Towards Integrating Topology Optimization and Additive Manufacturing

by

Amir M. Mirzendehdel

A dissertation submitted in partial fulfillment
of the requirements for the degree of
Doctor of Philosophy
(Mechanical Engineering)

at the
UNIVERSITY OF WISCONSIN-MADISON
2017

Date of final oral examination: 3/10/2017

The dissertation is approved by the following members of the final oral committee:

Krishnan Suresh, Professor, Mechanical Engineering
Xiaoping Qian, Associate professor, Mechanical Engineering
Dan Negrut, Associate Professor, Mechanical Engineering
Natalie Rudolph, Assistant professor, Mechanical Engineering
Matthew S. Allen, Associate professor, Engineering Physics

To my Parents, Ahmad and Farideh.

And my late *maman joon*.

ACKNOWLEDGEMENTS

I would like to sincerely thank my advisor, Professor Krishnan Suresh, for his invaluable support and insights throughout my graduate studies. By any measure he is the best teacher I have had in my higher education and I feel immensely fortunate to be able to discuss research topics with him on daily basis.

I am also grateful to my PhD committee, Professors Xiaoping Qian, Dan Negrut, Natalie Rudolph, and Matt Allen for their guidance, constructive feedback, and excellent classes.

It has been an honor to be a member of Engineering Representation and Simulation Laboratory (ERSL) at University of Wisconsin-Madison and I greatly appreciate the company and fruitful discussions with Praveen Yadav, Shiguang Deng, Chaman Singh Verma, and Behzad Rankouhi. I would like to especially thank Behzad for his help on experimental tests.

My special thanks go to my collaborators in University of Wisconsin School of Business, Liz Christenbury and Professor Jon Eckhardt for their help on devising and conducting a survey research on important issues in integrating topology optimization and additive manufacturing.

Words fail to express my deep and sincere gratitude to my parents for their endless support and unconditional love.

TABLE OF CONTENTS

LIST OF FIGURES

Figure

LIST OF TABLES

Table

ABSTRACT

Towards Integrating Topology Optimization
and Additive Manufacturing

by

Amir M. Mirzendehdel

Advisor: Dr. Krishnan Suresh

Topology optimization (TO) is an automated design tool that integrates mathematical modeling with numerical analysis to automatically reduce weight and material usage while ensuring certain prescribed constraints on performance of the design are satisfied. The high-performance light-weight designs created through topology optimization are often free-form and organic, manufacturing of which through traditional casting, forming, or subtractive technologies can become quite challenging. Additive manufacturing (AM) is a class of more modern technologies that seem to alleviate this issue by fabricating complex parts layer by layer. On the other hand, the cost of additively manufactured parts increase significantly with material usage. Therefore, optimizing designs can reduce material usage, build time, and post-process time to make AM worthwhile. Thus, TO and AM complement each other to fabricate ever more complex high-performance and customized yet affordable products. However, for these technologies to be integrated, there are certain issues, such as extraneous support structures or material anisotropy, that need to be considered within the optimization.

Focus of this thesis is mainly on:

1. Addressing challenges on reducing amount of support structure and considering process-induced anisotropy throughout the optimization process.

2. Exploiting the capabilities of AM in free-form fabrication to improve performance by generating more complex multi-material designs.

In other words, the present thesis attempts to make advances on integrating the two modern and promising fields, topology optimization and additive manufacturing by developing optimization algorithms that generate optimized designs while tracing Pareto frontiers. Perhaps the most important benefit of this class of methods is the fact that intermediate topologies remain structurally valid, thus iterative solvers can converge much faster. Further, these intermediate designs are local optimum solutions. These traits make these methods well-suited for rapidly exploring the design space to find free-form designs while ensuring their structural integrity.

CHAPTER I

Introduction

Topology optimization (TO) represents a class of computational methods for designing light-weight, high-performance structure [7; 8; 9]. After several years of intensive research, it has emerged as a powerful design tool, and is deployed in optimization of aircraft components [10; 11], spacecraft modules [12], automobiles components [13], cast components [14], compliant mechanisms [15], etc. Additive manufacturing (AM) refers to a class of manufacturing processes through which parts are fabricated by material addition [16]. The growing interest in AM stems from its ability to fabricate highly complex parts, a feat that was not possible through traditional subtractive techniques. Furthermore, AM is well-suited for small-batch production and on-spot fabrication where transporting built parts is expensive or even impossible.

AM and TO complement each other in that organic and complex designs generated through TO can be manufactured through AM technologies. On the other hand, the cost of AM parts increase significantly with material usage. Thus optimizing designs can be crucial in saving material usage, build time, and post-fabrication time [17]. However, there are certain challenges in TO for AM which need to be addressed before the two fields can be seamlessly integrated. Addressing some of these issues through efficient algorithms for 3D structures is the focus of this thesis. Figure 1.1 illustrates the synergy between TO and AM.

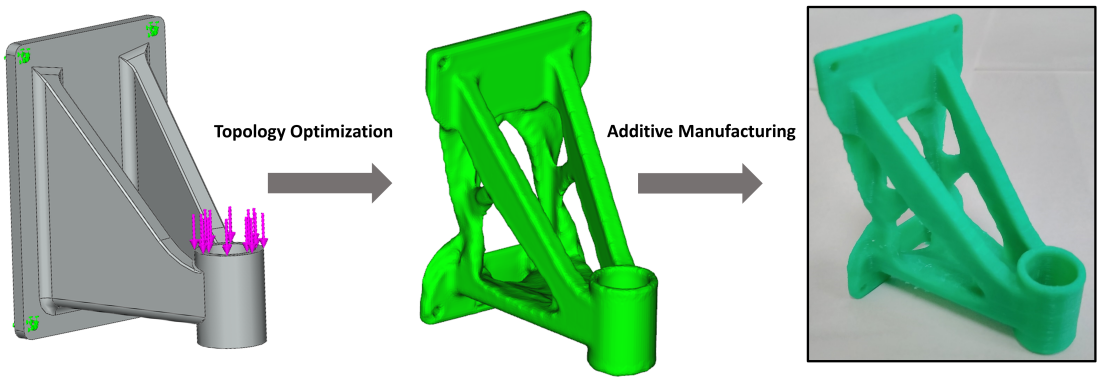

Figure 1.1: Synergy between TO and AM.

In this section, topology optimization (TO) methods (1.1) and additive manufacturing (AM) technologies (1.2) are briefly discussed and their synergy is explained. The contributions and outline of this thesis are summarized in sections (1.3) and (1.4).

1.1 Topology optimization

A typical TO problem can be posed as the following Single-Objective Problem (SOP): given an initial design domain D, we want to find an optimal topology that minimizes an objective while satisfying N (usually inequality) constraints,

$$\begin{aligned} &\underset{\Omega \subset D}{minimize}\, f(\Omega, \mathbf{u}) \\ &g_n(\Omega, \mathbf{u}) \leq 0 \qquad n = 1, ..., N \\ &\text{subject to} \\ &\mathbf{Ku} = \mathbf{f} \end{aligned} \tag{1.1}$$

where:

$$
\begin{aligned}
&f: \text{Objective function, such as compliance, etc.}\\
&\Omega: \text{Topology to be computed}\\
&D: \text{Domain within which the topology must lie}\\
&\mathbf{u}: \text{Finite element displacement field}\\
&\mathbf{K}: \text{Finite element stiffness matrix}\\
&\mathbf{f}: \text{External force vector}\\
&g_n: \text{Constraints}
\end{aligned}
\tag{1.2}
$$

1.1.1 Topology Optimization Approaches

Numerous approaches have been developed for topology optimization which are mainly categorized into 1) density-based [18; 19; 20; 8]) level-set [21; 22], and 3) evolutionary [23; 24; 25]. These methods are briefly discussed here; more detailed reviews are available in [7; 9; 26].

Density-Based Methods. Density-based approaches, also known as Solid Isotropic Material with Penalization (SIMP), are the most popular TO methods which have benefited from extensive research. The key concept in SIMP is to describe the material distribution by a pseudo-density variable $0 \leq \rho \leq 1$ that interpolates the underlying material properties [18]; for example, the Young's modulus is typically interpolated per element via $E_e = \rho_e{}^p E_0$. The penalization factor p depends on the physics and dimension of the problem; it is typically assigned a value of '3' for 3D linear elasticity. The pseudo-density variables are then optimized to reach the desired objective. Density-based methods are mathematically sound, however they usually result in *gray* elements with intermediate densities (neither 0 nor 1), which would require further post-processing.

Evolutionary Methods. Another family of topology optimization methods are the evolutionary based methods, where no gradient of the objective functional is computed and elements are removed or added simply based on field values. Xie and Steven [27], first developed evolutionary structural optimization (ESO) in 1993, to solve optimiza-

tion problems by gradually removing elements with lowest value of von-Mises stress until the desired volume fraction is reached . In 1996, stiffness-constrained optimization problems were solved using ESO [28], where the sensitivity value of each element was calculated using strain energy. There also exist different versions of evolutionary methods such as BESO[24], AESO[29], GESO[25], etc.

Level-set Methods. Yet another popular TO approach is based on level-sets, where material distribution is determined through implicit boundaries or iso-contours. Unlike SIMP, level-set methods create crisp interfaces between material phases and there are no ambiguities in existence of material at a given region. In level-set methods, the design is optimized through updating the materials interfaces by solving the Hamilton-Jacobi equation. Early versions of level-set methods were limited to shape optimization, where no new holes could be introduced in the domain. This limitation was alleviated by the development of a rigorous mathematical formulation for topological sensitivity [30; 31].

1.1.2 Topological Sensitivity

In the present thesis, we mainly focus on level-set methods. A general technique to solve the TO problem of Equation 1.1 is by solving the following unconstrained problem using Augmented Lagrangian method [28]:

$$\begin{aligned} &\underset{\Omega \subset D}{minimize}\, \mathscr{L} = f(\Omega, \mathbf{u}) + \sum_{n=1,\dots,N} \lambda_n g_n \\ &\text{subject to} \\ &\mathbf{Ku} = \mathbf{f} \end{aligned} \tag{1.3}$$

where $\mathscr{L}$ is called Lagrangian and $\lambda \in \mathbb{R}^N$ are non-negative Lagrange multipliers.

To solve the TO problem of Equation 1.3 one must compute the first-order change in the Lagrangian of Equation 1.3 due to small perturbations in design. In other words,

topological sensitivity must be computed where:

$$\mathscr{T}_{\mathscr{L}} = \mathscr{T}_f + \sum_{n=1,\dots,N} \lambda_n \mathscr{T}_{g_n} \tag{1.4}$$

For any quantity of interest φ, topological sensitivity $\mathscr{T}_\varphi$ at every point computes the change in φ due to introduction of a hypothetical infinitesimal hole in that point. In other words, topological sensitivity at a point p for any quantity of interest p is defined as [32]:

$$\mathscr{T}_\varphi(p) \equiv \lim_{r\to 0} \frac{\varphi(r;p) - \varphi_0}{\frac{4}{3}\pi r^3} \tag{1.5}$$

The most common objective in TO is maximizing the stiffness of the design or equivalently minimizing strain energy or compliance functional:

$$J = \int_\Omega \mathbf{C}_{ijkl}\boldsymbol{\epsilon}_{ij}\boldsymbol{\epsilon}_{kl} = \mathbf{f}^T\mathbf{u} \tag{1.6}$$

where $\mathbf{C}$ is the fourth-order stiffness tensor of material and $\boldsymbol{\epsilon}$ is the strain tensor. The related constrained problem can be formally stated as:

$$\begin{aligned} &\underset{\Omega\subset D}{minimize}\, J \\ &|\Omega| \le V_f|D| \\ &\text{subject to} \\ &\mathbf{Ku} = \mathbf{f} \end{aligned} \tag{1.7}$$

where $|\Omega|$ is design volume, V_f is the target volume fraction, and $|D|$ is the volume of the prescribed design domain. The Lagrangian of Equation 1.7 can be written as:

$$\mathscr{L} = \mathscr{T}_J + \lambda_V(|\Omega| - V_f|D|) \tag{1.8}$$

where λ_V is the Lagrange multiplier associated with the volume constraint.

To solve the TO problem of Equation 1.7 one must compute the first-order change in the Lagrangian of Equation 1.8 due to small perturbations in design. In other words, topological sensitivity must be computed where:

$$\mathscr{T}_{\mathscr{L}} = \mathscr{T}_J + \lambda_V \mathscr{T}_V \tag{1.9}$$

where $\mathscr{T}_{\mathscr{L}}$, $\mathscr{T}_J$,and $\mathscr{T}_V$ are topological sensitivities of Lagrangian, compliance, and volume.

Compliance Sensitivity. Closed-form expressions for the topological sensitivity of the compliance in homogeneous isotropic materials exist in 2D [30]:

$$\mathscr{T}_J(p) \equiv \frac{4}{1+\nu}\boldsymbol{\sigma} : \boldsymbol{\epsilon} - \frac{1-3\nu}{1-\nu} tr(\boldsymbol{\sigma})\, tr(\boldsymbol{\epsilon}) \tag{1.10}$$

And in 3D [31]:

$$\mathscr{T}_J(p) \equiv -20\mu\boldsymbol{\sigma} : \boldsymbol{\epsilon} - (3\lambda - 2\mu)\, tr(\boldsymbol{\sigma})\, tr(\boldsymbol{\epsilon}) \tag{1.11}$$

where λ and μ are the Lame' parameters.

Thus the topological sensitivity can be computed as follows: (1) FEA is carried over the domain, (2) stresses and strains are computed, and (3) then the topological sensitivity field is computed through Equation 1.11; the resulting field is illustrated in Figure 1.2c.The interpretation is that regions of low sensitivity correspond to regions with relatively lower impact on performance (and can be removed). Similar topological sensitivity fields can be computed for various performance metrics, both in 2D and 3D [33].

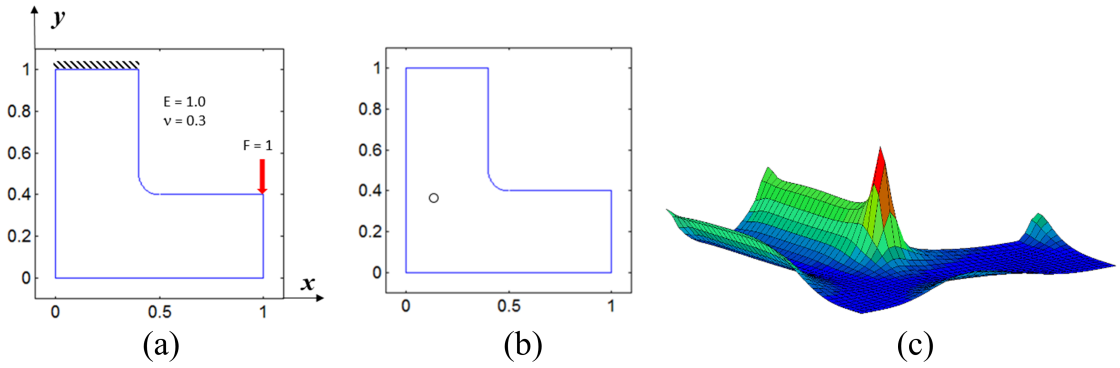

Figure 1.2: (a) A structural problem, (b) topological change, and (c) topological sensitivity field.

Volume Sensitivity. Considering the definition of Equation 1.5, the topological sensitivity of the design volume $|\Omega|$ in 3D is simply as follows,

$$\mathscr{T}_V \equiv \lim_{r\to 0} \frac{|\Omega - \frac{4}{3}\pi r^3| - |\Omega|}{\frac{4}{3}\pi r^3} = -1 \tag{1.12}$$

Observe that topological sensitivity of volume is constant everywhere in the domain. Consequently, the term $\lambda_V \mathscr{T}_V$ in Equation 1.9 only shifts the sensitivity field by a constant value and can be neglected. Hence, Equation 1.9 reduces to:

$$\mathscr{T}_{\mathscr{L}} = \mathscr{T}_V \tag{1.13}$$

1.1.3 Element Sensitivity

For many quantities of interest other than compliance such as anisotropic strength or inhomogeneous material distributions, no closed-form expressions exist. We will therefore also consider an alternate *discrete element sensitivity*, defined as the change in any quantity of interest when a single element e is deleted from the mesh:

$$\mathscr{D}_{\varphi}(e) \equiv \frac{\varphi(\Omega - e) - \varphi(\Omega)}{|e|} \tag{1.14}$$

Where $|e|$ is volume of a single finite element and is negligible with respect to volume of topology ($|e| \ll |\Omega|$).

Compliance Sensitivity. One can show that the discrete sensitivity is given by:

$$\mathscr{D}_J = \mathbf{u_e^T K_e u_e} \tag{1.15}$$

Figure 1.3 compares discrete sensitivity against the topological sensitivity for compliance for the 2D L-bracket. Observe that the two fields are quite similar since they essentially capture the first order change in compliance when material is removed.

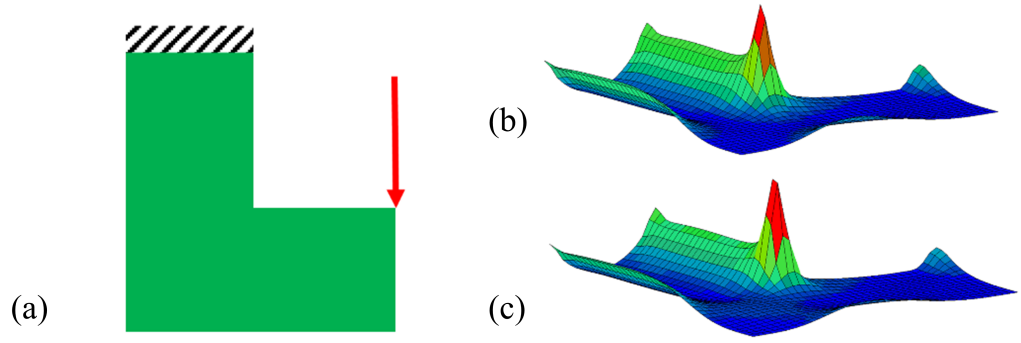

Figure 1.3: (a) L-bracket geometry, (b) topological sensitivity and (c) discrete element sensitivity.

Volume Sensitivity. Similar to Equation 1.12, element sensitivity of design volume is:

$$\mathscr{D}_V \equiv \lim_{r \to 0} \frac{(|\Omega| - |e|) - |\Omega|}{|e|} = -1 \tag{1.16}$$

1.1.4 Multi-Objective Topology Optimization

Alternatively, we can generalize SOP of Equation 1.1 to consider multiple objectives. The resulting Multi-Objective Problem (MOP) can be formulated as:

$$\begin{aligned} &\underset{\Omega \subset D}{minimize}\{f_m(\Omega, \mathbf{u})\} && m = 1, ...M \\ &g_n(\Omega, \mathbf{u}) \leq 0 && n = 1, ..., N \\ &\text{subject to} \\ &\mathbf{Ku} = \mathbf{f} \end{aligned} \tag{1.17}$$

The solutions of 1.17 are the so-called Pareto-optimal solutions, which give the best compromise between all objective and constraint functionals.

The concept of Pareto optimality, named after the Italian economist and engineer Vilfredo Pareto (1884-1923), is extensively used in multi-objective optimization in a wide range of applications from Economics and Ecology to Computer sciences and Engineering. It is a measure of efficiency; a solution is considered Pareto-optimal when further improvement of one criteria worsens at least one other. In other words, Pareto-optimality gives the best trade-off between multiple quantities of interest. A set of Pareto-optimal solutions are referred to as Pareto frontier, which can be particularly useful in engineering applications where a designer can explore multiple optimal designs and choose the one with the most suitable trade-off. Figure 1.4 illustrates the Pareto front for a generic bi-objective optimization problem.

To formally define Pareto optimality, we relate objective and constraint functions through the *feasible criterion vector* which is denoted as:

$$\begin{aligned} z(\Omega) &= \{z_1(\Omega), ..., z_{M+N}(\Omega)\}^T \\ &\equiv \{f_1(\Omega), ..., f_M(\Omega), g_1(\Omega), ..., g_N(\Omega)\}^T \in \mathbb{R}^{M+N} \end{aligned} \tag{1.18}$$

Consequently, the following sets can be defined:

$$
\begin{aligned}
Z &= \{z \in \mathbb{R}^{M+N} : z = z(\Omega), \Omega \subset D\} \\
P &= \{z \in Z : \nexists \tilde{z} \in Z \quad s.t. \quad \tilde{z}(\Omega) \leq z(\Omega)\} \\
F &= \{\Omega \subset D : z(\Omega) \in P\}
\end{aligned}
\tag{1.19}
$$

where Z is the *set of all feasible criterion vectors* and is bounded and closed in $\mathbb{R}^{M+N}$. P is the set of all Pareto-optimal criterion vectors. F is the frontier or the set of all Pareto-optimal designs.

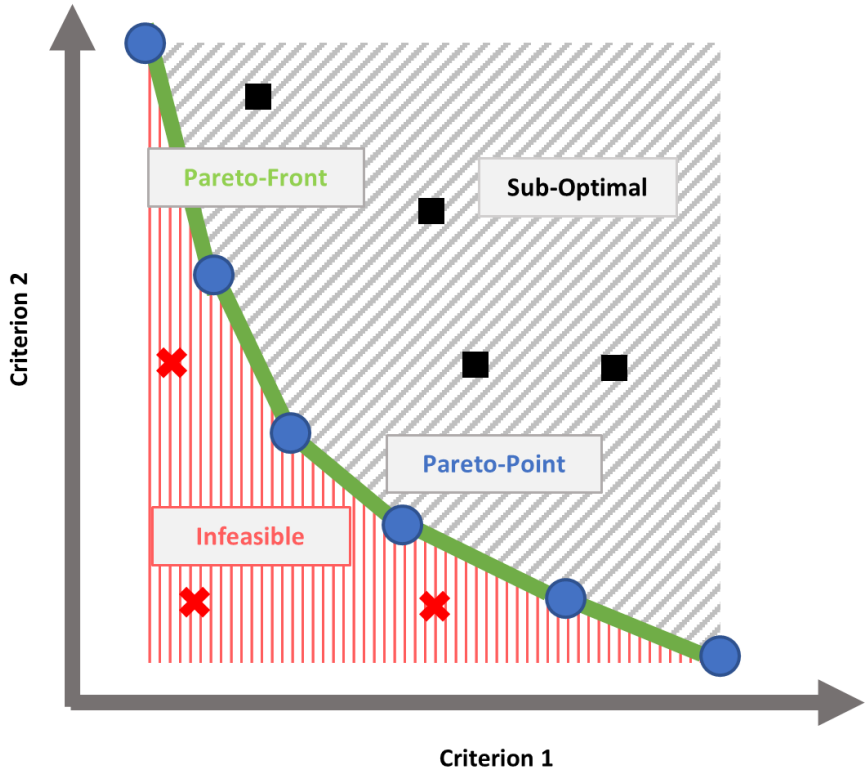

Figure 1.4: Pareto frontier for a generic bi-objective optimization problem.

Equation 1.17 is most commonly solved by the weighted-sums approach [32]. Let

the non-negative weighting vectors of Λ be defined as:

$$\Lambda = \{\lambda \in \mathbb{R}^{M+N} : \lambda \geq 0, \sum_{i=1}^{M+N} \lambda_i = 1\} \tag{1.20}$$

Considering definition of 1.18 and $\lambda \in \Lambda$, 1.17 can be rewritten as the following weighted-sums problem:

$$\begin{aligned} &\underset{\Omega \subset D}{minimize} \sum_{m=1}^{M} \lambda_m f_m + \sum_{n=M+1}^{M+N} \lambda_n g_n \\ &\text{subject to} \\ &\mathbf{Ku} = \mathbf{f} \end{aligned} \tag{1.21}$$

1.1.5 Compliance minimization via Pareto Optimality

Alternatively, to find Pareto-optimal designs the TO problem of Equation 1.7 can be stated as the following multi-objective problem:

$$\begin{aligned} &\underset{\Omega \subset D}{minimize}(|\Omega|, J) \\ &\text{subject to} \\ &\mathbf{Ku} = \mathbf{f} \end{aligned} \tag{1.22}$$

writing the Lagrangian we have:

$$\mathscr{L} = \lambda_V |\Omega| + \lambda_J J \tag{1.23}$$

For the topological sensitivity we have:

$$\mathscr{T}_{\mathscr{L}} = \lambda_V \mathscr{T}_V + \lambda_J \mathscr{T}_J \tag{1.24}$$

Since $\mathscr{T}_V = -1$ everywhere, Equation 1.24 reduces down to:

$$\mathscr{T}_{\mathscr{L}} = \mathscr{T}_J \tag{1.25}$$

In general, SOP of Equation 1.7 is used in traditional density-based approached, while the Pareto method solves the MOP of Equation 1.22. Figure 1.5 illustrates the difference between the two approaches. The Pareto-based method uses the topological sensitivity as a level-set to trace the Pareto curve for decreasing volume fraction. As the topology evolves, the topological sensitivity is recomputed at each iteration.

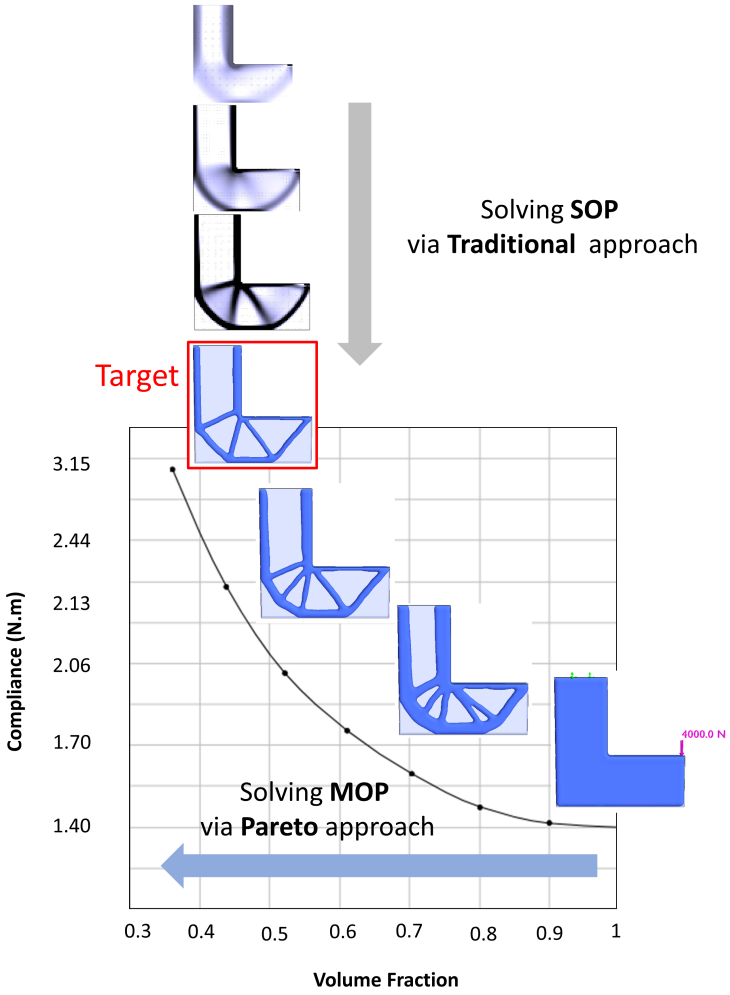

Figure 1.5: Difference between density-based (SOP) and Pareto (MOP) for optimizing L-bracket to 0.5 volume fraction.

Observe that intermediate designs produced in density-based methods are sub-optimal and might even become disjoint and invalid. Further, the gray regions with low pseudo-density result in an ill-conditioned stiffness matrix; subsequently, iterative solvers such

as conjugate gradient require large number of iterations to converge. On the other hand, intermediate designs generated through Pareto remain valid and (by definition) local optimal solutions; alleviating convergence issues caused by disjointedness.

1.2 Additive Manufacturing

There is a variety of AM processes which differ in material and the process through which layers of material are deposited. Generally, they can be classified as:

1. Material Extrusion
2. Powder Bed Fusion
3. Direct Energy Deposition
4. Vat Photo Polymerization
5. Material Jetting
6. Binder Jetting
7. Sheet Lamination

This thesis mainly focuses on material extrusion type technologies with an eye towards powder bed fusion processes, however more detailed reviews of AM technologies can be found in [16]. Material extrusion or Fused-Deposition Modeling (FDM) is an AM process through which molten filaments are extruded from a nozzle and deposited on a substrate to build the part layer by layer. FDM is fairly robust with respect to build scale and material [34]. This, along with other advantages such as ease of use, portability, affordability, and safety make FDM very promising in producing functional parts in applications such as:

a. Large-scale printing (cars and houses)[34; 35]
b. Biomedical customized parts [36]

c. Electronics-embedded designs [1]

d. Printing in hostile places, e.g. space missions [37]

Figure 1.6: FDM printed functional quadcopter. Printed via Voxel8 with embedded electronics and endures structural loading [1].

Most common materials in FDM are thermoplastics such as ABS or PLA, however other materials such as concrete or filaments with metal infills are also used. Powder Bed Fusion (PBF) is another class of AM technologies, in which a laser beam selectively scans regions of the powder bed to build the part through particle fusion. Based on the level of fusion, there are essentially two types of PBF processing, 1) *sintering*, where the particles are partially fused together and 2) *melting*, where the heat source is strong enough to melt the powder and create a melt pool as it scans the surface of the bed. For instance, Direct Metal Laser Sintering (DMLS) is specific to metal alloys, while for polymer-based materials Selective Laser Sintering (SLS) is used. Additionally, Selective Laser Melting (SLM or LM) is used to fabricated strong and dense metallic or ceramic parts, however compared to DMLS there are less metals available for this process. Electron Beam Melting (EBM) is another PBF process for metals which compared to SLM builds the part faster while at the price of reducing surface quality.

Directed Energy Deposition (DED) process is an another AM technology that uses metal powders to fabricate 3D parts. Unlike PBF, in DED the metal powder is melted as it is being deposited. Laser Engineered Net Shaping machine (LENS^{TM}) is also a closely related variation of DED.

Vat photo polymerization or StereoLithography Apparatus(SLA) is the oldest AM process where a laser beam scans a vat of liquid photopolymer to create the part through layer by layer polymerization. In Material Jetting (MJ), droplets of wax-like material are selectively deposited. Binder Jetting (BJ) can be used for a wide range of materials, where liquid adhesive material is selectively deposited to bond powders. Figure 1.7 summarizes AM technologies.

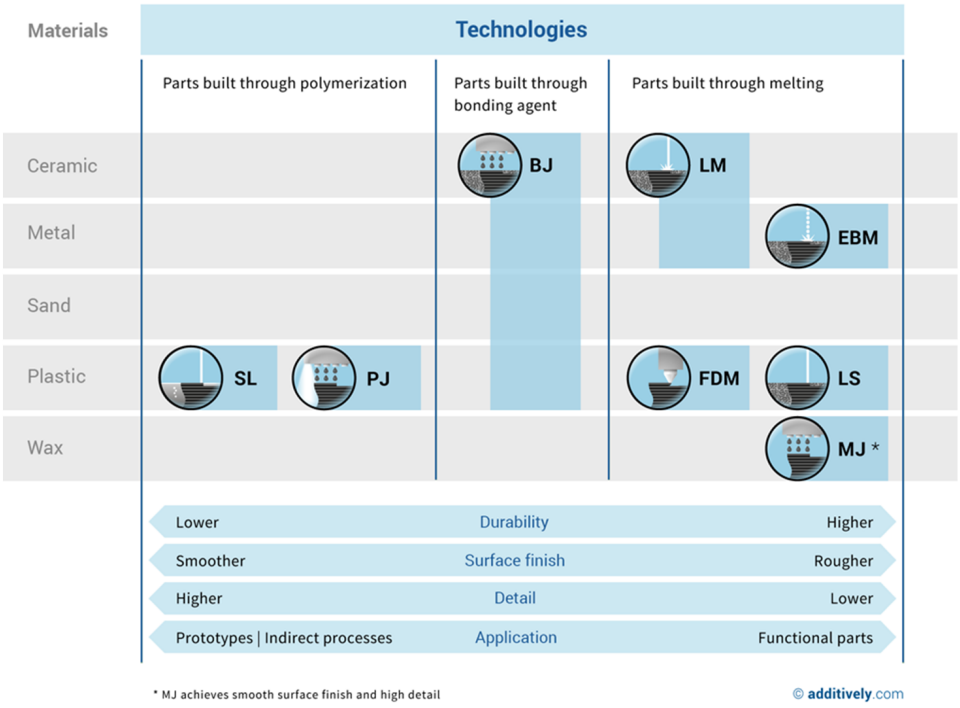

Figure 1.7: Overview of AM technologies [2]

1.3 Contributions

The contributions of this thesis are primarily on integrating TO and AM (mostly FDM) through 1) consideration of manufacturing constraints imposed by AM processes and 2) exploiting the capabilities of AM in free-form fabrication to explore more complex designs and improve performance. To this end, a survey study was conducted in collaboration with UW-Madison's school of Business to identify which of the five open

areas of research directly related to topology optimization are most important to engineers in academia and industry. The results of the study are summarized in Figure 1.8.

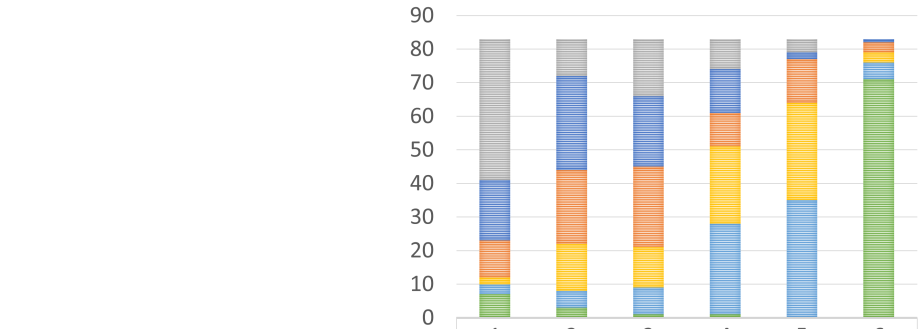

	1	2	3	4	5	6
Feature-based CAD of the optimized design	42	11	17	9	4	0
Material anisotropy	18	28	21	13	2	1
Multiple materials	11	22	24	10	13	3
Manufacturing Cost	2	14	12	23	29	3
Uncertainty	3	5	8	27	35	5
Other	7	3	1	1	0	71

Figure 1.8: Open areas of research in TO.

According to Figure 1.8, generating a feature-based CAD model of the optimized design is the most popular choice; however, this is a post-optimization task and is beyond the scope of this work. Considering material anisotropy and multiple materials during TO are the most popular open research topics which lie within the scope of this thesis. The third related issue is considering manufacturing cost, which is a vast topic and heavily depends on the specific process, printer, material, and many other factors. However, an important consideration in design for FDM and SLM processes is the need for support structures, which has negative impact on cost by increasing material usage, build time, and post-fabrication time. Contributions of the present thesis can be summarized as follows:

1. Introducing topological sensitivity for support structures and an efficient Pareto tracing algorithm to reduce support structure volume while optimizing performance of the design.

2. Presenting a new sensitivity analysis for anisotropic materials based on Tsai-Wu criterion. The numerical results are verified through experiments.
3. Developing an efficient method for large-scale multi-material topology optimization based on tracing Pareto frontiers.

1.4 Outline

In chapter 2, a TO framework is devised to simultaneously control support structure volume while monitoring performance of design. First, an unconstrained TO problem is solved through Pareto tracing. Since the intermediate designs are all valid and local optimum, we can track how support structure volume changes throughout optimization. Thence, we can impose a realistic constraint on support structure. Next, a topological sensitivity for support structure is introduced and numerical validations are provided.
In chapter 3, anisotropic strength is considered as an objective functional. The strength criterion is based on the well-known Tsai-Wu criterion. A sensitivity analysis is conducted on p-norm of strength and a Pareto-based algorithm is proposed. For validation, the anisotropy induced by FDM process is considered and numerical examples are verified through experiments.
In chapter 4, a Pareto approach to multi-material topology optimization in 3D is proposed, where we are minimizing a cost criterion such as weight or price while maximizing a performance criterion such as stiffness or strength. Every optimization step is composed of two successive sub-steps, where the first one reduces cost and the second increases performance. Numerous numerical examples are provided to demonstrate effectiveness and efficiency of the proposed algorithm.
Chapter 5 summarizes the contributions of this thesis and discusses possible future research topics.

CHAPTER II

Support Structure Constraint

2.1 Introduction

Before we discuss how support structure constraints can be imposed, we will briefly review how support structures are algorithmically generated. This will provide key insights into developing appropriate constraints.

Support structure generation in AM is based on the overhang concept which states that *if the angle between the boundary normal and the build direction exceeds a certain threshold, then support structures are needed at that point* [17]. For instance, for the design and the build-direction illustrated in Figure 2.1a, the subtended angle α is illustrated in Figure 2.1b. Given a threshold $\hat{\alpha}$ (typically around 135°), boundary points with $\alpha > \hat{\alpha}$ are considered overhanging, and require support as illustrated in Figure 2.1c; For simplicity, vertical support structures are assumed in this chapter; support structures may terminate at the platform or at any opposing non-overhanging point. The union of all such support structures results in a support volume as illustrated in Figure 2.1d. The fill-ratio, i.e., material density, of support structures is typically less than that of the primary design.

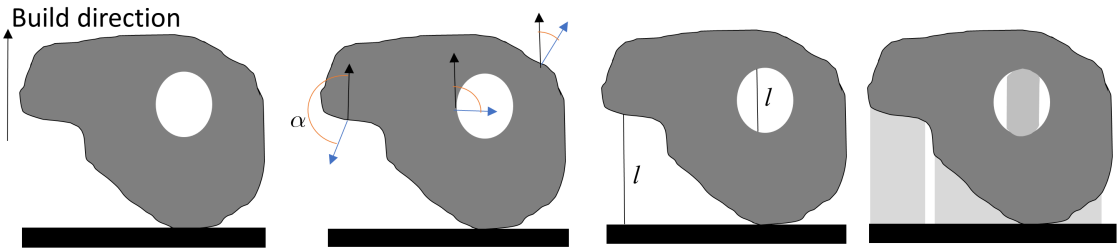

Figure 2.1: (a) Build-direction. (b) Subtended angle. (c) Support length. (d) Support volume.

There are a number of AM processes that may require support structures yet for different reasons. In FDM, support structures as the plastic part is built, each layer must be properly supported by previous layers due to weight. For overhang surfaces, this support is not provided by design itself, therefore extra support structures must be printed so that the molten material would not droop. Figure 2.2 demonstrates Failure of FDM parts due to lack of support.

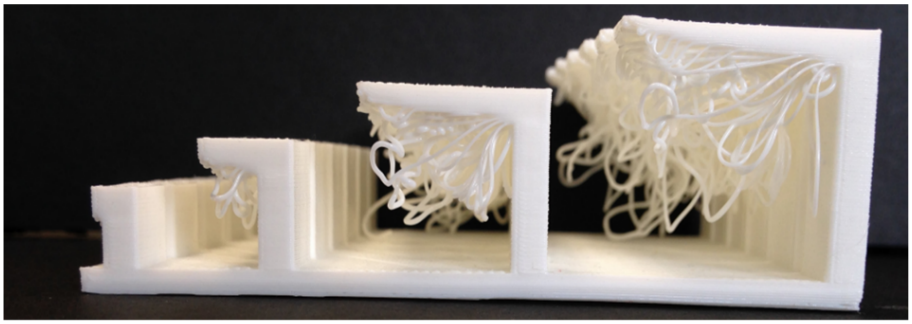

Figure 2.2: Failed FDM prints in absence of support structure [3].

Unlike FDM, in Powder Bed Fusion (PBF) processes, the weight of part is sustained by the bed of powder, however some metal PBF technologies, such as Selective Laser Melting (SLM), Direct Metal Laser Sintering (DMLS), or Electron Beam Melting (EBM) may require support structures to diffuse the accumulated heat in overhang surfaces. In other words, Support structures in metal additive manufacturing work as a heat sinks to dissipate excessive heat into the surrounding powder. Figure 2.3 shows an optimized GE engine bracket printed by Arcam (EBAM) metal 3D printer.

Figure 2.3: Optimized GE engine bracket printed by Arcam (EBAM) metal 3D printer.

If proper support is not provided, the temperature difference can result in dramatic distortions, warpage, curling, or burning; thus failure of the print job. Figure 2.4 (left) shows the warpage occurred during EBAM process in the absence of support structures. Figure 2.4 (right) demonstrates the effectiveness of extraneous support, as the warpage is clearly mitigated.

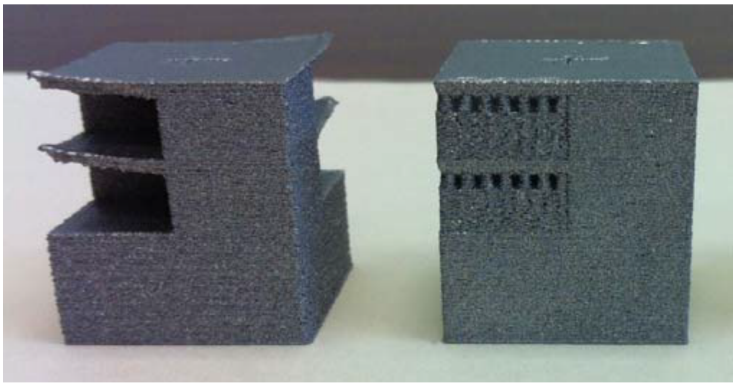

Figure 2.4: warpage in EBAM printed part in the absence of support structures (left) and mitigation of support in presence of support (right) contact[4].

Printing support structures directly adds to the build-time and material cost. Material costs can be substantial in AM; for example, the largest percentage cost for metal AM, besides the machine cost that is amortized, is material cost (18%) [43]. Further, support structures can be hard to remove (and sometimes even inaccessible), leading

to the post-fabrication (clean-up) cost. Post-fabrication costs make-up for about 8% of AM product cost [43]. Thus, reducing the amount of support structure is of particular interest and can be significantly beneficial. There have been many attempts towards this addressing this issue, which are reviewed in the next section.

2.2 Related work

Support structure minimization is of significant interest within the AM community, and several methods have been proposed to reduce its amount. These are classified into the following categories.

Strategy 1: Finding an optimal build direction

AM build-direction can have a significant impact on support structures. Therefore, a popular strategy is to find a build-direction that minimizes support structure volume (and optionally optimizes other AM metrics). For instance, Jibin [38] developed a multi-objective function to find an optimal build direction to minimize volumetric error, support structure, and build time. Along similar lines, Pandey et al. [39] proposed a multi-criteria genetic algorithm to minimize support structure and build time, while improving surface quality. In both instances, weighted averaging was used to solve multi-objective problems. Nezhad et al. [40] proposed tracing the Pareto front to find the optimal part orientation; the Pareto front involved two objective functions, namely support structure and build time. Paul and Anand [41] used a voxel representation (rather than the STL representation) to minimize support structure while satisfying constraints on cylindricity and flatness errors. More recently, Das et al. [42] identified optimal build orientation with respect to tolerance errors and support structure volume by extracting product manufacturing information. Alternate approaches for selecting build-direction include optimizing post-build quality and perception [43], and increased (cross-sectional) mechanical strength [44].

Strategy 2: Generating efficient support structures

While the above methods assume vertical support columns, more efficient support structures have been proposed for a given build-direction. For example, the commercial software Meshmixer^{TM} generates tree-like support structures. While this potentially reduces the support volume, manual modifications are required to ensure printability. Vanek et al. [45] overcame this deficiency by presenting an efficient method for automatically creating tree-like support structures that are printable. Specialized methods have also been proposed for specific AM processes. For instance, Barnett and Gosselin [46] developed shell and film techniques to create support structures for processes with weak support materials, such as three dimensional foam printers. Dumas et al. [47] exploited scaffolding structures to generate efficient supports for Fused Deposition Modeling (FDM). Considering the stability of the object throughout the build process, the method first identifies support points and then creates horizontal bars between vertical pillars to reduce the support volume. A contour-based support generation scheme was proposed in [48] based on layer-wise analysis. The method first analyzes all of the layers and then generates support anchors using offset and Boolean operations to ensure printability of the part.

Strategy 3: Following design rules for AM

A third strategy is to include support volume constraints during the manual design process [49; 50; 51; 52; 53]. This is often based on design rules such as [50]: (1) avoid surfaces with large overhang angle, (2) avoid large-size holes (say, larger than 5 mm) [47] perpendicular to the build-direction, (3) avoid trapped surfaces where support structures are hard to remove, and (4) use explicit fillets and chamfers to avoid support structures. Since these rules are feature-based, they are hard to include during TO.

Strategy 4: Optimizing the topology for AM

The final strategy is to include AM constraints within TO. As stated earlier, the advantage of this strategy lies in the (potential) integration of these two technologies.

Imposing manufacturing constraints in TO has been addressed before; a particularly

relevant constraint is that of *draw-direction* constraint for casting [54; 55], where the TO algorithm was modified so as to avoid *inserts*. While this is analogous to the support structure constraint, there are two fundamental differences: (1) support structures are governed by a threshold angle, while the threshold angle for draw-direction is essentially zero, and (2) the draw-direction constraint is bidirectional, while the build-direction in AM is unidirectional. Thus, the draw-direction methodology does not apply to AM; novel methods are needed.

Bracket et. al. [17] made several recommendations on integrating TO and AM,. For example, to minimize support structures, they suggested a penalization scheme on overhanging surfaces, and an edge analysis was carried out on a benchmark 2D example. The overhang constraint was suggested but not demonstrated. Wang et. al. [56], proposed a novel strategy to reduce the material cost by first extracting the frame structure of the design. The frame is in fact the solution of a multi-objective optimization problem that minimizes the number of struts while considering stability and printability.

Leary [57] introduced the idea of self-supporting designs, where the TO optimized design was altered to include features similar to support structures. In other words, support structures were introduced as design features *a posteriori*. Since this is carried out after TO, the structural load path is altered, and may violate stress and other performance constraints.

Based on the suggestions proposed by Bracket et. al [17], Gaynor and Guest [58], employed a smooth Heaviside approximation to penalize overhanging surfaces within a SIMP based TO. They demonstrated that, for 2D compliance minimization, this scheme changes the topology to be AM friendly. Specifically, they demonstrated that it is possible to eliminate support structures by suitably changing the TO process. The results are encouraging, but they noted convergence issues when the overhanging penalization was imposed. Recently, Hu et. al [59] proposed a shape optimization technique to alter the model to a more self-supported one. To this end, once a volumetric tetrahedral mesh

is generated, the overhang tetrahedra are mapped onto the Gauss sphere and minimally rotated to a self-supported state; the method was also proven to be effective in finding optimal build direction.

2.3 Limitations of the Overhang Constraint

Further, the definition suggests that if one could *eliminate all overhanging surfaces*, then support structures can also be eliminated. But, this may not an effective optimization strategy for the following reasons:

1. *Eliminating all overhanging surfaces may not be possible.* Researchers [58] have demonstrated that one can eliminate overhang surfaces in certain 2D problems. However this is unlikely to be successful in general, especially in 3D (as the numerical examples in Section 4 demonstrate). As was also suggested in [17], "*...there will probably be instances where it is not necessary for all support structure to be eliminated and so the user should be able to have some control over the strength of the penalty function.*".

2. *The overhang constraint does not penalize support volume.* Two overhanging surfaces with equal subtended angle will be penalized equally, although the support volume associated with one may be much larger than the other. To avoid such contradictions, a direct constraint on the support volume is desirable.

3. *Penalizing just the overhanging surfaces is insufficient.* Support volume may be enclosed between an overhanging surface and an opposing surface, as illustrated in Figure 2.5. To reduce support volume, both surfaces must be penalized, for example, by moving them closer to each other as illustrated. By penalizing the overhanging surface, only half the problem is addressed.

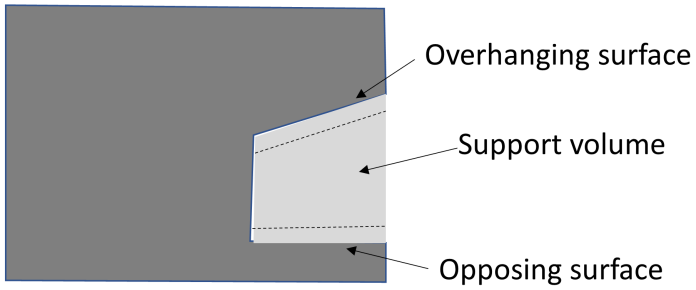

Figure 2.5: Moving either the overhanging or its *opposing* surface changes the support volume.

We propose here a formulation that relies on (1) dynamically estimating the support volume as the topology evolves, and (2) imposing constraints on the support volume through topological sensitivity methods. Consider the first step of dynamically estimating the support volume. In this framework, we assume that support structures are vertical. Therefore, the support volume is simply the integral of the support length over the boundary, multiplied by a suitable fill-ratio, (see Figure 2.1d), i.e.

$$S = \gamma \int_{\alpha \geq \hat{\alpha}} l_p d\Gamma \tag{2.1}$$

where:

$$\begin{aligned} &S: \text{ Support strucuture volume} \\ &\alpha: \text{ Subtended angle} \\ &l_p: \text{ Lenght of support structure at boundary point p} \\ &\gamma: \text{ Fill ratio (relative material density) of support structures)} \end{aligned} \tag{2.2}$$

In Equation 2.1, the exact value of the fill ratio is not critical; it can be assumed to be 0.5, without a loss in generality.

Further, for short overhangs, it is well known that support structures are not needed. For

example, for FDM, the allowable overhang [17] can be approximated via:

$$h(mm) = \begin{cases} 5 + 40(1 - \frac{\alpha}{\pi}) & \frac{3\pi}{4} < \alpha \leq \pi \\ \infty & 0 \leq \alpha \leq \frac{3\pi}{4} \end{cases} \tag{2.3}$$

Thus, at any point on the boundary, if the subtended angle is α , support structures are not needed if the overhang distance is less than h given by Equation 2.3. In implementation, we search for self-supporting boundary within a distance given by Equation 2.3; see Figure 2.6.

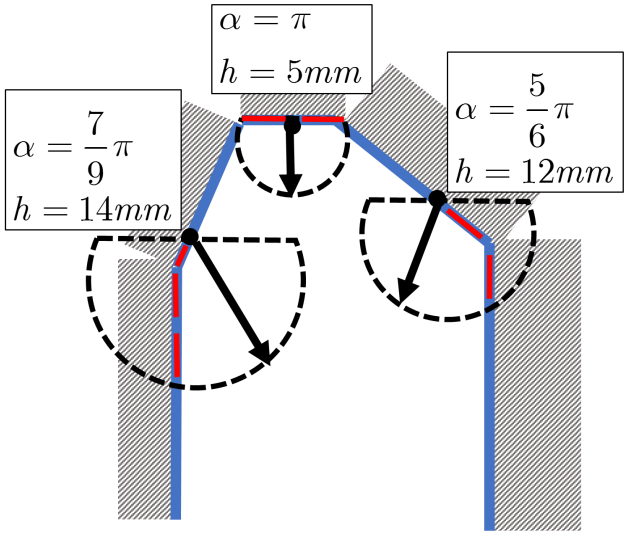

Figure 2.6: Searching for self-supporting boundary.

2.4 Options for imposing support constraint

Consider the three-hole bracket of Figure 2.7 where the two left side holes are fixed and the right-hand side hole is subject to a downward unit load. The underlying material is assumed to be isotropic ABS plastic with Young's modulus of $E = 2GPa$ and Poisson ratio of $\nu = 0.39$.

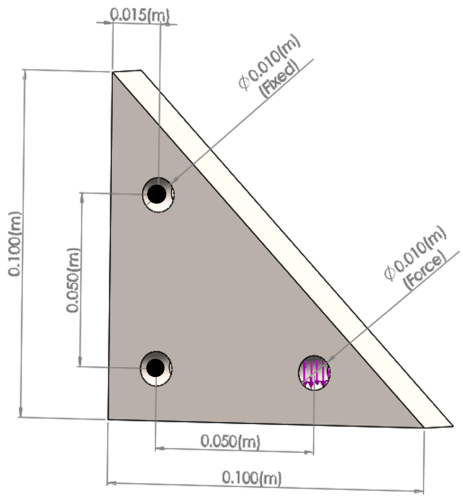

Figure 2.7: Three-hole bracket geometry and boundary condition.

Next, we want to reduce volume of the initial design by 50% while retaining its stiffness by solving the following compliance minimization problems:

$$\begin{aligned} &\underset{\Omega \subset D}{minimize}\{|\Omega|, J\} \\ &\text{subject to} \\ &\mathbf{Ku} = \mathbf{f} \end{aligned} \tag{2.4}$$

Figure 2.8 illustrates the progression of the optimization process in Pareto up to a volume fraction of 0.5. Observe that optimization begins with a volume fraction of 1.0, and generates multiple topologies that lie on the Pareto front. This will play an important role in the proposed method for constraining the support structure volume. Further, we do not rely on a velocity field concept to move the boundary; instead, we use fixed-point iteration, proposed by [60], to converge to Pareto-optimal designs; the implementation is described in [61; 33; 62].

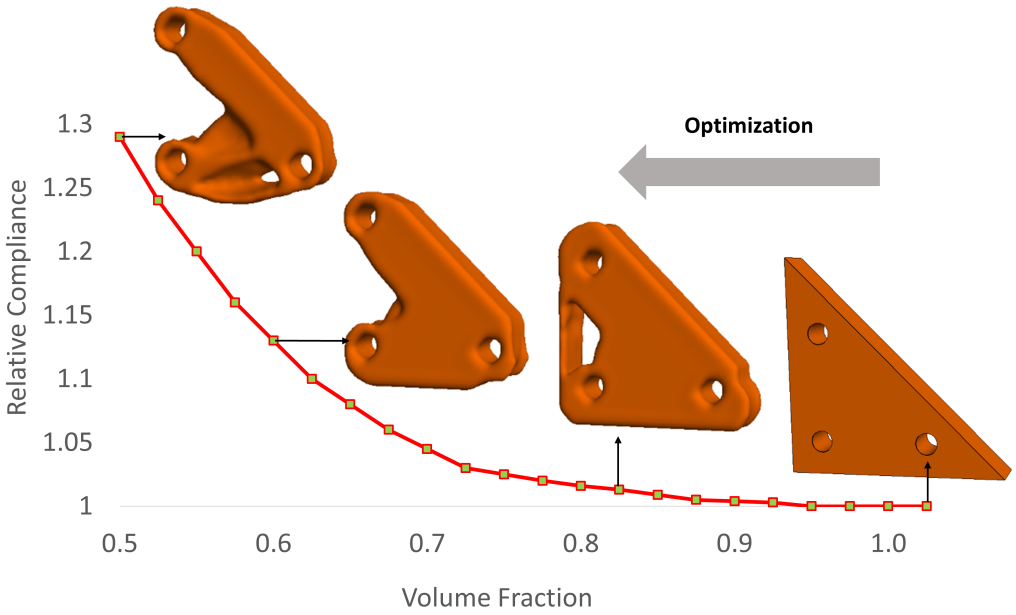

Figure 2.8: Pareto curve for three-hole bracket optimization.

Next consider the challenge of imposing support volume constraint. Perhaps the simplest strategy is to impose an absolute constraint as in:

$$S \leq S_{max} \tag{2.5}$$

However, this places an unreasonable burden on the designer to arrive at an absolute value for the upper limit a priori. Instead, we consider relative upper bound constraints. Specifically, recall that in the Pareto method, one generates multiple topologies for various volume fractions, i.e., one can solve the unconstrained problem, and store reference support volumes $\eta S_{unc.}(v)$ at intermediate volume fractions. For example, Figure 2.9 illustrates the support volume $\eta S_{unc.}(v)$ for the unconstrained problem. The support volume curve is, in general, non-smooth, unlike the compliance curve in Figure 2.8.

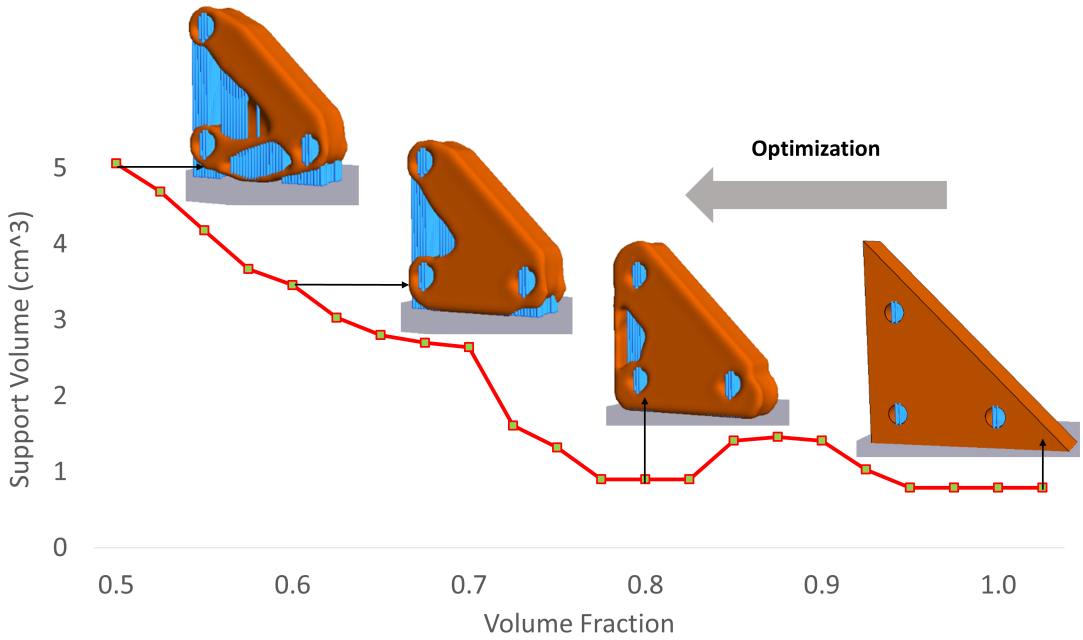

Figure 2.9: Relative support structure volume at different volume fractions for unconstrained problem.

Next we impose a relative constraint with respect to $\eta S_{unc.}(v)$, via a user-defined parameter $\eta(0 < \eta \geq 1)$:

$$S(v) \leq \eta S_{unc.}(v) \tag{2.6}$$

In other words, Equation 2.6 states that the desired support volume should be less than the unconstrained support volume by a factor of η, at each volume fraction (through interpolation, if necessary). Alternately, one can impose a constraint at the final volume fraction, but imposing a constraint at each volume fraction leads to a smoother optimization process. Further, in this formulation, we treat Equation 2.6 as a *soft* constraint, i.e., the constraint is used to prioritize the solutions within the feasible space (see section 2.5.2), rather than limiting this space [63]. In summary, we propose the following support-structure constrained TO problem, where the parameter η is used to strike a

balance between performance and AM costs (see numerical experiments in section 2.8):

$$\begin{aligned} &\underset{\Omega \subset D}{minimize}\{|\Omega|, J\} \\ &S(v) \leq \eta S_{unc.}(v) \qquad (soft) \\ &\text{subject to} \\ &\mathbf{Ku} = \mathbf{f} \end{aligned} \tag{2.7}$$

In section 2.5, we consider a gradient based TO framework for solving the above problem. The framework will rely on topological sensitivity for performance [31; 30], and the proposed topological sensitivity for support structure volume.

2.5 Sensitivity analysis

To compute the sensitivity, we begin with the Lagrangian of Equation 2.8:

$$\mathscr{L} = \lambda_V |\Omega| + \lambda_J J + \lambda_S (S(v) - \eta S_{unc.}(v)) \tag{2.8}$$

Thus for topological derivative we have:

$$\mathscr{T}_{\mathscr{L}} = \lambda_J \mathscr{T}_J + \lambda_S \mathscr{T}_S \tag{2.9}$$

For example, for an intermediate topology in Figure 2.10a, (1) FEA is carried over the new topology, (2) the stresses and strains are computed, and (3) the topological sensitivity field is computed through Equation 1.11; the resulting topological sensitivity field is illustrated in Figure 2.10b and Figure 2.10c.

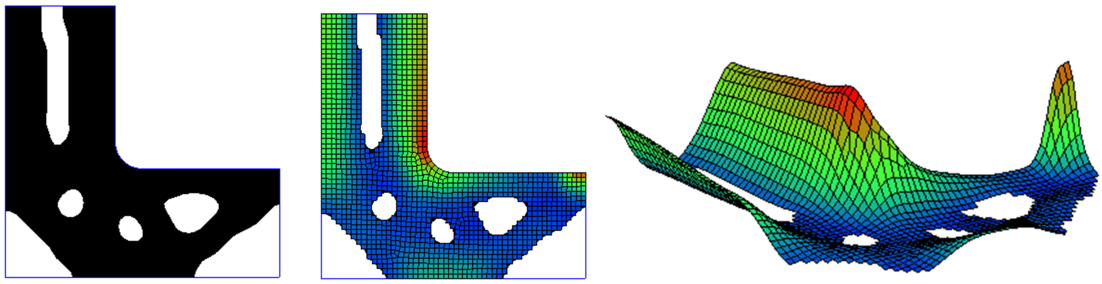

Figure 2.10: (a) Instance of topology, (b) compliance topological sensitivity (2D) (c) 3D view of (b).

2.5.1 Sensitivity of Support Volume based on Surface Angle

Analogous to the topological sensitivity for performance, we propose here topological sensitivity of support structure volume, i.e., *the rate of change in support structure volume with respect to volumetric measure of the hole.* Towards this end, consider the two scenarios illustrated in Figures 2.11 and 2.12, where the design is infinitesimally perturbed either in the interior, or on the boundary.

Interior Hole (Figure 2.11): If a hole of radius ϵ is inserted in the interior of the domain, one can compute the topological-shape sensitivity as follows. Employing the shape sensitivity method proposed in [30], the topological derivative is computed via:

$$\mathcal{T}_S(p \in \Omega) \equiv \lim_{\substack{\epsilon \to 0 \\ \delta \to 0}} \frac{S(\Omega_{\epsilon+\delta}) - S(\Omega_\epsilon)}{V(B_{\epsilon+\delta}) - V(B_\epsilon)} \tag{2.10}$$

In Equation 2.10, $S(\Omega_\epsilon)$ and $V(B_\epsilon)$ are support volume and hole volume, for a hole of radius ϵ. Using the above definition, one can show that the support volume sensitivity is given by (see Figure 2.11a and Appendix B):

$$\mathcal{T}_S(p \in \Omega) = \frac{3(\pi - \hat{\alpha} - \sin(\hat{\alpha})\cos(\hat{\alpha}))(\sin(\hat{\alpha}) - \frac{\sin^3(\hat{\alpha})}{3})}{\pi} \tag{2.11}$$

Where $\frac{\pi}{2} \leq \hat{\alpha} \leq \pi$ is the threshold angle. For example, if the threshold angle $\hat{\alpha} = \frac{\pi}{2}$, then $\mathcal{T}_S(p) = 1$, i.e., the entire hole will need to be filled with support structures; a typical value is $\mathcal{T}_S(p \in \Omega) \approx 0.72$ when $\hat{\alpha} = \frac{3\pi}{4}$.

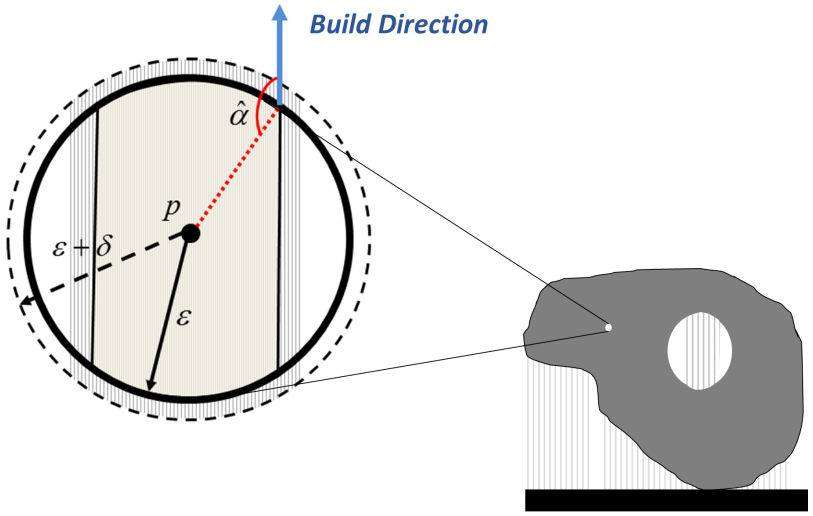

Figure 2.11: Sensitivity of support volume in the interior.

Boundary Hole (Figure 2.12): Unlike the interior, the support volume on the boundary depends both on the local neighborhood (curvature) and the length and direction of support. In order to capture both, we define a scalar function $F^S(x_p)$at each boundary point as follows:

$$F^S(x_p) = \frac{1}{2} l_p (1 - \cos(\alpha_p)) \tag{2.12}$$

In Equation 2.12, α_p is the angle between surface normal and build direction at boundary point p. We compute the sensitivity for the worst-case scenario, where boundary is perturbed along support at each point $\hat{S}_p$. One can then show that the sensitivity at the boundary is given by Equation 2.13:

$$\mathcal{T}_S(p \in \partial\Omega) = \frac{1}{2}(1 - \cos(\alpha_p)) \tag{2.13}$$

Further, for each overhang point, the same sensitivity value is assigned to its corresponding opposite point (see Figure 2.12).

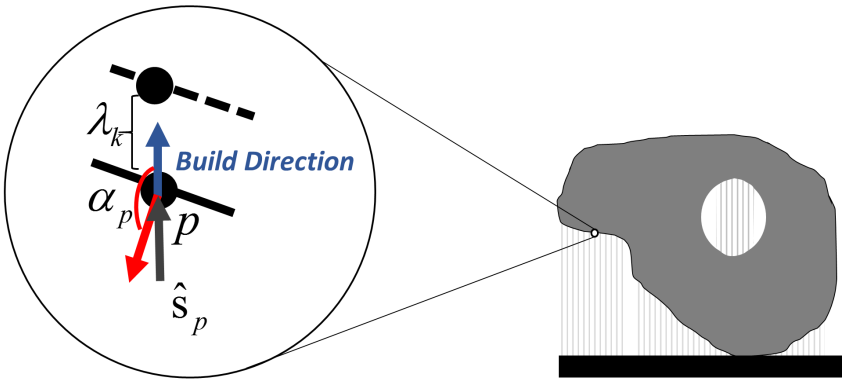

Figure 2.12: Sensitivity of support volume on boundary.

Given the above definitions, one can compute the support volume sensitivity at all points; this is illustrated in Figure 2.13a and Figure 2.13b.

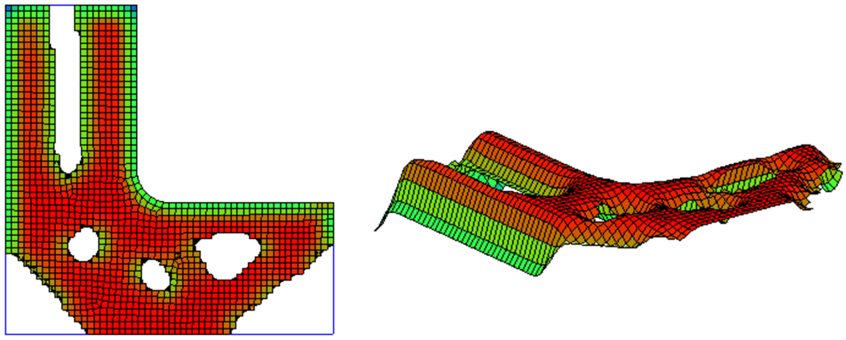

Figure 2.13: (a) Sensitivity of support volume (2D). (b) 3D view of (a).

2.5.2 Sensitivity Weighting

Once the performance and support volume sensitivities are computed and normalized, we exploit the well-established augmented Lagrangian method [64] to impose support structure constraint. Specifically, the support-constrained in Equation 2.7 is first

expressed in the standard form:

$$g = \begin{cases} \dfrac{S(v)}{\eta S_{unc.}(v)} - 1 \leq 0 & \eta S_{unc.}(v) \neq 0 \\ S(v) = 0 & \eta S_{unc.}(v) = 0 \end{cases} \tag{2.14}$$

A popular method for imposing such constraints the augmented Lagrangian method [64], where the constraint and objective are combined to a single field:

$$\mathscr{L} = J + \mathscr{L}_g \tag{2.15}$$

where:

$$\mathscr{L}_g = \begin{cases} \lambda g + \dfrac{1}{2}\gamma(g)^2 & \lambda + \gamma g > 0 \\ \dfrac{1}{2}\dfrac{\lambda^2}{\gamma} & \lambda + \gamma g \leq 0 \end{cases} \tag{2.16}$$

Where λ is the Lagrangian multiplier and γ is the penalty parameter (that are updated during the optimization process [64]). By taking the topological derivative of Equation 2.15, we arrive at Equation 2.17 for the effective sensitivity [65]:

$$\mathscr{T} = \mathscr{T}_J + w_S \mathscr{T}_S \tag{2.17}$$

where

$$w_s = \begin{cases} \mu + \gamma g & \mu + \gamma g > 0 \\ 0 & \mu + \gamma g \leq 0 \end{cases} \tag{2.18}$$

Observe that the weight on the support structure sensitivity is zero if $g < \dfrac{-\lambda}{\gamma}$, else it takes a positive value.

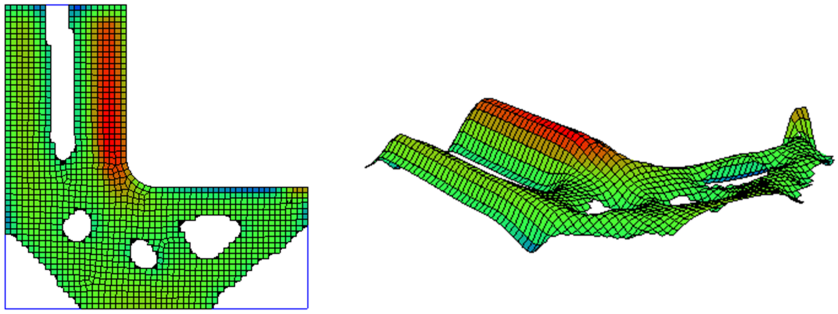

Figure 2.14: (a) Equally weighted sum of the two sensitivity fields (2D) (b) 3D view of the sensitivity field.

To illustrate Equation 2.17, suppose the two topological sensitivity fields are normalized to unity, and suppose $w_s = 1.0$, the resulting field is illustrated in Figure 2.14a and Figure 2.14b. Observe that the resulting field is a combination of the two fields in Figure 2.10 and Figure 2.13. As the optimization progresses, the weight is determined dynamically from Equation 2.18, while the parameters $\mu$and γ are updated during each iteration as described in [65].

2.6 Algorithm

Piecing these concepts together, the proposed algorithm proceeds as follows (see Figure 2.15):

1. It is assumed that the unconstrained optimization problem has been solved, and $S_{unc.}(v)$ has been computed.
2. Carry out FEA on Ω; compute the normalized sensitivity fields $\mathscr{T}_J$, $\mathscr{T}_S$ and the weighted field $\mathscr{T}$ as described above; smoothen the $\mathscr{T}_J$ field [33]. Observe that, every time the topology changes, FEA must be executed and the topological sensitivities recomputed.
3. Treating $\mathscr{T}_J$ as a level-set function, extract a new topology Ω using fixed-point iteration [33], and the iso-surface is extracted [66]. If the topology has not converged, repeat steps 2 and 3.

4. Decrement the volume fraction and return to step 2 until the desired volume is reached.

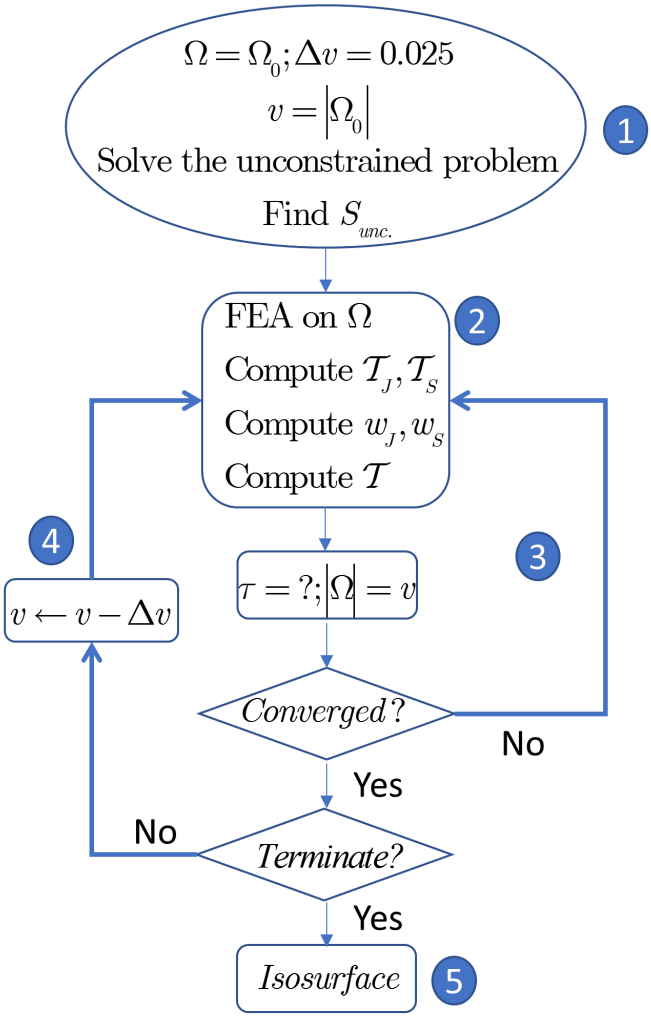

Figure 2.15: Support Structure constrained Pareto algorithm.

2.7 Limitations

Since the topological sensitivity depends on the *rate of change* in support structure volume, to ensure convergence of the optimization process it must necessarily be smooth and differentiable. However this is not the case in practice and in some cases a slight change in surface angle might introduce or eliminate a large volume of support

structure. Topological sensitivity on boundary points proposed in Equation 2.13 is a sufficiently smooth approximation to what is expected in practice. Hence this assumption on differentiability prevents the current algorithm to make decisions that require abrupt change in support volume. This becomes highlighted in special cases where it is possible to remove all support structure through introducing certain shapes such as isosceles. This will be demonstrated in Numerical experiments.

2.8 Numerical Experiments

In this section, we demonstrate the proposed method through several examples. In section 2.8.1, we study the impact of the proposed method on the optimized design and support volume for a simple 2D example. In section 2.8.2, the impact of user controlled parameter η is examined for the three-hole bracket. In section 2.8.3, a more complex 3D design is optimized and the designs are printed to demonstrate the effectiveness of the proposed method. In section 2.8.4, the effect of build direction on support volume and performance are studied on a large-scale optimization problem. In all of the experiments, the material is assumed to be isotropic ABS plastic with Young's modulus of $E = 2GPa$ and Poisson ratio of $\nu = 0.39$. The threshold angle $\hat{\alpha}$ is assumed to be $\frac{3\pi}{4}$, unless otherwise noted.

2.8.1 2D MBB

Consider the 2D MBB design (implicit thickness of 1 cm) in Figure 2.16 whose support structure reduction was studied in [58]. The initial design requires no support and the objective is to find stiffest design at 0.65 volume fraction.

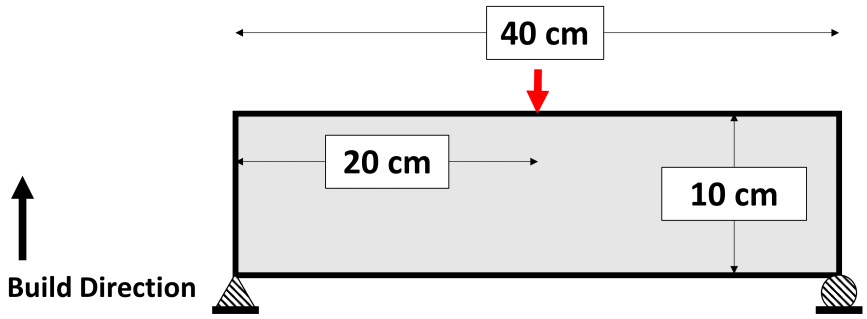

Figure 2.16: 2D MBB example with boundary conditions and build direction.

Recall that we first solve the unconstrained problem, and a series of topologies that lie on the Pareto curve are generated; see Figure 2.17. Figure 2.18 illustrates the corresponding support volume in cm3.

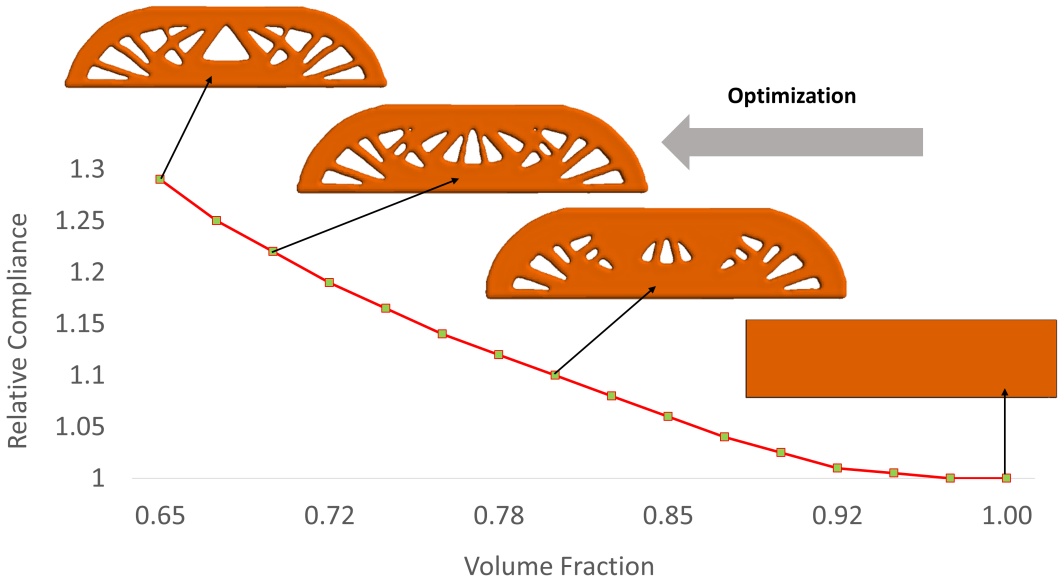

Figure 2.17: Compliance Pareto curve for the MBB beam.

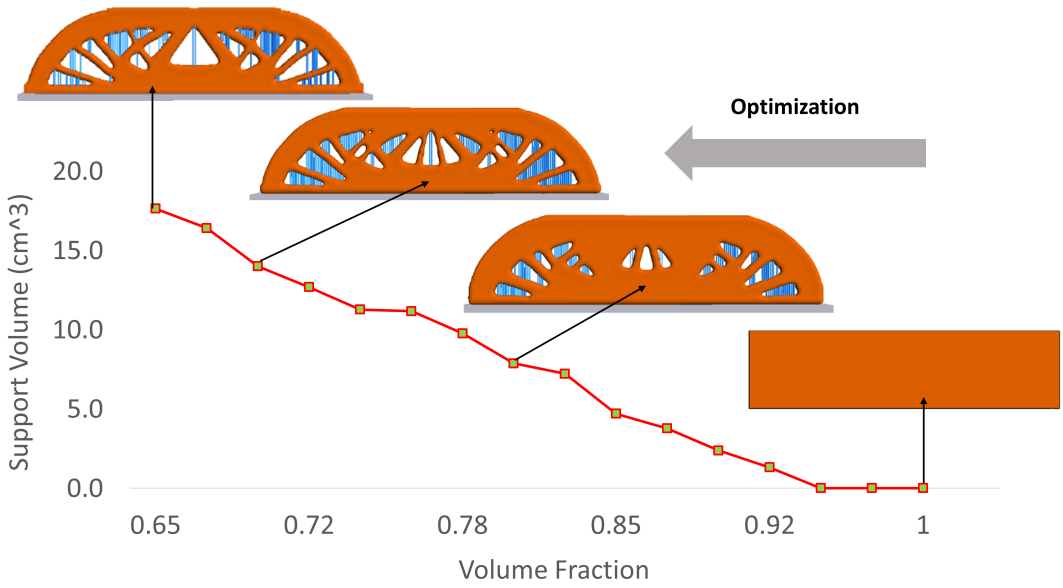

Figure 2.18: Support volume for the unconstrained MBB beam problem.

The unconstrained support volume from Figure 2.18 is then used as a reference to impose a support structure constraint. In particular, we study the impact of the relative constraint η (see Equation 2.7) on the *final topology* at a volume fraction of 0.65. Table 2.1 summarizes the results; observe that with increased support structure constraint, the proposed method reduces the number of internal holes. This is, by no means, the unique solution to the problem; it happens to be a solution that meets the desired constraints. As was discussed in section 2.7, in this particular example changing shape of the holes to isosceles would be more desirable, but that would require abrupt change in sensitivity analysis and current framework avoids such designs.

Table 2.1: 2D MBB. Effect of support constraint on optimized design.

Final Topology	Support Volume Constraint	Support Volume Achieved	Relative Compliance
	-	-	1.29
	80%	62%	1.34
	60%	59%	1.42
	40%	42%	1.56
	0%	0%	1.75

2.8.2 Three-Hole Bracket

In this example, we study the impact of the support structure constraint over the entire Pareto curve. Considering the three-hole bracket illustrated earlier in Figure 2.7 and recalling the compliance Pareto curve for the unconstrained problem in Figure 2.8, and the corresponding support structure curve in Figure 2.9; Figure 2.19 illustrates compliance Pareto curves for the unconstrained and the constrained case. As expected, imposing the support constraint increases compliance.

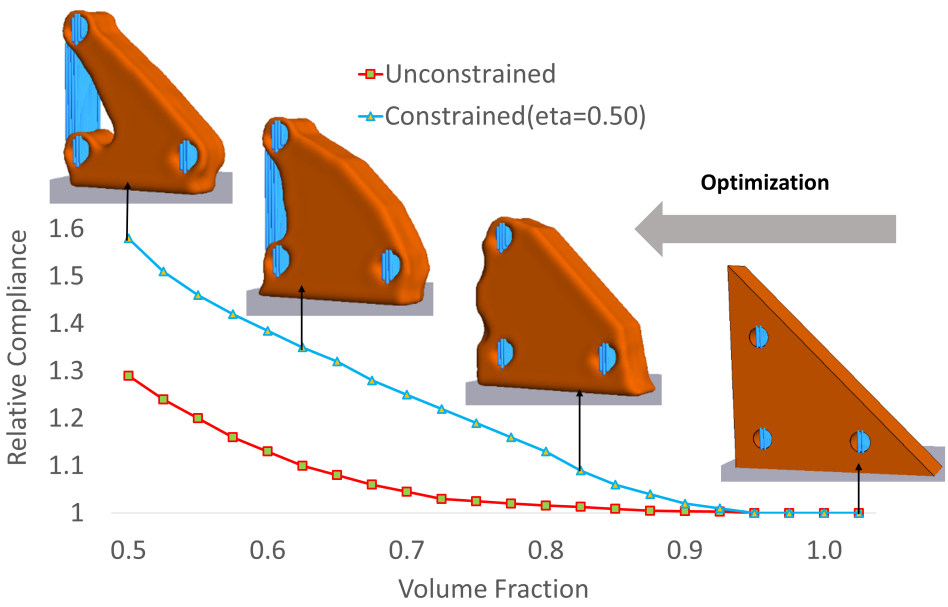

Figure 2.19: Unconstrained and constrained Pareto curves for three-hole bracket optimization.

Figure 2.20 illustrates the evolution of support structure volume for the two scenarios. Observe that as expected, removing more material can either increase or decrease the support volume due to its nonlinearity, nonetheless imposing a stringent constraint on support structure consistently reduces the support volume w.r.t the corresponding unconstrained design.

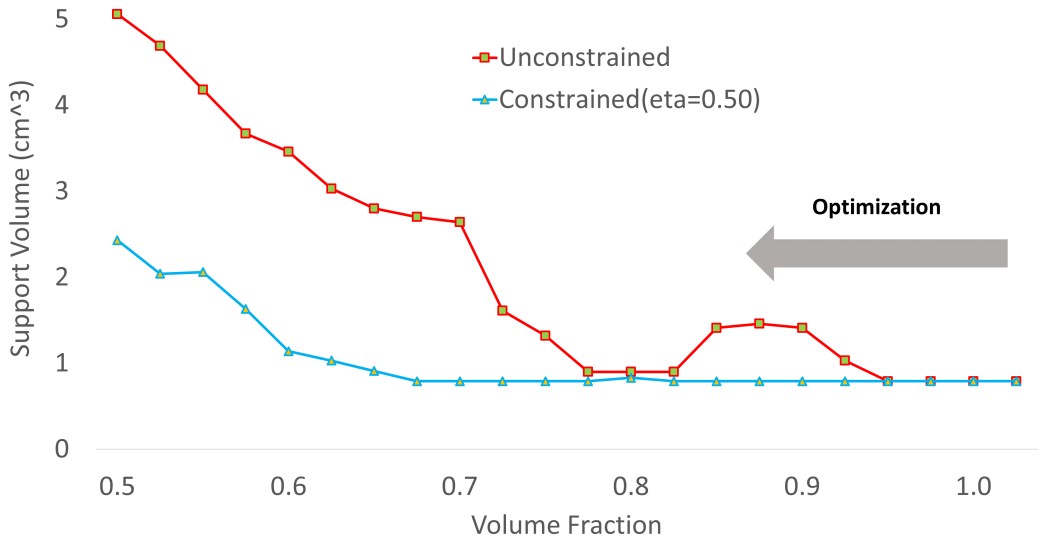

Figure 2.20: Evolution of support volume for three-hole bracket.

The support volume prior to optimization is $S_0 = 0.79(cm^3)$. The objective is to find stiffest design at 0.5 volume fraction. Figure 2.21 illustrates the optimized design for (a) unconstrained, (b) constrained with $\eta = 0.5$. Relative compliance values for these cases are respectively 1.24 and 1.58.

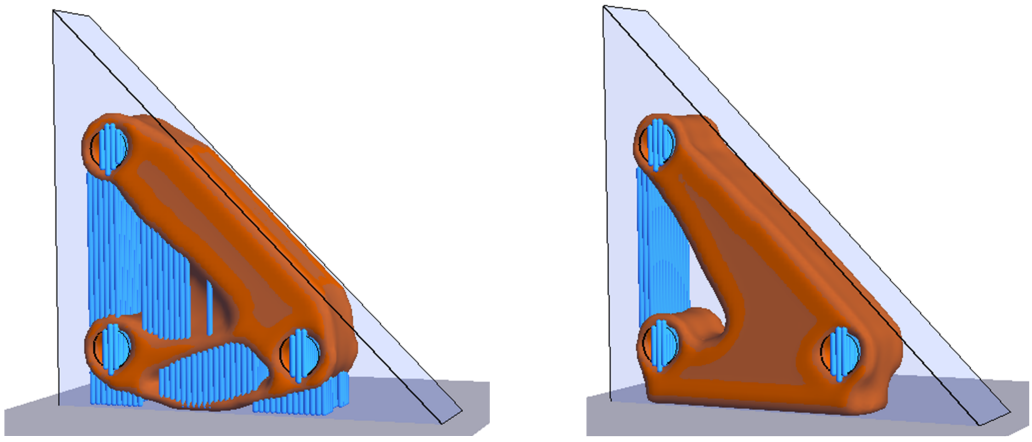

(a) (b)

Figure 2.21: Optimized three-hole bracket. (a) Unconstrained (b) Constrained with $\eta = 0.50$.

2.8.3 Mount Bracket

Consider the mount bracket of Figure 2.22 subject to structural constraints and loading as illustrated. The threshold angle $\hat{\alpha}$ is assumed to be $3\pi/4$. The build direction illustrated in Figure 2.22 is chosen such that it gives the best surface quality on the larger cylindrical face; for this design, prior to optimization the support volume is $S_0 = 1.12(cm^3)$. The objective is to find stiffest design at 0.7 volume fraction.

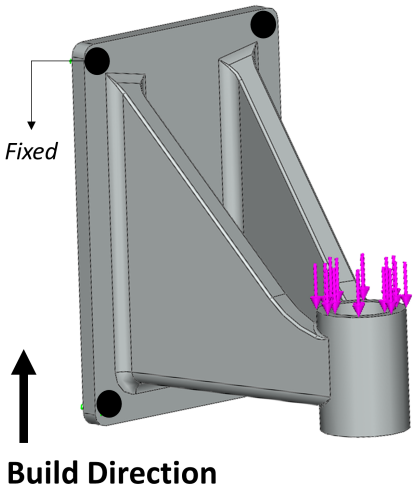

Figure 2.22: Mount bracket with boundary conditions and build direction.

Figure 2.23 illustrates the optimized designs of (a) unconstrained and (b) constrained with $\eta = 0.80$. The final support structure volume for the unconstrained design is $9.24(cm^3)$ while for the constrained design it has reduced by about 17% to $7.70(cm^3)$.

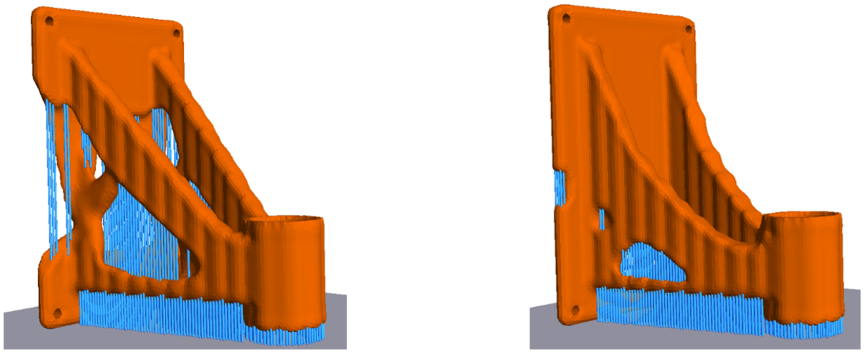

Figure 2.23: Optimized mount bracket at 0.7 volume fraction. (a) Unconstrained (b) constrained with 0.8 support fraction.

Figure 2.24 illustrates the evolution of support volume throughout the optimization process. Observe that up to 0.9 volume fraction the unconstrained and constrained results are very similar. However for lower volume fractions the constrained support volume is consistently about 20% smaller than that of unconstrained design.

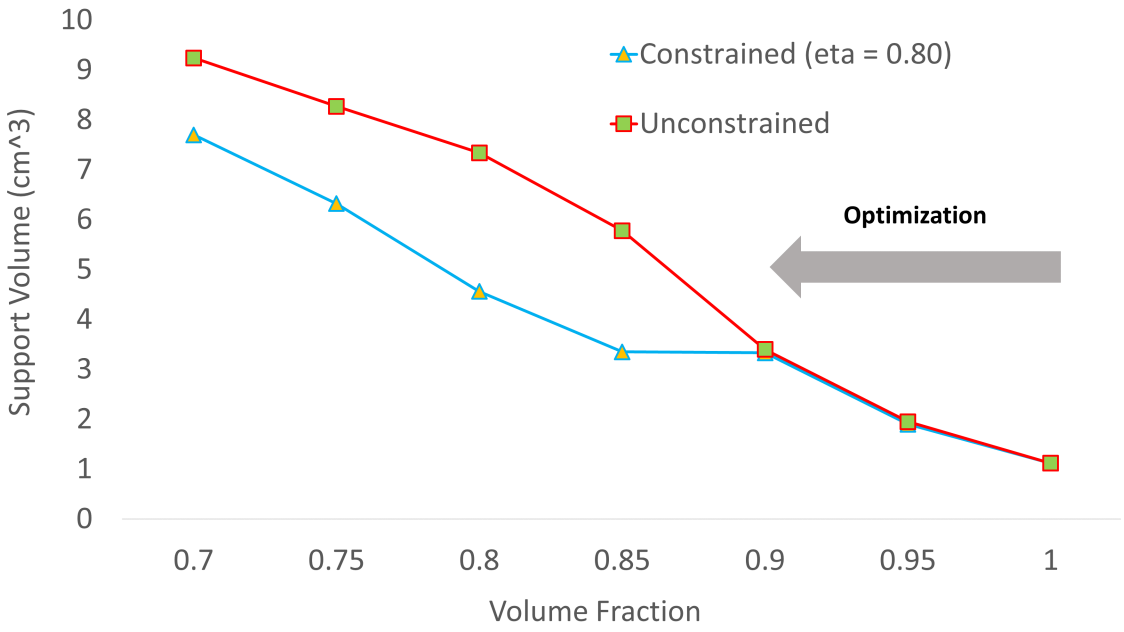

Figure 2.24: Evolution of support volume for the mount bracket.

Figure 2.25 illustrates the evolution of relative compliance values as more material

is removed from the design. For the unconstrained design the final C/C_0 is about 1.05, while by imposing support constraint this value increases to about 2.52. Figure 2.25 highlights the trade-off between support volume and compliance when the support constraint is imposed. It is essentially up to the designer to choose the intensity of support constraint.

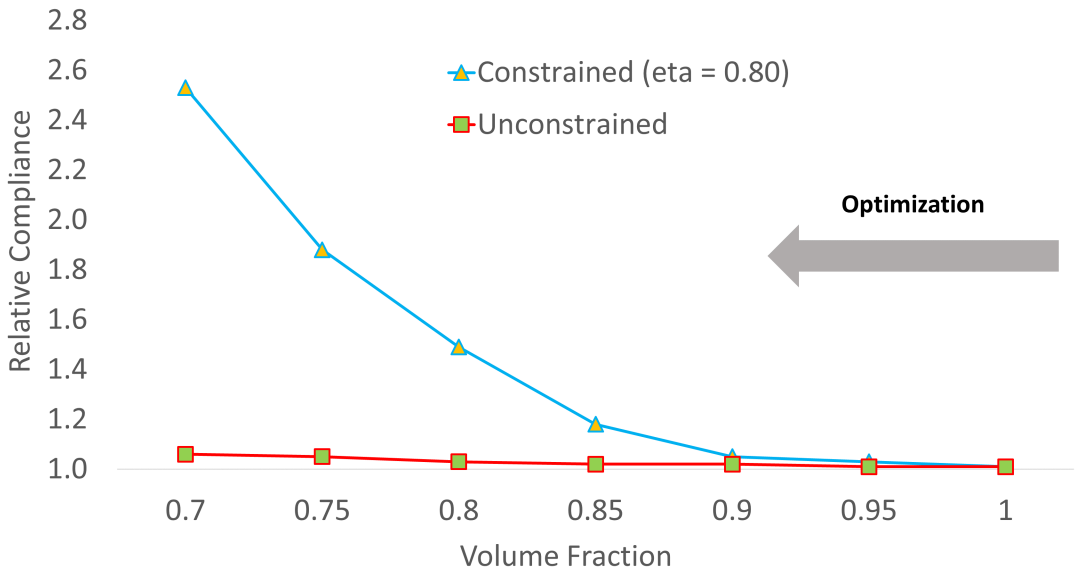

Figure 2.25: Evolution of compliance for the mount bracket.

Figure 2.26: Printed mount bracket and the required support structures at 0.7 volume fraction.

To verify the validity of these simulated results, each of these topologies were printed on an *XYZ Da Vinci 2.0* fused deposition printer. Note that the support structures were not generated by our algorithm, they were introduced by the XYZ software, based on default settings. Figure 2.26 illustrates the actual parts after clean-up. Observe that both of the optimized designs have the same weight (as prescribed by the optimization), while the amount of support structure is substantially reduced in the constrained design. This example illustrates the effectiveness of the proposed algorithm in handling support constraints.

2.8.4 Different Build Directions

In this section, we demonstrate the robustness of the proposed method with respect to the build directions. Consider the problem posed in Figure 2.27 where the geometry is described via numerous curved surfaces and two cylindrical holes in two different directions; this makes picking the optimal build orientation challenging. Further to capture the complexity of the design, a hexahedral mesh with about 1.7 million degrees of freedom was used.

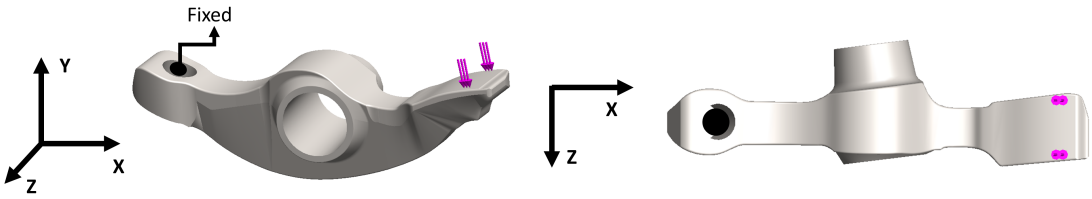

Figure 2.27: Rocker arm of Honda Supra-X 100 cc (grabcad.com): (a) Iso view, (b) Top view.

A plausible choice for the build direction is -Z, as shown in Figure 2.28. In this direction, the larger cylinder has better surface quality and the initial support is minimal. First, we optimize the design for minimum compliance at 0.7 volume fraction without imposing any constraints on support structure(Figure 2.28a).

In this particular orientation, $S_{unc.}(0.7)$ is smaller than S_0, which means that during optimization, some of the overhanging surfaces are removed to reduce the overall support volume. Next, in order to further reduce support structure, we set $\eta = 0.90$ and solved the optimization problem of Equation 2.7 to arrive at the design in Figure 2.28b. Observe that by imposing the support constraint, no additional overhangs are created, however since the initial design is dominant, support volume is reduced by only about 3%, while the compliance has increased by about 15%.

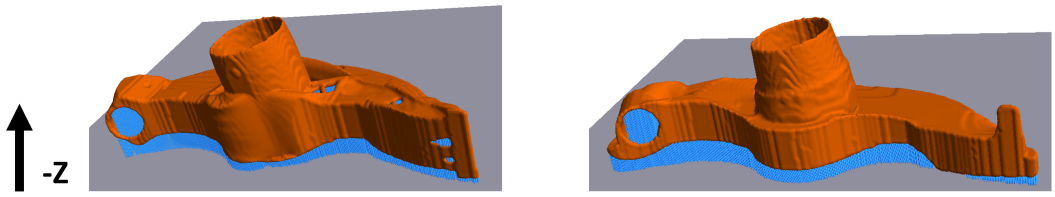

Figure 2.28: Rocker arm. Building in -Z direction a) unconstrained b) constrained.

Next, the build direction was set to +Y since it gives better surface quality for the smaller cylindrical hole. Solving the same optimization problem as before results in the unconstrained design in Figure 2.29a and constrained design in Figure 2.29b with $\eta = 0.90$. The support volume was reduced by 20%, while the compliance increased by 32%.

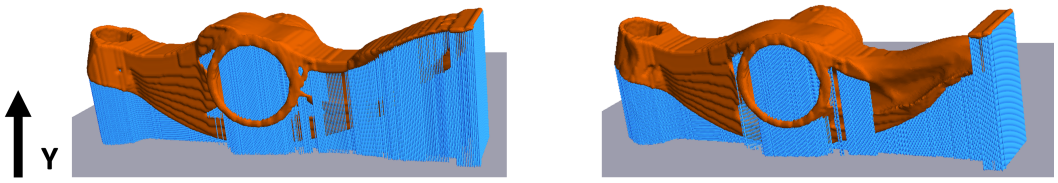

Figure 2.29: Build direction along +Y direction: (a) unconstrained, and (b) constrained.

Finally, the build direction was set to +X; a justification for this direction can be better fusion between layers, since the print area is smaller than previous directions. The results are summarized in Figure 2.30: the support volume was reduced by 4%, while the compliance increased by 10%.

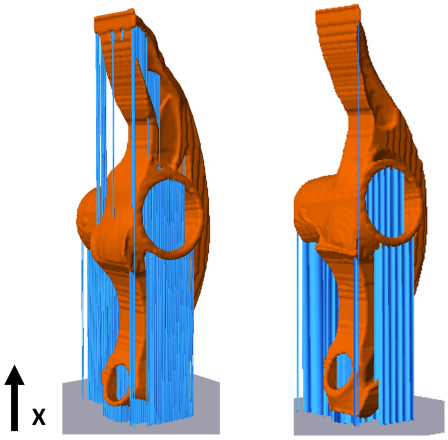

Figure 2.30: Rocker arm. Building in +X direction, unconstrained(left) and constrained (right)

2.8.5 Computational Cost

In this section, we study the convergence and performance of the proposed algorithm. All experiments are conducted on a Windows 7 64 bit machine with an 8-core Intel Core i7 CPU running at 3.00 GHz, and 16 GB of memory. Table 2.2 summarizes the CPU times of the unconstrained and constrained examples presented in sections 2.8.1 to 2.8.4. Observe that as the size of the problem and the support volume increases, the constrained problem requires more computational effort to compute support sensitivity

field, yet for all of the presented experiments CPU time remains comparable.

Table 2.2: Computational cost, with and without support structure constraints.

Example	**Finite element degrees of freedom**	**CPU time Unconstrained**	**CPU time Support Constrained**
MBB	27,400	5.25 sec.	5.5 sec.
Three-hole bracket	45,000	10 sec.	($\eta = 0.75$)11 sec. ($\eta = 0.50$)13.7 sec.
Rocker Arm (-Z)	≈ 1.7 million	28 min 30 sec.	30 min 59 sec.
Rocker Arm (+Y)	≈ 1.7 million	28 min 30 sec.	32 min 6 sec.
Rocker Arm (+X)	≈ 1.7 million	28 min 30 sec.	30 min 14 sec.

CHAPTER III

Anisotropic Strength

3.1 Introduction

Material anisotropy and weakness along build direction, especially in FDM, is an important issue which becomes more critical when the part is functional and must satisfy strength-related constraint. There are mainly two types of anisotropy, namely 1) intrinsic e.g. composites and 2) process induced. Intrinsic anisotropy is often favorable since it can provide more freedom through intentionally creating directional preference in behavior. On the other hand, process-induced anisotropy is the result of process limitations and is often unfavorable. In this chapter, we focus on addressing material anisotropy induced throughout FDM process due to lack of interlayer fusion as illustrated Figure 3.1. Note that anisotropy in FDM could manifest itself in two ways: 1) anisotropic constitutive properties relating stress and strain, and 2) directional strengths. However, current experimental results suggest that in some cases (see section 3.6), printed parts exhibit isotropic constitutive properties [67]. The focus of this chapter is on strength anisotropy.

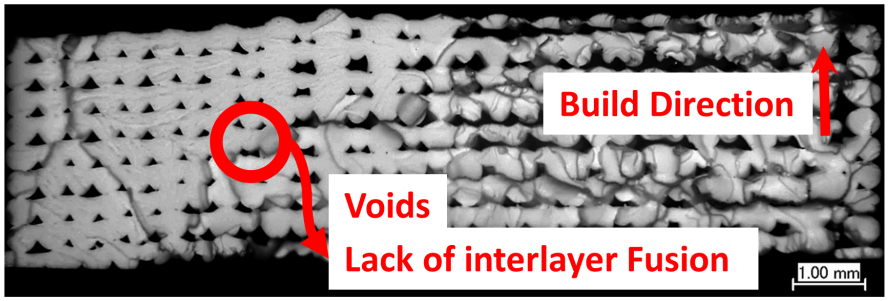

Figure 3.1: Micro fractographs of 3D printed samples using FDM. Different raster orientations plays and important role in mechanical behavior of parts [5].

In section 3.2, we will review literature on stress-constrained TO for both isotropic (3.2.1) and anisotropic (3.2.2) materials. In section 3.3 we will describe the proposed method and define the strength-based TO problem, perform sensitivity analysis (3.4) and present the Pareto algorithm (3.5). Finally, in section 3.6 we demonstrate the effectiveness of the proposed method through numerical and experimental results.

3.2 Strength-Based Optimization

3.2.1 Strength Optimization for Isotropic Materials

There are numerous failure criteria that have been developed for isotropic materials over the years; the most common ones are based on maximum principal stress by Rankine, maximum principal strain by St. Venant, total strain energy by Beltrami, maximum shear stress by Tresca, and octahedral shear stress by von Mises. Among these, Rankine is best suited for brittle materials and vonMises agrees best with ductile materials [68]. Earlier attempts towards producing strength-based optimum structural designs were mainly focused on shape optimization [69] and topology optimization of trusses [70]. It was believed by many [71; 72; 73] that the optimal design might be an isolated or singular point in the design space. For instance for truss optimization, as was shown by Kirsch [73], a singularity phenomenon occurs as the cross-section of a bar reaches its lower bound of zero. This, as explained later by Cheng and Jiang [74], was due to

discontinuity of the stress function and the fact that the constraint function of the optimization problem becomes undefined. Cheng and Guo [75] proposed an ε-relaxation method as a solution to this issue, where the singular optimum design was eliminated from the design space; consequently, sizing and topology optimization could be unified in a single framework (also see [76; 77]).

Density based approaches. Since the development of homogenization method by Bendsøe and Kikuchi [78] and Solid Isotropic Material with Penalization (SIMP) method by Bendsøe [79], many different strategies have been proposed for stress-based TO. For instance, Xie and Steven [27] proposed an evolutionary method, in which elements with lower von-Mises stress are gradually rejected. This approach could lead to sub-optimal designs, due to locality nature of stress [80].

Yang and Chen [81] used a global stress measure such as Kreisselmeier-Steinhauser or Park-Kikuchi as the objective function. In particular, their objective was a weighted average of compliance and the p-norm of a stress measure.

It is well-known that as ρ approaches 0, the stress values can become singular, which results in the same type of singularity phenomenon discussed above. In order to overcome this problem, Duysinx and Bendsøe [76], proposed an ε-relaxation scheme for SIMP. Bruggi and Venini [82] and Bruggi [83] proposed an alternative qp-approach to remedy the singularity problem, which required less computational effort. Le et al. [84] proposed a formulation based on normalized stress p-norm and a density filter to control length scale. Paris et al. [85], proposed a TO method considering local and global stress constraints. They later extended their work in [86] by developing block aggregated approach, where one stress constraint was assigned to a group of elements. As was shown in [76], TO with a global stress constraint can be too coarse and might yield results similar to those of stiffness optimization. The clustered approach can avoid stress concentrations and give better designs while not being too expensive. Along these lines, in [87], the number of stress constraints are reduced by clustering several stress evalua-

tion points into groups.

Level set approaches. In [88], Miegroet and Duysinx proposed a LS method to minimize the stress concentration of 2D fillets. The approach uses X-FEM, which enriches classical finite element method (FEM) with several discontinuous shape functions. Svanberg and Werme [89], presented two sequential integer programming methods, where a sequence of linear or quadratic sub-problems with decreasing mesh sizes are solved and on the fine level. A LS method was proposed in [90] to minimize stress of designs in 2D and 3D, where the Hamilton-Jacobi transport equation governs the evolution of the LS. Amstutz and Novotny [91] developed the topological derivatives for a stress-based objective function consisted of compliance, volume, and the p-norm of von Mises stress. Xia et al. [92] introduced a global measure of stress based on von Mises stress and Heaviside function. The sensitivity analysis was then carried out by solving an adjoint problem [93]. Finally, the optimization problem was solved using LS method. Suresh and Takalloozadeh[32] proposed a LS-based Pareto-front tracing algorithm. The proposed LS method used p-norm of von-Mises stress as the global measure to solve the optimization problem. Cai et al. [94] integrated LS function and B-spline finite cell method to improve the accuracy of stress and sensitivity evaluation. A combination of LS and augmented Lagrangian was introduced in [95], where stress constraints were assigned to a neighborhood of nodes to capture local effects while remaining continuous. Cai and Zhang [96] recently proposed an LS method for free-form design domains using Boolean operations. The method also exploits a dynamic aggregation technique to reduce the number of local stress constraints. Although the topological sensitivity is a well-established concept, it is mainly used when underlying material properties are isotropic, i.e. when closed-form gradients can be efficiently evaluated. Although there have been valuable theoretical contributions towards computing anisotropic topological sensitivities, they have not yet been employed in an optimization algorithm successfully. Schneider and Andrä [97] proposed a closed-form solution for topological sensitiv-

ity for materials with anisotropic constitutive properties, which involves considering ellipsoidal inclusions and computing Eshelby's tensor. Delgado and Bonnet [98] also proposed an asymptotic topological sensitivity for anisotropic stress functionals. In both cases the mathematical derivations are extremely complex and are yet to be exploited in an efficient optimization framework.

3.2.2 Strength Optimization for Anisotropic Materials

A generalization of von Mises criterion was introduced by Hill [99] for orthotropic materials. Later, Azzi and Tsai [100] presented another failure criterion, generally known as Tsai-Hill criterion that simplified Hill's criterion for unidirectional composites. However, Hill and Tsai-Hill criteria did not take into consideration the behavioral differences between tension and compression. This limitation was overcome by Hoffman [101] by including additional linear terms. Encompassing these ideas, Tsai and Wu [102] proposed a general criterion for anisotropic materials in the following tensor form,

$$\mathscr{F} = \sum_{j=1}^{6} \sum_{i=1}^{6} C_{ij}\sigma_i\sigma_j + \sum_{i=1}^{6} C_i\sigma_i \leq 1 \tag{3.1}$$

where:

$$\begin{aligned} &\sigma_1 = \sigma_{11} \qquad \sigma_2 = \sigma_{22} \qquad \sigma_3 = \sigma_{33} \\ &\sigma_4 = \sigma_{23} \qquad \sigma_5 = \sigma_{31} \qquad \sigma_6 = \sigma_{12} \end{aligned} \tag{3.2}$$

Often the coupling between shear terms can be neglected [103]; Equation 3.1 can then be reduced to that of Equation 3.3,

$$\mathscr{F} = \mathscr{A} + \mathscr{B} \leq 1 \tag{3.3}$$

where:

$$\begin{aligned}\mathscr{A} &= 2C_{12}\sigma_1\sigma_2 + 2C_{13}\sigma_1\sigma_3 + 2C_{23}\sigma_2\sigma_3 + \\ &C_{11}\sigma_1^2 + C_{22}\sigma_2^2 + C_{33}\sigma_3^2 + C_{44}\sigma_{23}^2 + C_{55}\sigma_{31}^2 + C_{66}\sigma_{12}^2 \\ \mathscr{B} &= C_1\sigma_1 + C_2\sigma_2 + C_3\sigma_3\end{aligned} \tag{3.4}$$

The coefficients are given by:

$$\begin{aligned}&C_1 = \frac{1}{X_t} - \frac{1}{X_c} \qquad C_2 = \frac{1}{Y_t} - \frac{1}{Y_c} \qquad C_3 = \frac{1}{Z_t} - \frac{1}{Z_c} \\ &C_{12} = \frac{-1}{2\sqrt{X_t X_c Y_t Y_c}} \qquad C_{13} = \frac{-1}{2\sqrt{X_t X_c Z_t Z_c}} \qquad C_{23} = \frac{-1}{2\sqrt{Y_t Y_c Y_t Y_c}} \\ &C_{11} = \frac{1}{X_t X_c} \qquad C_{22} = \frac{1}{Y_t Y_c} \qquad C_{33} = \frac{1}{Z_t Z_c} \\ &C_{44} = \frac{1}{S_{23}^2} \qquad C_{55} = \frac{1}{S_{31}^2} \qquad C_{66} = \frac{1}{S_{12}^2}\end{aligned} \tag{3.5}$$

where X_t, Y_t, Z_t are tensile strengths, X_c, Y_c, Z_c are compressive strengths, and S_{23}, S_{31}, S_{12} are shear strengths. Tsai-Wu criterion is widely used due to its 1) invariance with respect to basis, 2) symmetry, and 3) generality. It has also been used in the context of optimization. In order to optimize fiber orientations in composite laminates, Groenwold and Haftka [104] proposed a sensitivity analysis based on the Tsai-Wu criterion. However, it was shown in [104] that using a non-homogeneous failure index such as Tsai-Wu as the objective function would be load-dependent (sensitive to load intensity) and may result in counter-intuitive designs. To overcome these limitations, they proposed using the safety factor or strength-ratio discussed in the next section.

3.3 Optimization Problem

Consider the failure index in Equation 3.3:

$$\mathscr{A} + \mathscr{B} - 1 \leq 0 \tag{3.6}$$

Observe that this applies at each point within the domain, i.e., in practice, at each element within the mesh. For reasons, discussed above, it was proposed in [104] that one should consider the safety factor (also referred to as strength ratio), defined as the positive solution to the quadratic Equation 3.7,

$$\mathscr{A} s_e^2 + \mathscr{B} s_e + 1 = 0 \tag{3.7}$$

i.e.,

$$s_e = \frac{-\mathscr{B} + \sqrt{\mathscr{B}^2 + 4\mathscr{A}}}{2\mathscr{A}} \tag{3.8}$$

The goal therefore will be to maximize the safety factor at each element. Alternately, the goal is to minimize the failure index at each element, defined as:

$$\gamma_e = \frac{1}{s_e} \tag{3.9}$$

One can aggregate these failure indices via the p-norm ([32; 92; 105]) into a single global failure index:

$$\gamma = \|\gamma_e\|_p = \left(\sum_e (\gamma_e)^p\right)^{\frac{1}{p}} \tag{3.10}$$

In this chapter we will devise a TO framework based on the objective in Equation 3.10. Based on the discussion in the previous section, the TO problem considered in this here is:

$$\begin{aligned} &\underset{\Omega \subset D}{minimize}\{|\Omega|, \gamma\} \\ &J \leq \bar{J} \\ &\text{subject to} \\ &\mathbf{Ku} = \mathbf{f} \end{aligned} \tag{3.11}$$

where $\bar{J}$ is the (user defined) allowable compliance at the target volume fraction. Observe that (1) a compliance constraint is essential to avoid pathological conditions [106], (2) the failure criteria of Equation 3.3 is not explicitly imposed since it is absorbed into

the objective; however, this can be easily imposed as an additional check.

3.4 Sensitivity Analysis

To solve the TO problem of Equation 3.11 one must first compute the sensitivity of the objective and compliance constraint. To this end, let us consider the corresponding Lagrangian [64]:

$$\mathscr{L}(\Omega, \mathbf{u}) = \lambda_V |\Omega| + \lambda_\gamma \gamma + \lambda_J (J - \bar{J}) \tag{3.12}$$

where λ_V, λ_γ, and λ_J are the Lagrange multiplier associated with the volume, failure index, and compliance constraint, respectively. For solving the optimization problem, one must take the derivative of Lagrangian:

$$\mathscr{T}_{\mathscr{L}} = \lambda_V (-1) + \lambda_\gamma \mathscr{T}_\gamma + \lambda_J \mathscr{T}_J \tag{3.13}$$

which reduces to:

$$\mathscr{T}_{\mathscr{L}} = \lambda_\gamma \mathscr{T}_\gamma + \lambda_J \mathscr{T}_J \tag{3.14}$$

While closed-form expressions for the topological sensitivity of the compliance exist [31], a closed-form expression for the failure index does not exist. We will therefore consider an alternate *discrete element sensitivity*. Similar to Equation 3.13, the discrete sensitivity can be applied to the Lagrangian resulting in:

$$\mathscr{D}_{\mathscr{L}} = \lambda_\gamma \mathscr{D}_\gamma + \lambda_J \mathscr{D}_J \tag{3.15}$$

To compute $\mathscr{D}_\gamma$ we use the strategy proposed in [32]. Specifically, using the chain rule we have:

$$\mathscr{D}_\gamma = \left(\nabla_{\mathbf{u}} \gamma\right)^T \mathscr{D}(\mathbf{u}) \tag{3.16}$$

where $\mathscr{D}(\mathbf{u})$ is the change in displacement field due to the deletion of an element. One can show that this is given by:

$$\mathscr{D}(\mathbf{u}) = \left(\mathbf{K}^{-1}\Delta\mathbf{K}_e\right)\mathbf{u} \tag{3.17}$$

where $\Delta\mathbf{K}_e$ is the corresponding element stiffness matrix (mapped to the global indices). Substituting Equation 3.17 in Equation 3.16 leads to:

$$\mathscr{D}_\gamma = \left(\nabla_{\mathbf{u}}\gamma\right)^T\left(\mathbf{K}^{-1}\Delta\mathbf{K}_e\right)\mathbf{u} \tag{3.18}$$

Further, define the vector

$$\mathbf{g} \equiv \nabla_{\mathbf{u}}\gamma \tag{3.19}$$

In the Appendix C, it is shown that a computable expression can be derived for $\mathbf{g}$, i.e., $\mathbf{g}$ can be computed as a post-processing step. Thus, we have:

$$\mathscr{D}_\gamma = \mathbf{g}^T\mathbf{K}^{-1}\left(\Delta\mathbf{K}_e\right)\mathbf{u} \tag{3.20}$$

Now define and solve the adjoint problem:

$$\mathbf{K}\boldsymbol{\mu} = \mathbf{g}^T \tag{3.21}$$

Thus:

$$\mathscr{D}_\gamma = \boldsymbol{\mu}^T\left(\Delta\mathbf{K}_e\right)\mathbf{u} \tag{3.22}$$

This can be simplified to an element-wise construction,

$$\mathscr{D}_\gamma = \boldsymbol{\mu}_e^T\mathbf{K}_e\mathbf{u}_e \tag{3.23}$$

Thus, the element-wise discrete sensitivity of the Lagrangian is given by Equation 3.15.

3.5 Algorithm

Once the discrete sensitivity fields are computed, we can use the algorithm discussed in this section to solve the TO problem of Equation 3.11. The weights of Equation 3.15 can be dynamically computed through either the augmented Lagrangian method described, for example in [64] or equivalent as was proposed in [32] where the weights are updated as follows:

$$\begin{aligned} \mathscr{D}_{\mathscr{L}} &= w\mathscr{D}_{\gamma} + (1-w)\,\mathscr{D}_{J} \\ 0 &\leq w \leq 1 \end{aligned} \tag{3.24}$$

To begin with, the weight w is set to 1, i.e., the topology is entirely driven by the objective (to minimize anisotropic failure). The resulting sensitivity field is directly interpreted as a level-set, leading to the Pareto algorithms discussed in [61; 33; 32; 62; 65]. Using fixed-point iteration, the a small-step (that is dynamically modified) is taken along the Pareto curve. If the compliance constraint is violated the weight is reduced by a factor η (similar to the augmented Lagrangian method). The overall algorithm is illustrated in Figure 3.2 and the details are as follows:

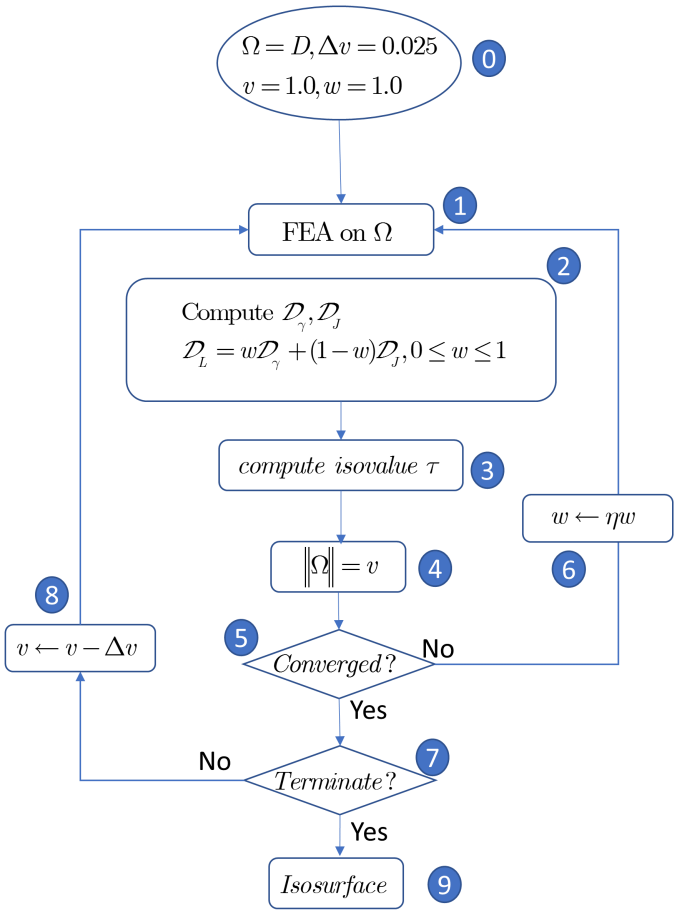

Figure 3.2: The proposed algorithm.

0. Initialization: we start with an initial design space D where current volume fraction v is set to 1.0, and at every TO step v is reduced by Δv (typically 0.025). The weighting factor η in Equation 3.24 is initialized to 1.0.
1. Solve the finite element problem on the current topology Ω. Compute discrete element sensitivity $\mathscr{D}_{\mathscr{L}}$ via Equations 3.15 and 3.23.
2. Compute level-set cutoff isovalue τ using fixed-point iteration.
3. Update topology.
4. Check if current τ has converged,
5. If not, reduce weight w by a factor $0 \le \eta \le 1$ (typically $\eta = 0.9$) and go to step 1.
6. Check if desired volume has been reached or any of the constraints are violated.

7. If not, reduce volume by Δv and repeat from step 1.

8. If yes, generate isosurface of the final design.

3.6 Experiments and Validations

In this section, we demonstrate the effectiveness of proposed method through numerical and experimental examples. Due to complexity of FDM-induced anisotropy, the experiments are conducted under the following assumptions.

Constitutive Properties. The (stress-strain) constitutive properties of FDM-printed parts are affected by numerous parameters. Here, we use the constitutive properties of ABS recently reported by Riddick et al. [67] considering $\pm 45^{\circ}$ raster orientation. It was reported in [67] that the primary constitutive properties namely, the Young's modulus and Poisson ratio were the same along both the raster orientation (S1) and build direction (V1), specifically, $E = 2.76GPa$ and $\nu = 0.38$. Thus, it exhibits isotropic constitutive properties (but not isotropic strength).

Anisotropic Strengths. For the Tsai-Wu failure criteria, 9 strength components (3 tensile, 3 compressive, and 3 shear) must be evaluated. We will use strength values reported in relevant literature (see Table 3.1. The three compressive strengths and three shear strengths are approximated according to the results reported in Ahn et al. [107] and Ahn et al.[108]. The three tensile strengths are assumed to be consistent with values reported in [67] considering $\pm 45^{\circ}$ raster orientation (S1 and V1). Note that these simplifications are merely a convenience; the topology optimization framework proposed in the chapter can handle alternate models.

Table 3.1: Material strengths.

Material	$\mathbf{X}_c$ (MPa)	$\mathbf{Y}_c$ (MPa)	$\mathbf{Z}_c$ (MPa)	$\mathbf{X}_t$ (MPa)	$\mathbf{Y}_t$ (MPa)	$\mathbf{Z}_t$ (MPa)	$\mathbf{S}_{yz}$ (MPa)	$\mathbf{S}_{zx}$ (MPa)	$\mathbf{S}_{xy}$ (MPa)
ABS (FDM)	38	38	35	29.62	29.62	**19.80**	10	10	10

Interaction Coefficients. The three in-plane interaction terms C_{12}, C_{13}, and C_{23} are expressed in terms of bi-axial strengths and are often not readily available, especially in 3D. The approximate values for these coefficients are consistent with [104] (see Equation 3.5). More careful examinations on the effects of geometry and print parameters on these parameters and subsequently Tsai-Wu criterion is required. For computing p-norm $p = 6$. All numerical experiments are performed on an off-the-shelf desktop with an Intel Core i7 @3.00GHz CPU and 16 GB memory.

3.6.1 Stiffness Versus Strength

In this example, we demonstrate why maximizing strength might yield a more suitable design than maximizing stiffness. To this end, let us consider the simple tensile test illustrated in Figure 3.3 where the geometry is a cube with dimensions of $5cm \times 5cm \times 5cm$. A unit force is applied at the center of top surface while four bottom corners are fixed. Bottom surface is retained for experimental purposes. The goal is to find the strongest design while 80% of material is removed. The domain is discretized into 50,000 hexahedral elements.

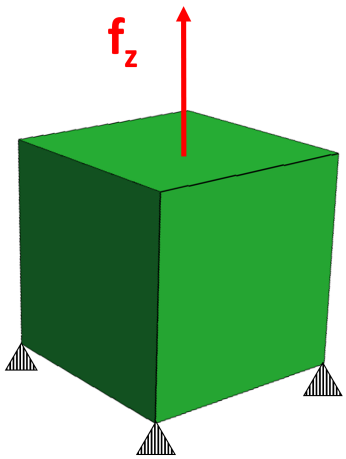

Figure 3.3: Tensile stool. Geometry and loading.

In order to compare the optimized design with respect to stiffness and strength, we first solve Equation 1.22 where the objective functional f is compliance. The optimized topology at 0.2 weight fraction is shown in Figure 3.4a. Next, we solve the proposed optimization problem of Equation 3.11, where weakness in tension along build direction is considered in the formulation. The optimized design is shown in Figure 3.4b.

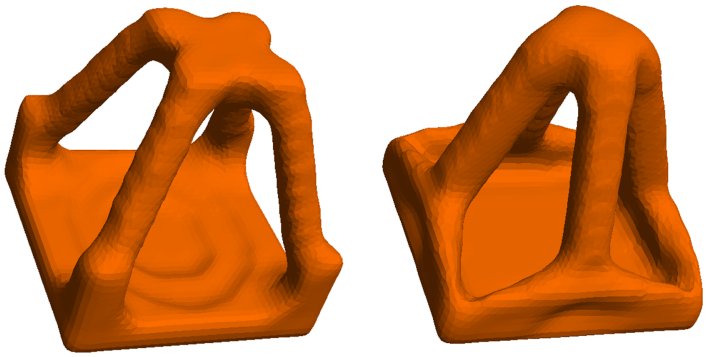

Figure 3.4: Tensile stool. Optimized design with respect to (a) Stiffness (b) Strength and weak in Z.

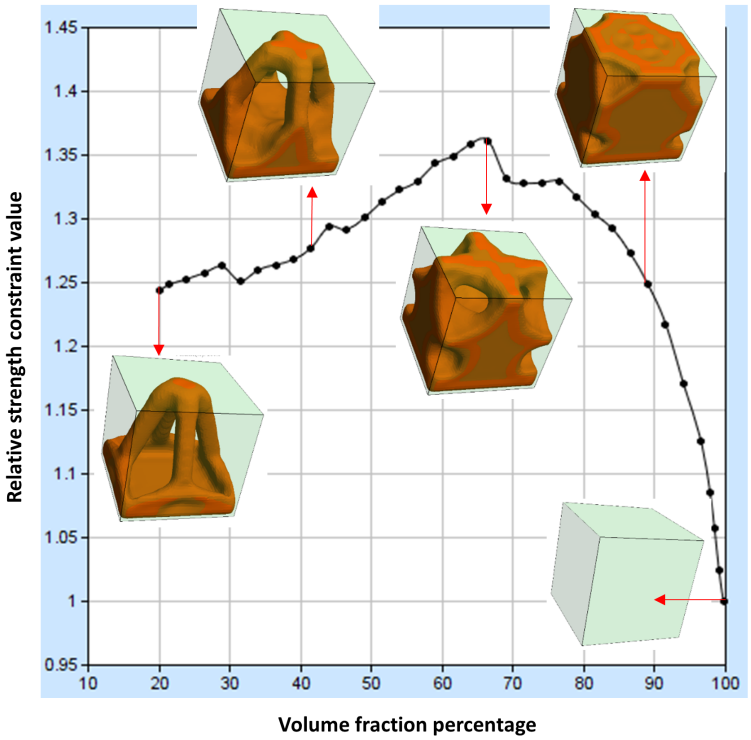

Figure 3.5: Tensile stool. Optimization process.

Figure 3.5 illustrates the change in γ throughout the optimization process for the second experiment. Observe that since the objective function is not self-adjoint, the Pareto front is also not convex.

Experimental Validation. To validate the numerical results, the designs of Figure 3.4 were printed and tested. An XYZ Da Vinci Duo was used to print four samples for each example. Samples were printed at 90% infill density (maximum allowable percentage by the software) with 2 shell layers. It is important to note that the build direction for all samples is the vertical direction and raster orientation is $\pm 45°$. The same generic brand of ABS was used to print the specimens. Tests were conducted using an MTS Criterion Model 43 system with 5 kN load cell. Built-in LVDTs measured the displacement between the grips. Displacement control tests were run at 5 mm/min with data collection rate of 100 Hz. Load and displacement were recorded for further analysis. Figure 3.6 illustrates the tensile test setup on an MTS criterion model 43 tensile actuator.

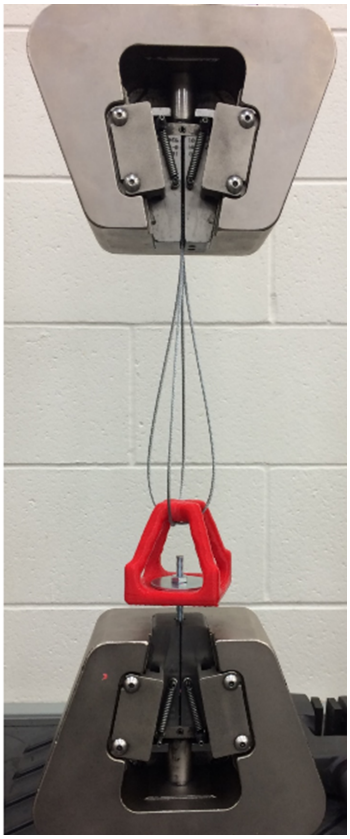

Figure 3.6: Tensile stool.tensile test setup for optimized stool designs.

Figure 3.7 illustrates the failed parts, observe that failure plane is perpendicular to the build direction.

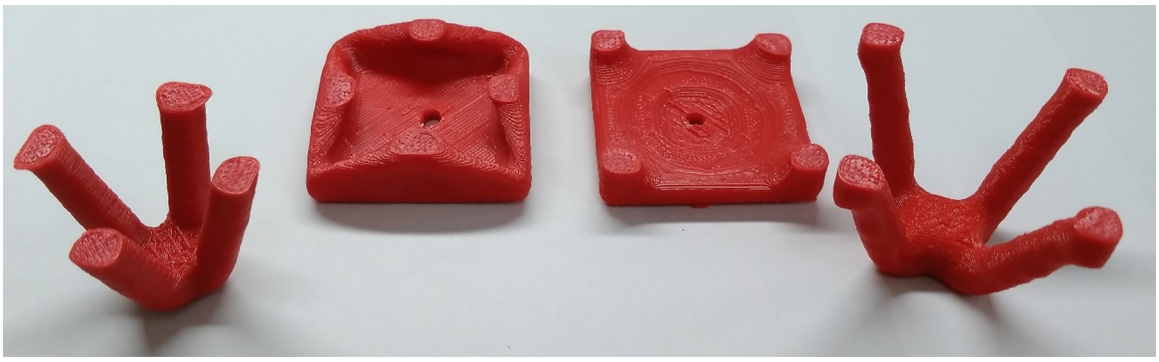

Figure 3.7: Tensile stool: tensile test, considering (left) anisotropic strengths and (right) stiffness.

Figure 3.8 summarizes the tensile test results. Four samples were tested per design. The design optimized for stiffness on average endured force of about 491 N, while this

was improved to 801 N for the optimized design considering strength and anisotropic behavior along build direction.

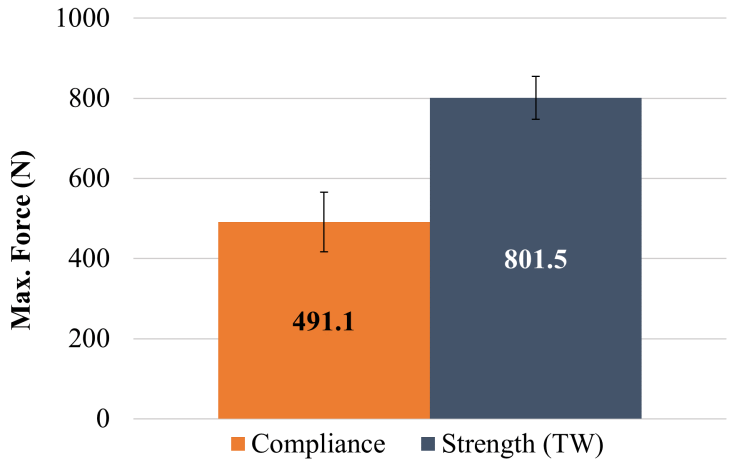

Figure 3.8: Tensile stool. Tensile test results.

Figure 3.9 illustrates the force-displacement graph of both tensile tests. Observe that the design optimized for strength has higher load capacity. Further, it is worth noting that both tests indicate brittle fracture, which in future needs to be incorporated optimization process.

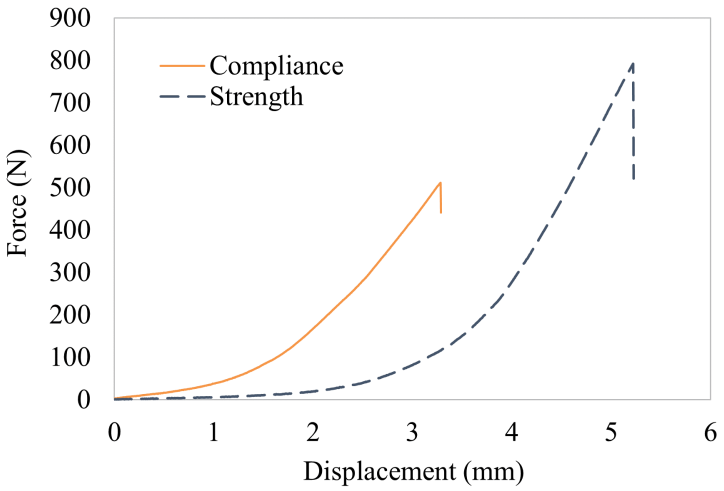

Figure 3.9: Tensile stool. Typical force-displacement graph.

3.6.2 Tension Versus Compression

In this experiment, we demonstrate that the proposed method captures the difference between tension and compression loading. Consider the C-bracket of Figure 3.10, where the bottom left surface is fixed. The domain is discretized into 20,000 hexahedral elements. In examples of Figure 3.10a and Figure 3.10b a downward and an upward force is acting at the right tip, causing the fillet to be under compression and tension, respectively. The objective is to find the strongest design while removing 50% of the material.

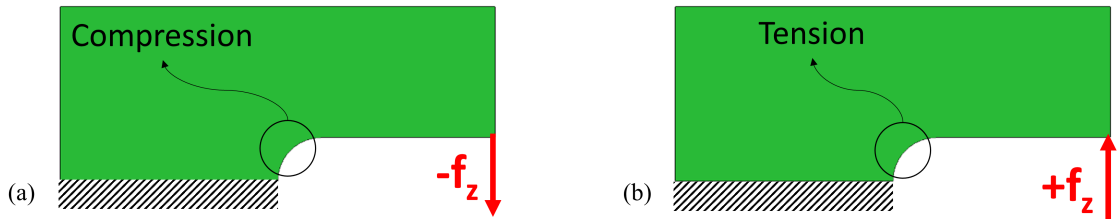

Figure 3.10: C-Bracket. Geometry and loading for (a) Compression at fillet and (b) Tension at fillet.

To compare the results, we first find the strongest design based on vonMises criterion [32], for which the result is shown in Figure 3.11a. Note that since vonMises does not capture directional preference, for both load cases the optimized design is the same. Observe that in the case of downward load, vonMises criterion fails to identify the actual failure region verified through experiment.

Next, the Tsai-Wu criterion was used to find the optimal topologies. Figure 3.11b illustrates the optimized design when the fillet is under compression. The optimized design is similar to that of Figure 3.11a with isotropic strengths. However, Tsai-Wu criterion successfully identifies the actual region of failure.

Figure 3.11c illustrates the optimized design when the fillet is under tension. Observe that in order to reduce stress concentration, the proposed optimizer increases the fillet radius. Moreover, Tsai-Wu criterion successfully identifies the actual failure point.

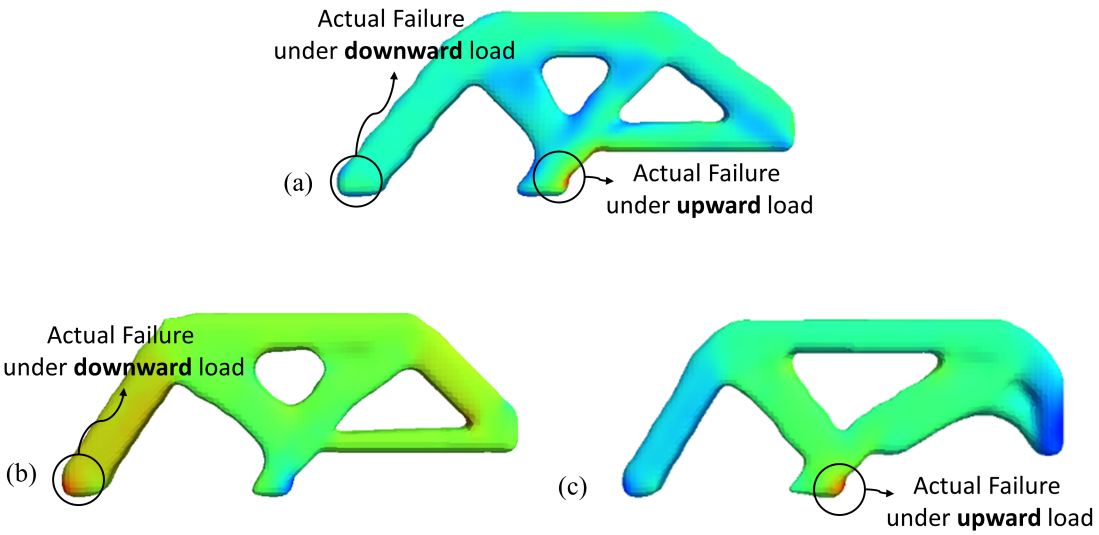

Figure 3.11: C-Bracket. Optimized designs with underlying stress field. a) Isotropic strength with vonMises field b) Weak Z compression at fillet with Tsai-Wu field and c) Weak Z tension at fillet with Tsai-Wu field.

Experimental Validation. To compare the performance of optimized designs under loadings of Figure 3.10a and Figure 3.10b, each design was printed using the same printer with the same printing parameters as mentioned before. The sample size is four for each design. A custom test fixture was designed to accommodate both tests in tension and compression. Testing parameters were also kept the same for the C-Bracket in both set of tests.

Figure 3.12 shows the test setup for exerting downward force and causing compression at fillet. Figure 3.13 shows the bending test results for C-bracket under compression. Results show a statistically equal strength for both designs. This conclusion agrees with von Mises and Tsai-Wu criteria predictions.

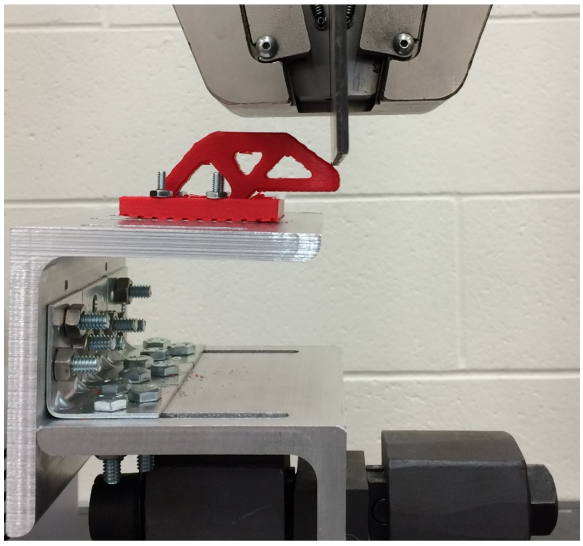

Figure 3.12: C-Bracket Fillet under compression, test setup.

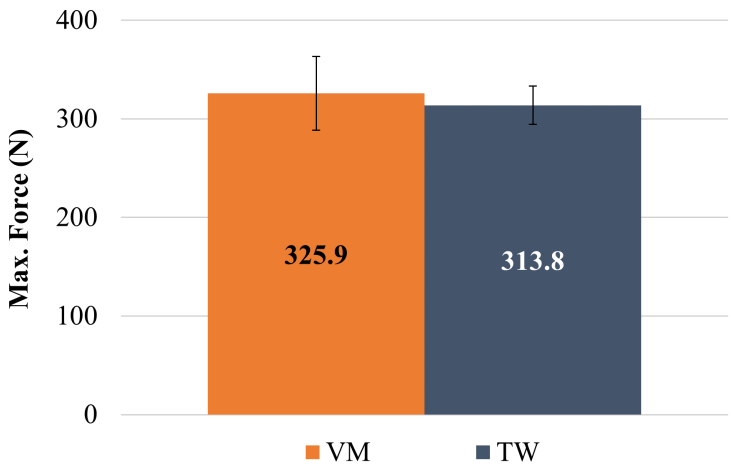

Figure 3.13: C-Bracket: fillet under compression, results.

On the other hand, results for bending test when C-bracket is under tension (Figure 3.14) favors heavily towards the design from Tsai-Wu criterion with an average maximum force of 116.1 N compared with maximum average force of 69.3 N (Figure 3.15).

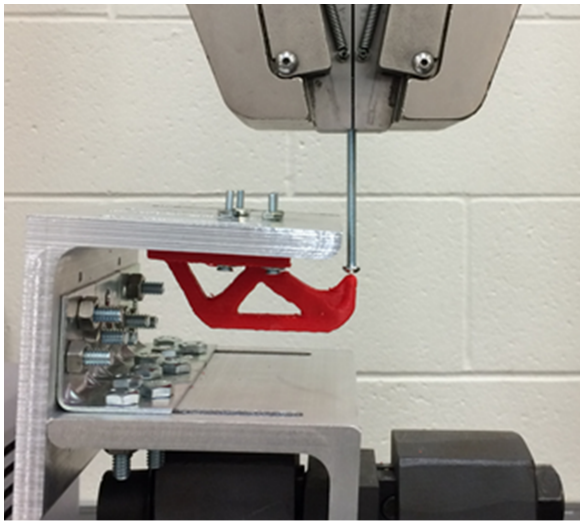

Figure 3.14: C-Bracket Fillet under Tension, test setup.

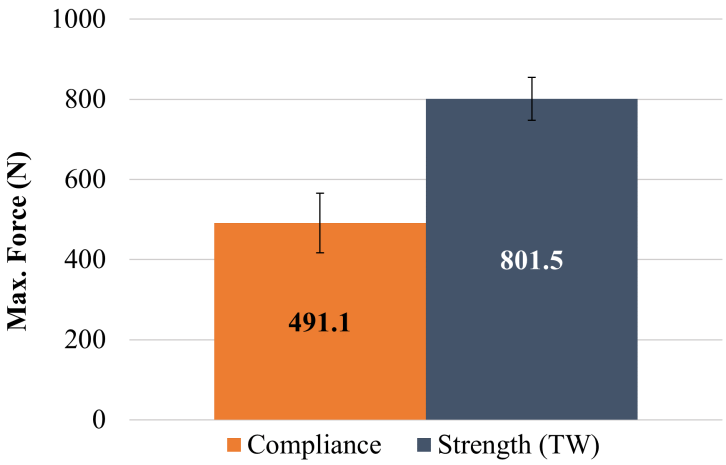

Figure 3.15: C-Bracket Fillet under Tension, results

It is also worth noting that the design of Figure 3.11a, which is optimized via von-Mises criterion, is about 4.7 times stronger under compressive load than tensile load. Since the failure plane is perpendicular to build direction, this is in agreement with the notion that FDM printed designs are much weaker in tension than compression along build direction.

3.7 Summary

In this chapter, we have proposed a method to compute strength sensitivity based on generalized failure criteria such as Tsai-Wu for anisotropic parts. For numerical experiments, we have focused on anisotropic strengths of additively manufactured parts where tensile strength along build direction is lower than other directions. Table 3.2 summarizes the results for the numerical examples.

Table 3.2: Summary of Experiments (VM: vonMises, TW: Tsai-Wu)

		Time (sec.)	**Rel. J**	**Rel. Objective**
Example	**#DOF**	**VM/TW**	**VM/TW**	**VM/TW**
Tensile stool	164,600	235/260	2.28/2.57	0.99/1.60
C-bracket (compression)	68,600	41/42	1.62/1.56	1.17/1.22
C-bracket (tension)	68,600	41/42	1.76/1.56	1.12/1.22

The proposed framework can be extended to also include constitutive anisotropy, which requires accurate tensile and shear measurements. Also, the fact that the materials is brittle must be taken into consideration through a more comprehensive fracture model and sensitivity analysis. Moreover, the current printing processes introduce uncertainty in the material behavior, considering robustness can also be beneficial. Furthermore, the sensitivity can be extended to strength-based multi-material topology optimization. For multiple materials, since each material has its own strength, vonMises criterion is inadequate and more generalized failure indices are suitable. However, local de-bonding effects must also be considered.

CHAPTER IV

Multiple Materials

4.1 Introduction

As additive manufacturing expands into using multiple materials, there is a demand for efficient multi-material topology optimization (MMTO), where one must simultaneously optimize the topology and the distribution of various materials within the topology. While MMTO has been addressed by many researchers, the objective of this chapter is to pursue a MMTO method that is computationally efficient and can be generalized to variety of objectives. In section 4.2, recent advances in MMTO are summarized. In 4.3, we formulate the MMTO problem, and carry-out the sensitivity analysis. In 4.4, we generalize the single-material Pareto-tracing method. In section 4.5, the validity of this method is confirmed through benchmark case-studies.

4.2 Related Work

For multi-material topology optimization (MMTO), the traditional single objective problem posed in Equation 1.1 is generalized to:

$$
\begin{aligned}
&\underset{\Omega_{k=1,\ldots,M} \subset D}{minimize}\, f(\Omega, \mathbf{u}) = \mathbf{f}^T \mathbf{u} \\
&\Omega_i \cap \Omega_{i \neq j} = \emptyset \qquad i, j = 1, .., M \\
&g_n(\Omega, \mathbf{u}) \leq 0 \qquad n = 1, ..., N \\
&\text{subject to} \\
&\mathbf{Ku} = \mathbf{f}
\end{aligned}
\tag{4.1}
$$

Where M is the number of materials and Ω_k is the topology for k th material to be computed.

Thus, the objective is to find the optimal distribution of M non-overlapping materials, within a given design space, that minimizes a specific objective and satisfies certain design constraints. The MMTO problem posed in Equation 4.1 assumes that every point within the design space has a distinct material associated with it (or is void). This differs from functionally graded material optimization [33], where a mixture of base materials is allowed.

Density-based MMTO. For multiple materials, the density approach was first extended to multiple materials in 1992 [109]. However, the challenges associated with assigning different interpolations for different materials and material properties were discussed in [20], where Sigmund proposed a two-material interpolation scheme for designing thermally and electro-thermally driven micro actuators. An alternate material interpolation strategy was developed in [110] by introducing a peak function and exploiting optimality criteria method.

A new density method was presented in [111] for optimizing multiple homogeneous materials, which interpolates the stiffness matrix instead of interpolating the Young's

modulus. The validity of this method was demonstrated through 2D examples involving two materials. In [112], Chavez et al. implemented SIMP to solve a special problem of minimizing the compliance of concrete slabs reinforced with carbon fibers. Their approach relies on concrete failure criteria, and the fact that the slabs are simple symmetric geometries in 2D. In 2007, De Kruijf et al. employed SIMP to minimize both compliance and resistance to heat dissipation of composites. The method is in 2D and attains only the upper limits of Hashin-Shtrikman [113]. If the materials are composites, it is well-known that SIMP interpolations can violate Hashin-Shtrikman bounds [114]. Blasques and Stolpe proposed a density-based framework for minimizing compliance of laminated composite beam cross sections [115]. The method allows multi-material laminates in 2D, where the formulation is carried out by writing equilibrium between laminate layers, under the limiting assumptions that the beam is slender and has invariant cross sections.

A new multi-resolution scheme for MMTO was developed in [116] where different levels of discretization were employed for representing displacement, design variables, and density. The method uses the alternating active phase algorithm, in which the original problem is decomposed into a number of sub-problems, where only two of the materials are active, and the problem is solved using the density approach.

Level-Set MMTO. In 2003, Wang and Wang introduced a novel level-set approach for MMTO [117]. The method requires M level-sets to represent 2^M distinct materials, and it was used to solve benchmark problems in 2D, where different *colored level-sets* represented distinct materials.

Later, the idea was expanded towards compliant mechanism design [118] and microstructures [119]. Unfortunately, as demonstrated in [120], these shape derivatives were approximations under certain assumptions. Allaire et al. developed the correct mathematical shape derivatives in [120] where the interface zone thickness is also kept constant. In order to remove discontinuity caused by sharp interfaces, authors of [121] suggested

using multiple intermediate interfaces to attain continuity. The most challenging issues in MMTO via level-set are: (1) field discontinuity, and (2) thickness diffusion. The former is due to discontinuity in phase properties, which leads to discontinuous normal strain and tangential stress. The latter is caused by numerical diffusion in level-set process [120].

More recently, as an improvement over the idea proposed in [117], a new multi-material level-set method was proposed in [122] for both shape and topology optimization. While exact sensitivity expression were provided, the implementation was restricted to 2D.

Evolutionary methods for MMTO. Yet another family of topology optimization methods are the evolutionary-based methods. Xie and Steven [27], first developed evolutionary structural optimization (ESO) in 1992, to solve optimization problems by gradually removing elements with lowest value of von-Mises stress until the desired volume fraction is reached. In 1996, stiffness-constrained optimization problems were solved using ESO, where the sensitivity number of each element was calculated using strain energy[28]. Querin et al. expanded the *hard-killing* ESO to BESO, which allowed the discarded elements to be re-added under certain circumstances [24]. An AESO approach was introduced in [29], which instead of discarding elements from a larger-than-optimum design, added elements to a minimum base design. In AESO, unlike ESO one could use maximum criterion directly in evolution process. Liu et al. developed a GESO algorithm, wherein a chromosome array was assigned to each element, and an element was removed only if all values of genes were zero [25]. The salient features of the ESO family are that they do not introduce intermediate elements and do not compute gradients. Thus, most of these methods fall into the category of non-gradient topology optimization (NGTO) methods, whose deficiencies are discussed in [123].

Element Sensitivity methods for MMTO. In 2010, Ramani developed an algorithm for compliance minimization for multiple materials [124]. The algorithm starts with computing and ranking element sensitivities, where for each element, there are generally

two values defined as sensitivity to change from current state to an immediate step, both better and worse performance. Then material distribution undergoes a repeated cycle between feasible and infeasible solutions until it converges. Ramani extended his work in 2011 to stress-constrained multi-material topology optimization [125].

The present work once again uses the concept of element sensitivity, as in [124]. Further, the element sensitivity is generalized to arbitrary quantities of interest.

In [124], the intermediate designs may be structurally disconnected. Therefore, as the author states, it is critical that void elements be assigned a low value of Young's modulus. In the present work, by construction, every intermediate design is connected, and void elements can be suppressed without resulting in singularity. This leads to better condition number, and faster convergence.

Displacement constraint are handled in [124] by switching between *infeasible* and *feasible* designs. In this framework, all intermediate designs satisfy the displacement constraint. Thus, the designer has the option of choosing from a multitude of Pareto-optimal designs, as the numerical experiment later illustrates. The material changes in [124] are restricted; this may lead to sub-optimal designs; this is illustrated later through numerical experiments.

4.3 Formulation

4.3.1 Volume vs. Mass

In this section, we will compare two common formulations used in MMTO, namely volume-based and mass-based. The two objective give identical results in SMTO, since the density is constant over the entire domain. However these objectives are not necessarily equivalent in a non-homogeneous topology optimization, an important fact that is often neglected.

For simplicity, consider the following volume-constrained formulation to find the stiffest

design at some volume fraction [119]:

$$
\begin{aligned}
&\underset{\Omega_{k=1,\ldots,M}\subset D}{minimize}\, J(\Omega,\mathbf{u}) = \mathbf{f}^T\mathbf{u} \\
&|\Omega| \leq V^* \\
&|\Omega_k| \leq V_k^* \\
&\Omega_i \cap \Omega_{i\neq j} = \emptyset \qquad i,j = 1,..,M \\
&g_n(\Omega,\mathbf{u}) \leq 0 \qquad n = 1,...,N \\
&\text{subject to} \\
&\mathbf{Ku} = \mathbf{f}
\end{aligned}
\tag{4.2}
$$

where J is compliance, $|\Omega|$ is the total volume, $|\Omega_k|$ is volume of k^{th} material. Basically we are seeking the stiffest design while some volume constraints on each material phase as well as total volume are satisfied. Also, there are no overlaps between two different phases. Immediately we can see that in order to start the optimization process with the above formulation, we *must* have a very good approximation for the optimum volume of each material. However, this is clearly not a simple task for complex designs and loading conditions. Further, as mentioned by Gao and Zhang [6] , imposing these additional linear constraints will reduce the feasible design space to only a subset of the actual design space.

Now let us consider the following mass-constrained formulation:

$$
\begin{aligned}
&\underset{\Omega_{k=1,\ldots,M}\subset D}{minimize}\, J(\Omega,\mathbf{u}) = \mathbf{f}^T\mathbf{u} \\
&\sum_{k=1,\ldots,M} \rho_k V_k \leq \bar{\mathscr{M}} \\
&\Omega_i \cap \Omega_{i\neq j} = \emptyset \qquad i,j = 1,..,M \\
&g_n(\Omega,\mathbf{u}) \leq 0 \qquad n = 1,...,N \\
&\text{subject to} \\
&\mathbf{Ku} = \mathbf{f}
\end{aligned}
\tag{4.3}
$$

In other words, we are looking for the stiffest design while total mass of our design is less than some upper bound $\bar{\mathcal{M}}$. Observe that with Equation 4.3, we need not know the amount of each material prior to optimization. Further, in the absence of additional linear constraints, we are more likely to converge to the minimum compliance of all possible combinations of multiple material distributions. This is illustrated in Figure 4.1 borrowed from [6].

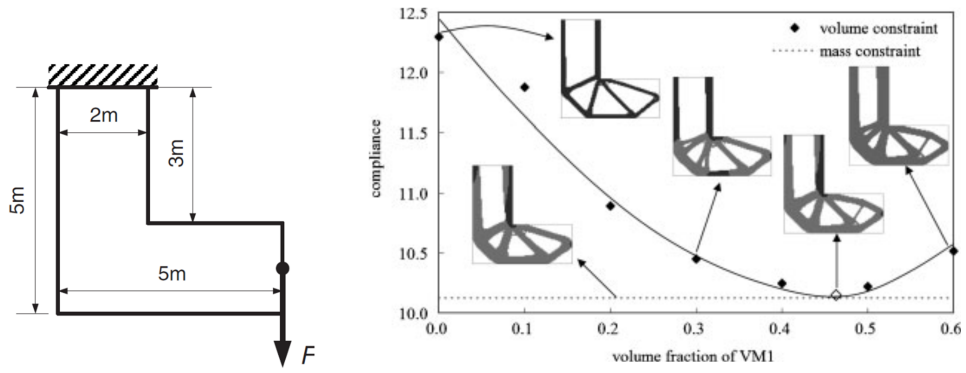

Figure 4.1: (a) Design Space and Boundary Condition (b) Comparison between results under mass and volume constraints with the equal mass [6].

Hence, we will present a formulation based on mass and later consider a more general objective function. Next, we will propose a multi-objective form of Equation 4.3 and discuss its advantages.

4.3.2 Multi-Objective Formulation

Most of the previous work on MMTO consider a single objective such as compliance and impose a constraint on mass. Alternatively, we can pose the problem in the follow-

ing multi-objective form:

$$
\begin{aligned}
&\underset{\Omega_{k=1,\ldots,M}\subset D}{minimize}\{J,\mathscr{M}\}\\
&\sum_{k=1,\ldots,M}\rho_k V_k = \mathscr{M}\\
&\Omega_i \cap \Omega_{i\neq j} = \emptyset \qquad i,j = 1,..,M\\
&\text{subject to}\\
&\mathbf{Ku} = \mathbf{f}
\end{aligned}
\tag{4.4}
$$

Now we can solve this modified MMTO problem using the so-called Pareto frontier. This will be discussed in more details in section 2.3, but first, let us complete this section by generalizing Equation 4.4.

Generally, we consider any two conflicting quantities, namely cost (C) and performance. Typical quantities that represent cost include *weight* and *price (in dollars)* that must be minimized, while performance metrics include *stiffness*, *strength*, etc. that must be maximized. However, to be consistent with classic multi-objective optimization, where all quantities are minimized, we define inefficiency (I) as the inverse of performance. Consequently, the multi-material problem will be posed as:

$$
\begin{aligned}
&\underset{\Omega_{k=1,\ldots,M}\subset D}{minimize}\{I,C\}\\
&\Omega_i \cap \Omega_{i\neq j} = \emptyset \qquad i,j = 1,..,M\\
&\text{subject to}\\
&\mathbf{Ku} = \mathbf{f}
\end{aligned}
\tag{4.5}
$$

For example, for compliance (J) as Inefficiency and mass ($\mathscr{M}$) as Cost, we get the Equation 4.4.

Assuming that the underlying design has been discretized using finite elements, and each element can be associated with a material of choice. Suppose we have a finite element with material k within the design. We will now consider a hypothetical swapping

of the underlying material k to material m. Observe that the change in compliance (I is used here to denote inefficacy) is given by the first-order element sensitivity (see Appendix A):

$$\Delta I_e^{k\to m} = \mathbf{u}_e^T \mathbf{K}_e^k \mathbf{u}_e - \mathbf{u}_e^T \mathbf{K}_e^m \mathbf{u}_e \tag{4.6}$$

As a special case, if the element is deleted, i.e., replaced with void, we have:

$$\Delta I_e^{k\to \emptyset} = \mathbf{u}_e^T \mathbf{K}_e^k \mathbf{u}_e \tag{4.7}$$

Similarly, as a special case of Equation 4.6, if a new element is inserted (in place of a void):

$$\Delta I_e^{\emptyset\to m} = -\mathbf{u}_e^T \mathbf{K}_e^m \mathbf{u}_e \tag{4.8}$$

Note that the above equation is consistent with the sensitivity expressions used in SIMP for compliance [9]. The element sensitivity in Equation 4.6 can obviously be generalized to other quantities of interest. Specifically, for any quantity of interest Q, the first-order sensitivity is given by (see Appendix A):

$$\Delta I_e^{k\to m} = -\boldsymbol{\lambda}_e^T \mathbf{K}_e^k \mathbf{u}_e + \boldsymbol{\lambda}_e^T \mathbf{K}_e^m \mathbf{u}_e \tag{4.9}$$

Where $\boldsymbol{\lambda}$ is the adjoint field associated with the quantity of interest. Thus, there is no fundamental restriction of the proposed method to compliance problems. The specific expression for the adjoint depends on the quantity of interest; for example, for the p-norm stress, an expression for the adjoint is derived in [32].

Correspondingly, the change in cost can also be computed; for example, if the cost is the mass function:

$$\Delta C_e^{k\to m} = \rho^m V_e - \rho^k V_e \tag{4.10}$$

where ρ denotes (real) material density and V_e denotes volume of an element.

4.4 Algorithm

Our objective is to trace the Pareto curve involving these two quantities with cost (C) on the x axis and inefficiency (I) on the y axis. For simplicity, let us for now assume that the initial optimum design is known; for instance the most expensive material also performs best and there are no materials with the same cost. We shall discuss finding the initial Pareto design in case of ambiguities in section 4.4.6. The proposed algorithm will start with a topology with the highest cost and optimized material distribution and trace Pareto front through a series of fixed-point iterations.

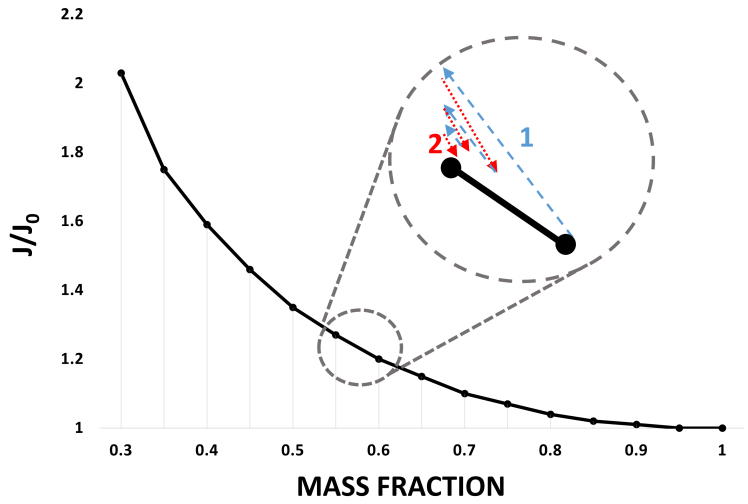

Figure 4.2: Tracing Pareto curve, and the two sub-steps.

To ensure that each optimization step results in a Pareto-optimal design, each step consists of two sub-steps, where (1) the cost function will be reduced by a small decrement (sub-algorithm 1), followed by (2) a reduction in inefficiency (sub-algorithm 2); these two steps are illustrated in Figure 55. By repeating these two steps, we show that the Pareto curve can be generated, and associated topologies computed, in an efficient and unambiguous manner.

4.4.1 Reducing Cost

Now consider the cost-inefficacy plot of Figure 4.3. In this sub-step, our objective is to reduce cost, i.e., we swap materials only if $\Delta C_e^{k\to m} < 0$. The change in inefficacy can be either positive or negative Therefore, only quadrants 2 and 3 in Figure 4.3 are acceptable; quadrant 3 is preferable, since both cost and inefficacy are reduced. Thus the angle θ must be maximized, i.e.,

$$\begin{aligned} &\underset{m}{maximize}\,\theta_e^{k\to m} \equiv \frac{\Delta I_e^{k\to m}}{\Delta C_e^{k\to m}} \\ &\text{subject to} \\ &\Delta C_e^{k\to m} < 0 \end{aligned} \tag{4.11}$$

or equivalently:

$$\begin{aligned} &\underset{m}{minimize}\,-\theta_e^{k\to m} \equiv \frac{-\Delta I_e^{k\to m}}{\Delta C_e^{k\to m}} \\ &\text{subject to} \\ &\Delta C_e^{k\to m} < 0 \end{aligned} \tag{4.12}$$

Hence, in the first sub-step, for each element, we find the material m that gives the lowest value of $-\theta_e^{k\to m}$.

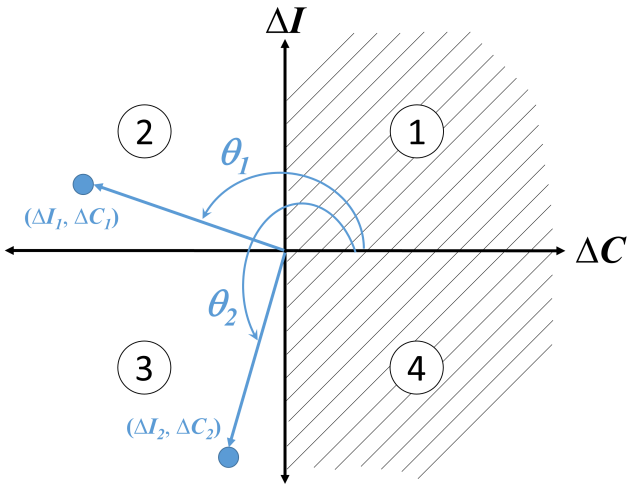

Figure 4.3: Reducing Cost.

4.4.2 Reducing Inefficiency

Now consider the cost-inefficacy plot of Figure 4.4. In this sub-step, our objective is to reduce cost, i.e., we swap materials only if $\Delta I_e^{k\to m} < 0$. The change in cost can be either positive or negative Therefore, only quadrants 3 and 4 in Figure 4.4 are acceptable; considering proper normalization, we try to stay as close as possible to $\theta_e^{k\to m} = \frac{3\pi}{2}$.

$$\begin{aligned} &\underset{m}{minimize} |\theta_e^{k\to m} - \frac{3\pi}{2}| \equiv sign(\Delta C_e^{k\to m}) \frac{\Delta I_e^{k\to m}}{\Delta C_e^{k\to m}} \\ &\text{subject to} \\ &\Delta I_e^{k\to m} < 0 \end{aligned} \tag{4.13}$$

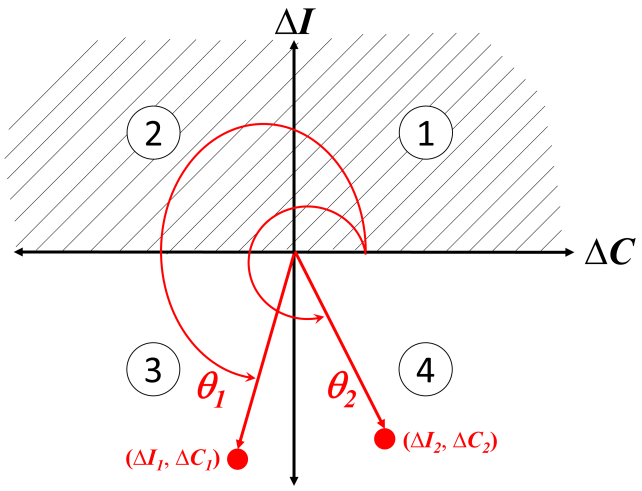

Figure 4.4: Reducing Inefficiency.

4.4.3 Main algorithm

The main algorithm is illustrated in Figure 4.5 and each of the steps is described below.

1. Start with an initial design with $\Omega = D$ and maximum cost (example, maximum weight).

2. The cost C is reduced by ΔC, either by removing material or replacing the most costlier material one with the less expensive one (see sub-step 1 for details).
3. Inefficiency I is reduced while maximum of N number of elements can be modified. The cost can increase or decrease. (see sub-step 2 for details)
4. Check if the converged design is acceptable:
5. If Step-3 fails, reduce ΔC and repeat
6. If the design has converged to the desired cost C, optimization is terminated
7. (Else) ΔC is reinitialized, and algorithm returns to step 1.

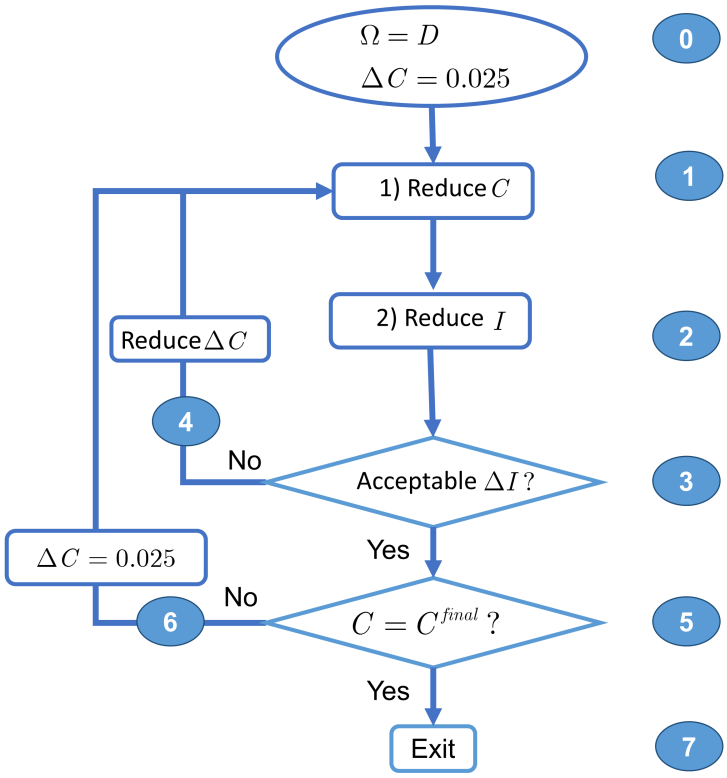

Figure 4.5: Main algorithm.

4.4.4 Sub-step 1: Reduce Cost C

The sub-algorithm 1 is illustrated in Figure 4.6, and each of the steps is described below.

1. We first perform a finite element analysis and compute the inefficiency for each element.
2. Next, for *each element* we find the ranking parameter $r(e)$.
3. In the next step, we sort the array r in an increasing order while keeping track of corresponding material and element.
4. Initialize counter i and the current reduction in C in this step (δC) to zero.
5. Replace elements with a new material or void, accordingly.
6. Update values of δC and i.
7. Check if we have reached the allowed ΔC .
8. (Yes) Update C and go to sub-step 2
9. (No) return to 1.5

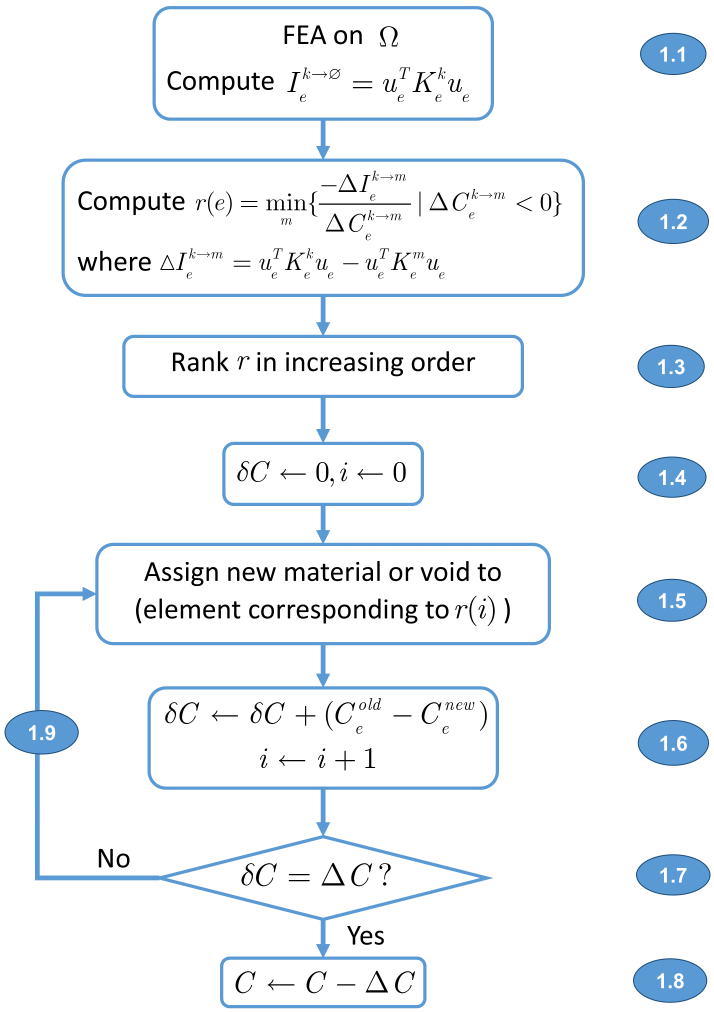

Figure 4.6: Sub-algorithm 1, reducing C.

4.4.5 Sub-step 2: Reduce Inefficiency at Constant C

Figure 4.7 shows the sub-algorithm 2, and each of its steps is explained herein.

1. We first perform a finite element analysis and compute the inefficiency for each element
2. Next, for each element we find the ranking parameter $r(e)$.
3. In the next step, we sort the array r in an increasing order while keeping track of corresponding material and element.

4. Initialize counter i and the current reduction in C in this step (δC) to zero.
5. Replace elements with a new material or bring back void elements, accordingly.
6. Update values of (δC) and i.
7. Check if we have reached the allowed number of element changes N.
8. (Yes) Update C and go to sub-step 2
9. (No) return to 2.5

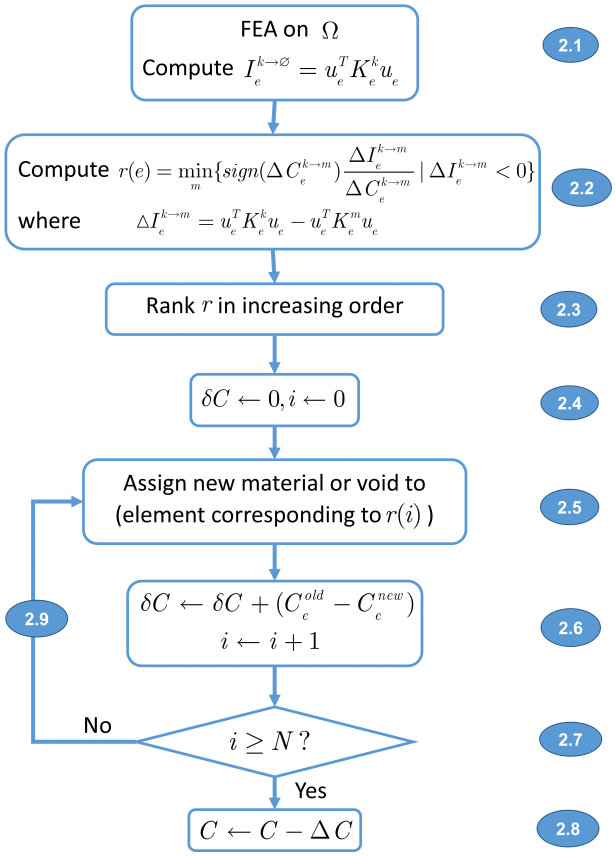

Figure 4.7: Sub-algorithm 2, reducing inefficiency.

4.4.6 Initial Material Distribution

In the last section, it was assumed that the initial material distribution is uniquely known as *a priori*. However, this may not be the case when materials have the similar costs or directional dependence, e.g. composites. Finding initial optimal design is

addressed in this section, where the material distribution (and possibly geometry) is optimized while the cost is remained a constant. The algorithm is essentially a special case of the main algorithm of Figure 4.5, where we begin with some sub-optimal distribution of material and successively apply sub-algorithms 1 and 2 with similar ΔC, until we find a local optimum which lies on the Pareto frontier.

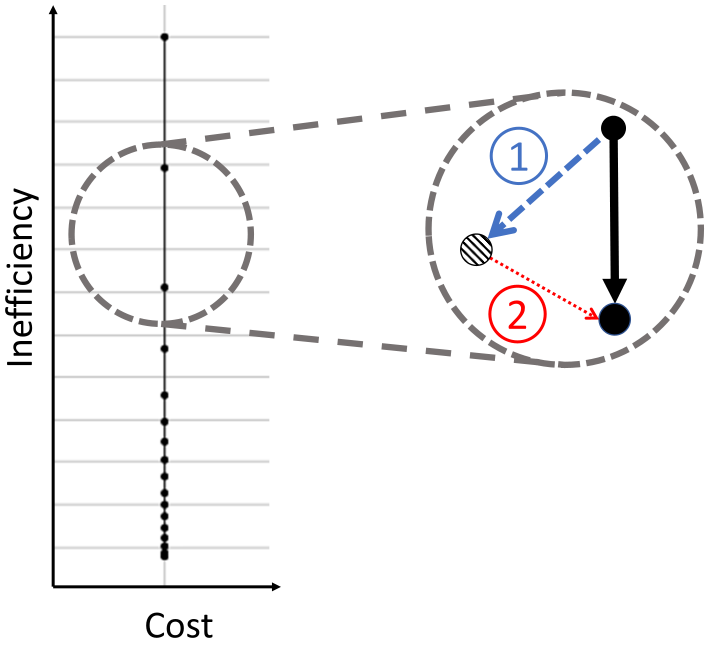

Figure 4.8: Optimizing design at the same cost.

4.5 Numerical Validations

In this section, we demonstrate the validity of the proposed method through several 3D examples. In Section 4.5.1, the single-material compliance minimization of the classic L-bracket is compared against a two-material compliance minimization. This experiment illustrates that, for a given weight fraction, the two-material design is less compliant (i.e., stiffer) than the single material design. In addition, the condition numbers of the underlying stiffness matrices for single and multiple materials are compared.

In Section 4.5.2, the effectiveness of the filtering method is illustrated through a mesh independency study on the classic MBB structure. In Section 4.5.3, three materials are considered for a benchmark problem. As expected, for a given weight-fraction, adding a material choice improves the performance. In Section 4.5.4, we consider a 3D case study for mount bracket using 2 available metal-infill filaments. Finally, in Section 4.5.5, the computational costs (running time and memory required) for all the above experiments are summarized. In all numerical experiments, the decrement in the cost function for Pareto tracing is initialized to 0.025. All dimension are in meters, unless otherwise noted. In all tables, E, ν, and ρ denote Young's modulus, Poisson ratio, and density, respectively. For all experiments, we rely on the assembly-free deflated conjugate gradient (CG) discussed in [126], with a tolerance set to 10^{-8}.

4.5.1 L-Bracket: Single and Two-Material Design

First, we consider the L-bracket illustrated in Figure 4.9a and compare the optimized results for: (1) a single material A, and (2) two materials A and B, whose properties are summarized in Table 4.1. The mass serves as the cost function while compliance is the measure of inefficiency; 20,000 elements are used for both experiments.

Table 4.1: Material Properties of A and B.

Material	$E(GPa)$	ν	$\rho(Kg/m^3)$
A	170	0.3	7100
B	70	0.33	2700

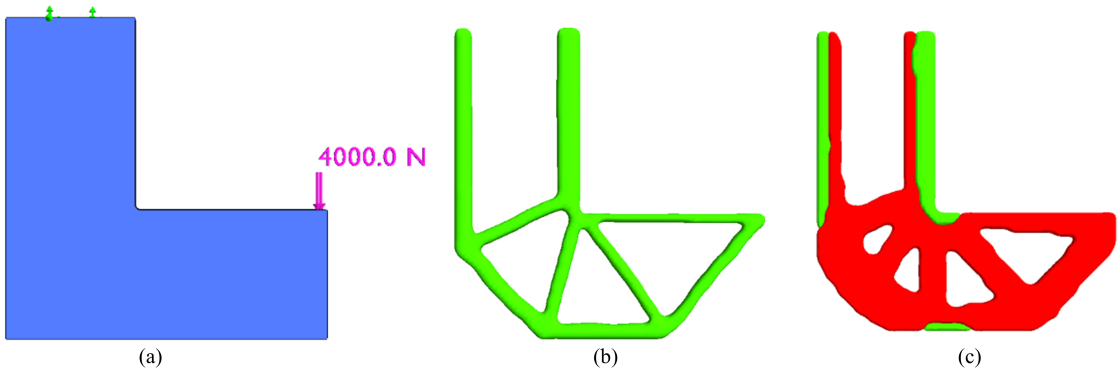

Figure 4.9: (a)L-bracket geometry and loading condition, (b) design at 30% cost using only material A and (c) design at 30% cost using materials A and B.

The Pareto curve is generated for up to 70% reduction in mass. As stated earlier in the algorithm, we start with the heaviest design (all A) and optimize the topology and material distribution. After the optimization process is complete, we obtain the two Pareto curves illustrated in Figure 4.10. As expected, for a given weight fraction, the two-material design is less compliant (stiffer) than the corresponding single material design.

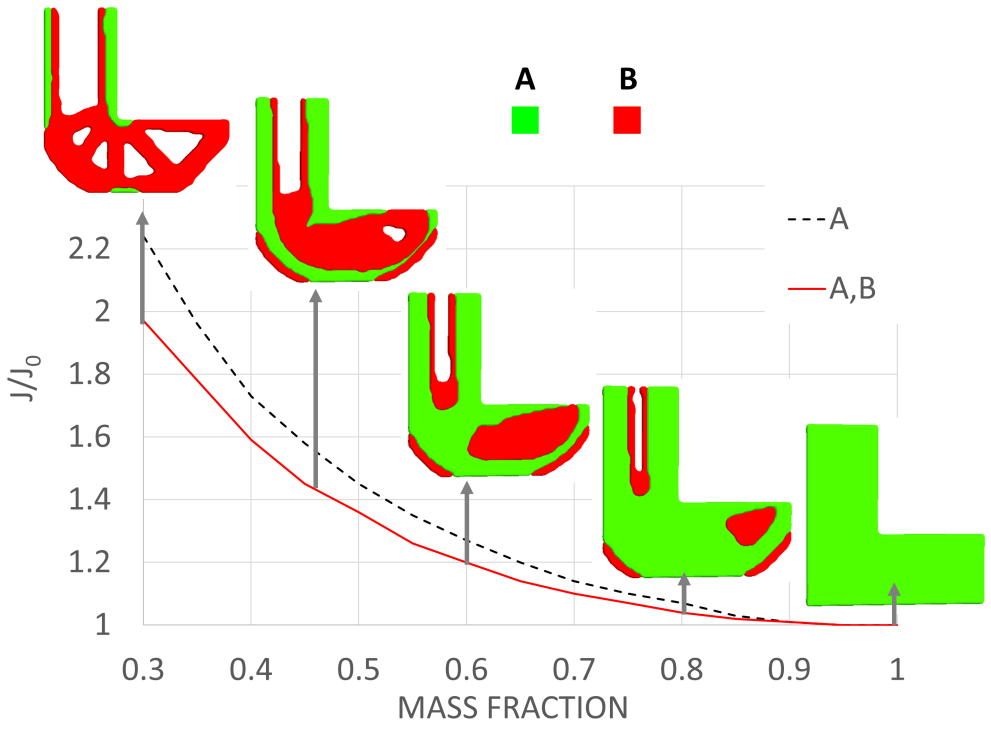

Figure 4.10: The Pareto curves and topologies for single material (A) and two materials (A and B).

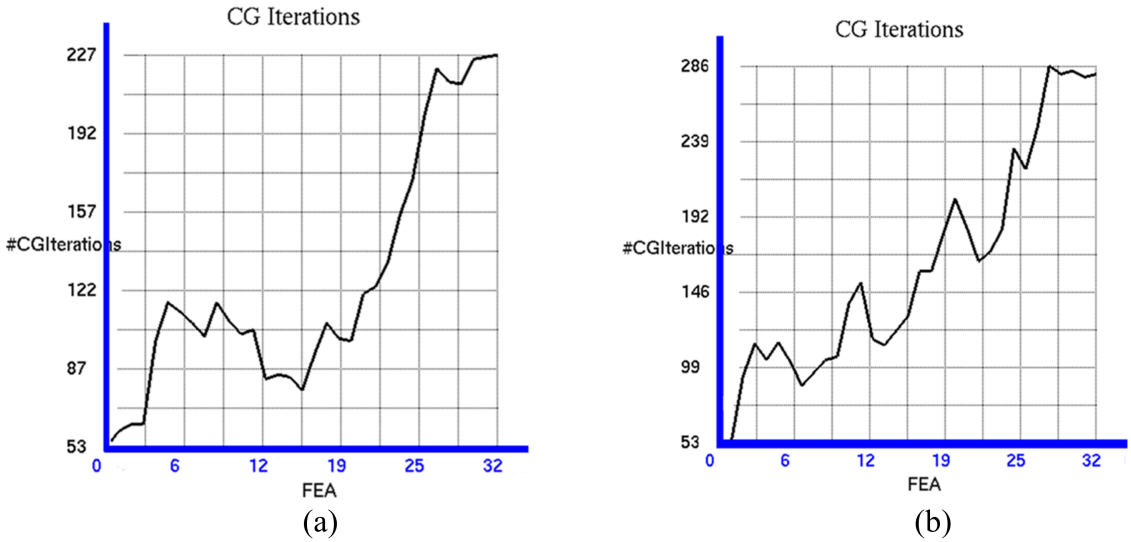

Figure 4.11: CG iterations for the L-Bracket with (a) single material A, (b) two materials A and B.

Figure 4.11 illustrates the number of deflated CG iterations for each of the 32 FEAs

during optimization. Figure 64a corresponds to single-material, while Figure 64b corresponds to multi-material. As one can observe, the iterations increase moderately in both scenarios; this can be attributed to the presence of thin/slender structures in the topology. Both experiments required 32 finite element operations to complete. Thus, for this example, the cost of multi-material design is almost exactly the same as the single-material design.

4.5.2 MBB Structure: Mesh Independency

In this example, we study the impact of mesh size using the classic MBB structure illustrated in Figure 4.12. The structure is loaded with 30 units at the center, and 15 units on either side of the center; the material properties are given in Table 4.1.

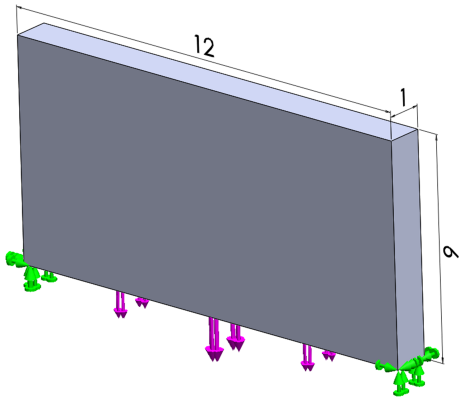

Figure 4.12: MBB structure.

Figure 4.13 illustrates the Pareto curves with 10,000 and 40,000 elements; as one can observe, the two curves are almost identical, suggesting that the method is insensitive to mesh discretization.

The final topologies are illustrated in Figure 4.14. Note that as the mesh size increases, the design details are a bit refined as expected. Yet the distribution of the material within the two designs are quite similar.

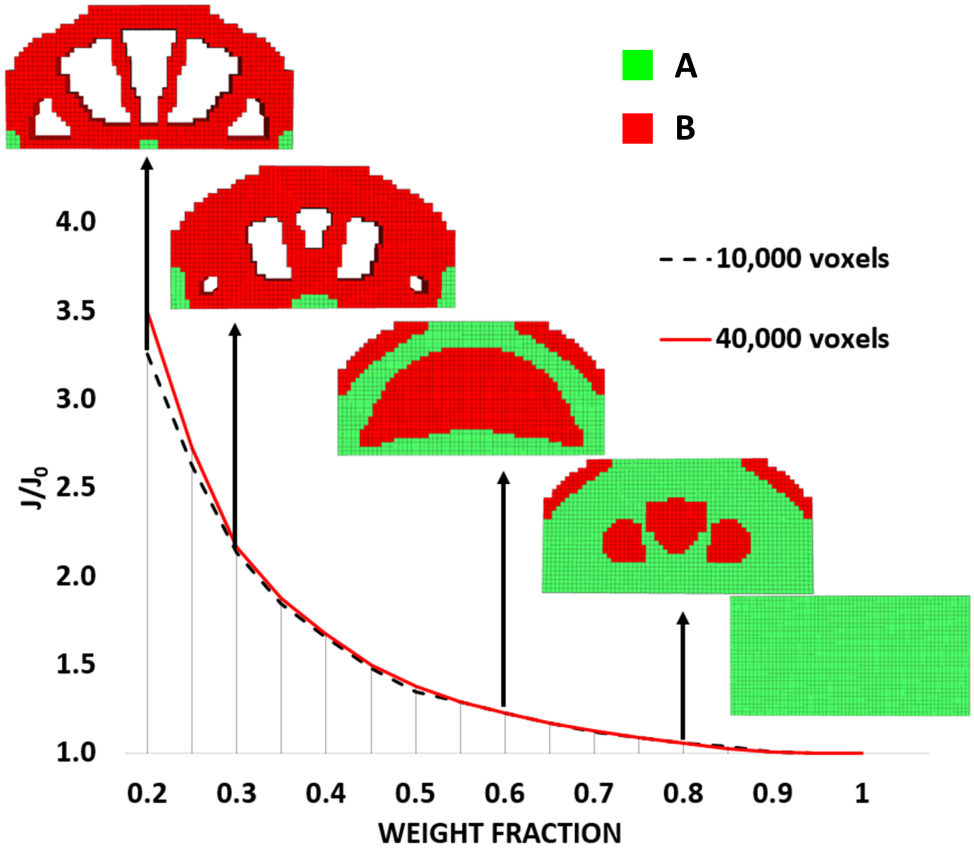

Figure 4.13: Pareto curves for 10,000 and 40,000 elements.

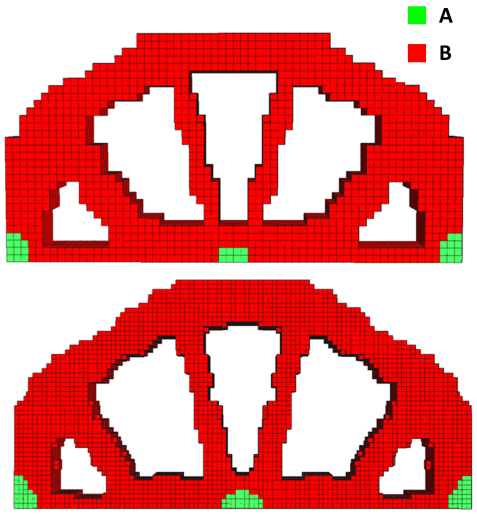

Figure 4.14: MBB structure with 10,000 and 40,000 elements at weight fraction of 0.2.

4.5.3 Cantilevered Beam: Three-Material Pareto Curve

In this experiment, we consider three materials. The geometry and boundary conditions are illustrated in Figure 4.15. The design is discretized using 30,000 elements, i.e. 101,400 degrees of freedom.

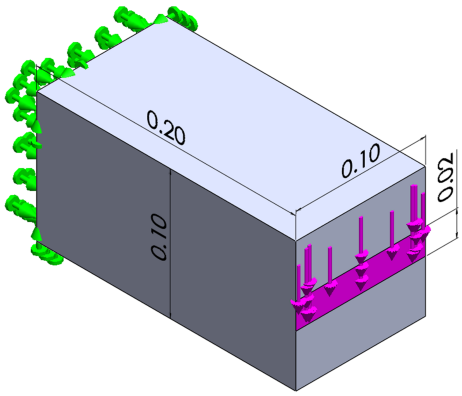

Figure 4.15: Cantilevered beam.

The material properties are summarized in Table 4.2. We solve the MMTO problem for 3 different scenarios: (1) pure A (single material), (2) A and B (two materials) and (3) A, B, and C (three materials).

Table 4.2: Material Properties of A, B and C.

Material	$E(GPa)$	ν	$\rho(Kg/m^3)$
A	380	0.2	19250
B	210	0.3	7800
B	110	0.25	4390

Beginning with all A initial design, the objective is to reduce mass by 70% while keeping the design as stiff as possible. Figure 4.16a shows the optimized design using only material A , Figure 4.16b is optimized design with materials A and B. Figure 4.16c illustrates optimized designs using A and C. Finally, Figure 4.16d illustrates the optimized

design at 0.3 mass fraction using all three materials.

Figure 4.17 illustrates the 4 Pareto curves, and the topologies for the third scenario. As one can observe, moving from one material to two-materials results in a significant improvement of 27% for both cases of A-B and A-C, and adding the third-material further improves the design by 29%. It is also interesting that up to 50% mass reduction, A-B results are identical to those of A-B-C and only in lower mass fractions does the third material improve the result.

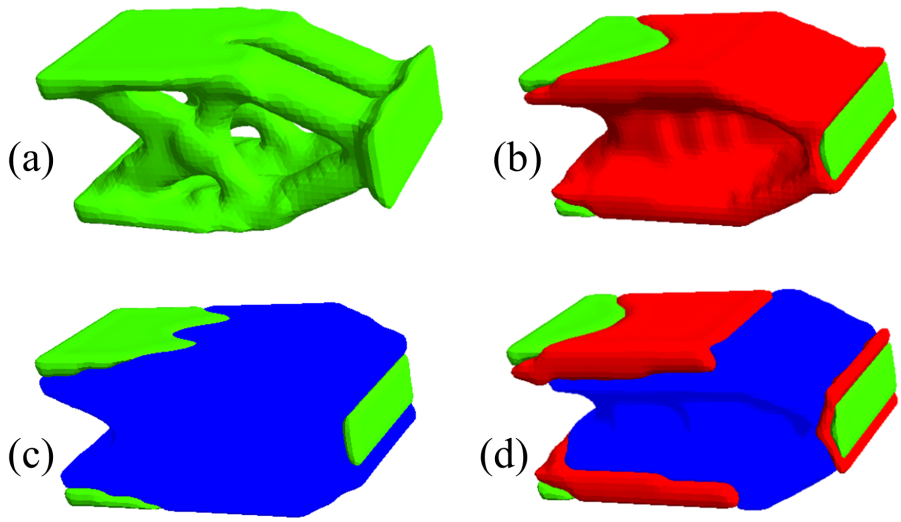

Figure 4.16: Optimized cantilever beam at 0.3 mass fraction, (a) only A ,(b) A and B, (c) A,C, and (d) A, B, and C.

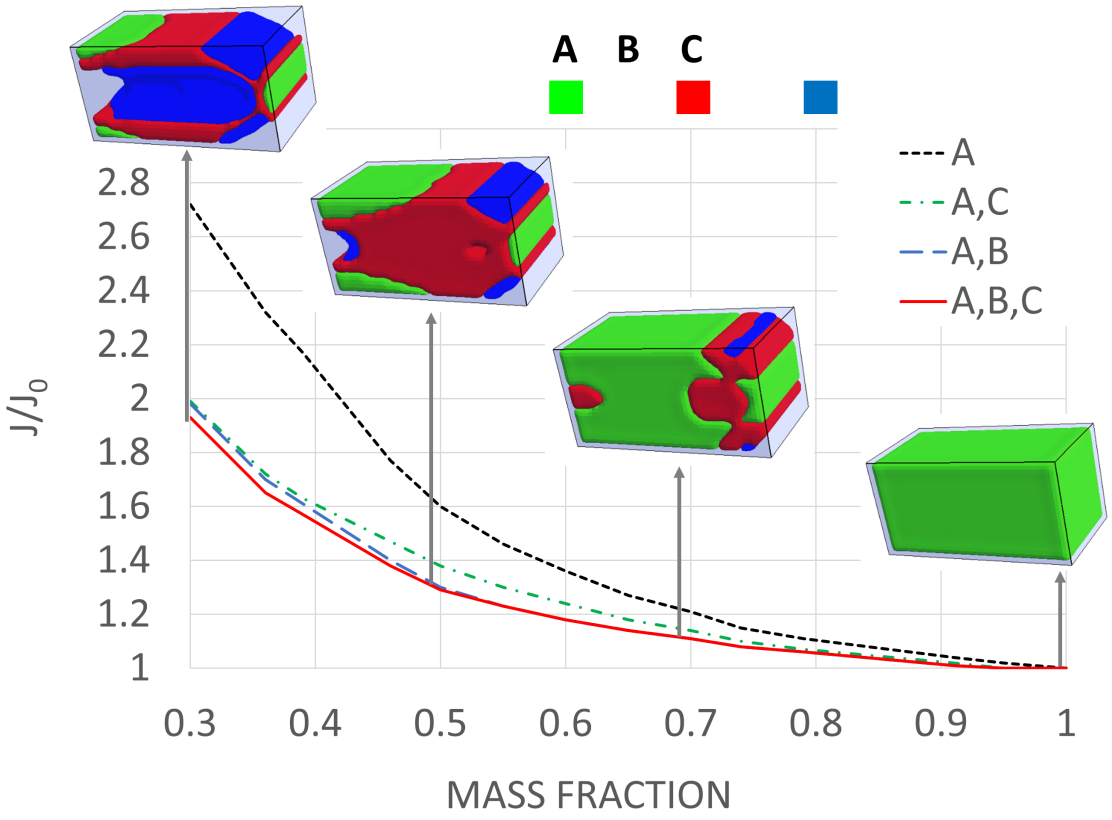

Figure 4.17: Effect of number of materials on Pareto Curve.

4.5.4 Mount-Bracket: a case study

This example focuses on demonstrating robustness and efficiency of the proposed method via a more complex and large scale design. Consider the mount bracket of Figure 4.18 and its corresponding boundary conditions. The domain is discretized into 40,000 hexahedral elements with 163,929 dof.

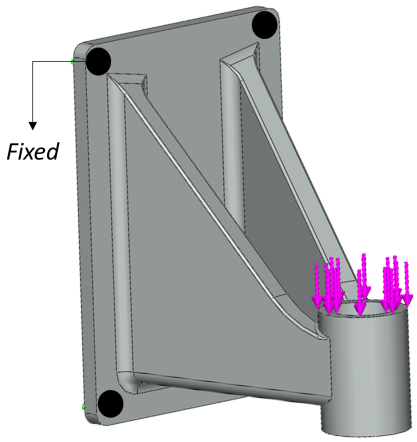

Figure 4.18: Mount bracket, geometry and boundary conditions.

There are many metallic filaments available for FDM. For this example, let us consider Copper-PLA and Aluminum-PLA filaments. Neglecting anisotropic behavior due to lack of data, the effective isotropic material properties for these materials can be found via applying the rule of mixture and are according to Table 4.3. Obviously, copper filament is both stiffer and heavier.

Table 4.3: Material Properties of Copper-PLA and Aluminum-PLA.

Material	$E(GPa)$	ν	$\rho(Kg/m^3)$
Copper-PLA (40%-60%)	45.2	0.33	4340
Aluminum-PLA (40%-60%)	28.8	0.33	1836

Given these material choices and beginning with the stiffest and heaviest initial design, the objective is to reduce mass by 60%. Figure 4.20 illustrates cross-sectional views of the design of Figure 4.19b. Using both materials reduces compliance of final design by about 13%.

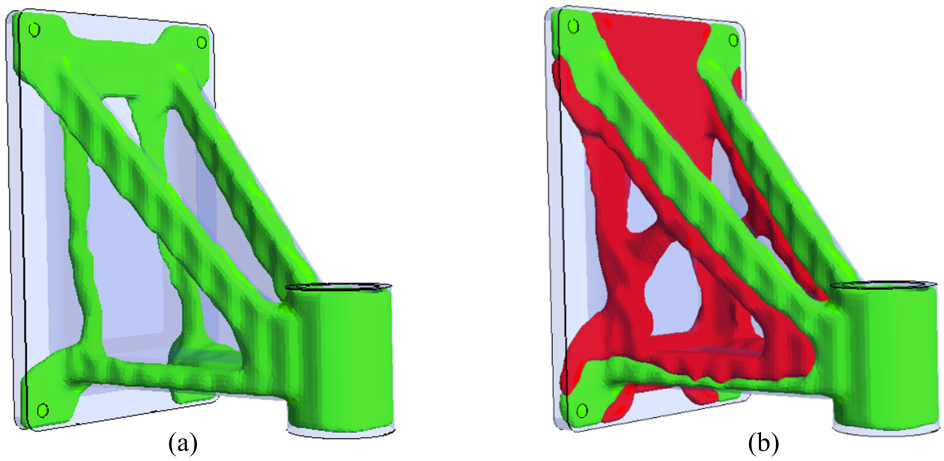

Figure 4.19: Mount bracket, optimized design at mass fraction of 0.4 using (a) only A and (b) A and B.

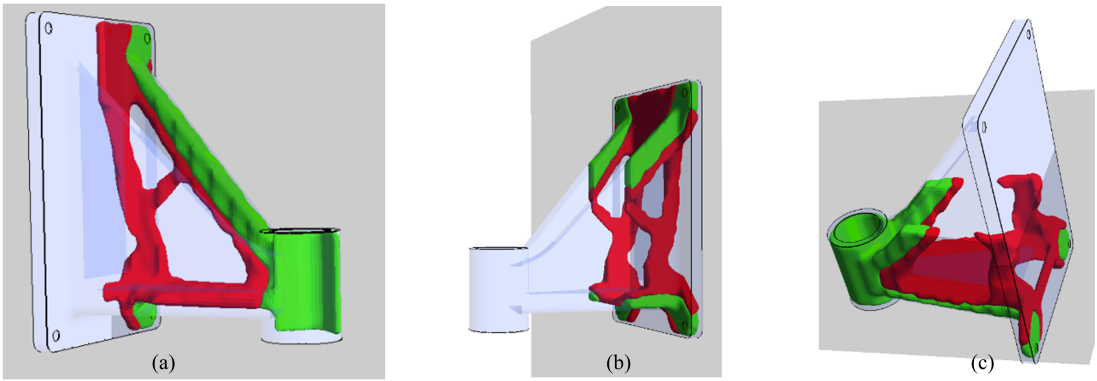

Figure 4.20: Mount bracket cross-sectional views.

Figure 4.21 illustrates the Pareto fronts for single-material TO with Copper-PLA and bi-material TO with both materials in Table 4.3.

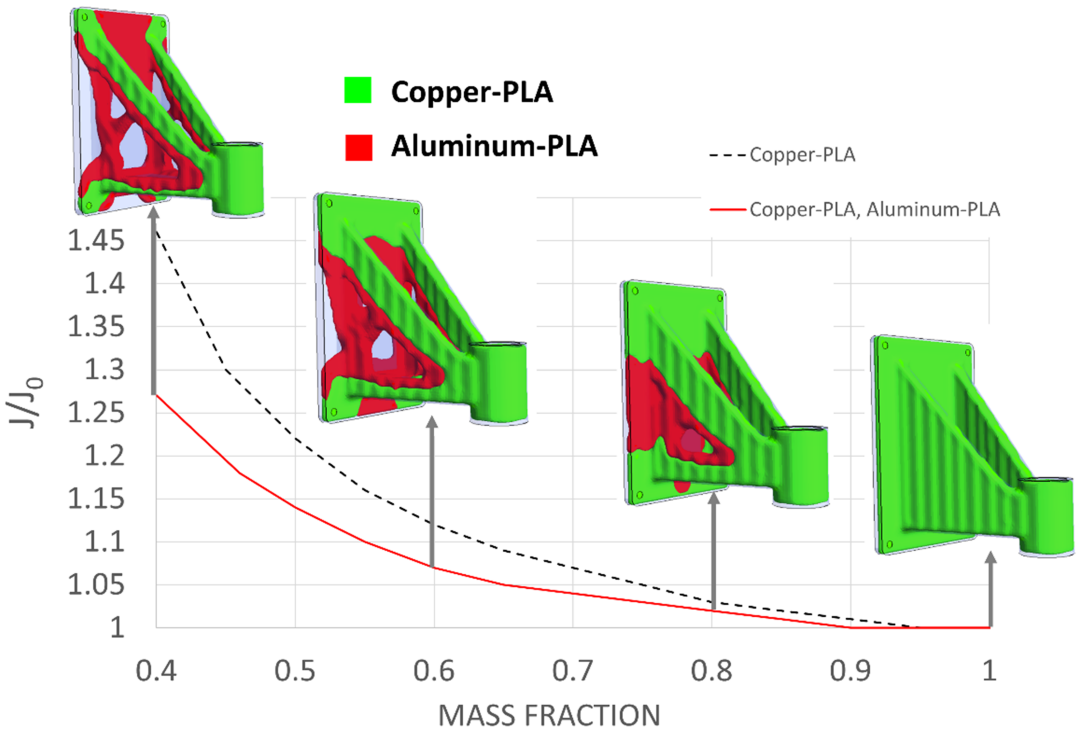

Figure 4.21: Mount bracket Pareto frontiers for copper-PLA and Aluminum-PLA filaments.

Further, as stated in section 4.4.6, tracing the Pareto curve need not begin at the heaviest design. For the two materials of Table 4.3 we can generate a random material distribution, which results in a sub-optimal design at 0.7 mass fraction. Thus, we first need to find optimal material distribution at 0.7 mass fraction through algorithm of Figure 4.8. Once this Pareto-optimal design is found, subsequent optimal designs can be generated via the algorithm of Figure 4.5. The process is demonstrated and compared against original Pareto tracing in Figure 4.22.

Observe that for this particular example, optimal design at mass fraction of 0.7 is similar for both methods. However, it is well-known that for complex geometries and loading conditions, there exist multiple (locally) optimal solutions with similar performance. It might be possible to rapidly explore the design space through efficiently combining algorithms of Figure 4.5 and Figure 4.8.

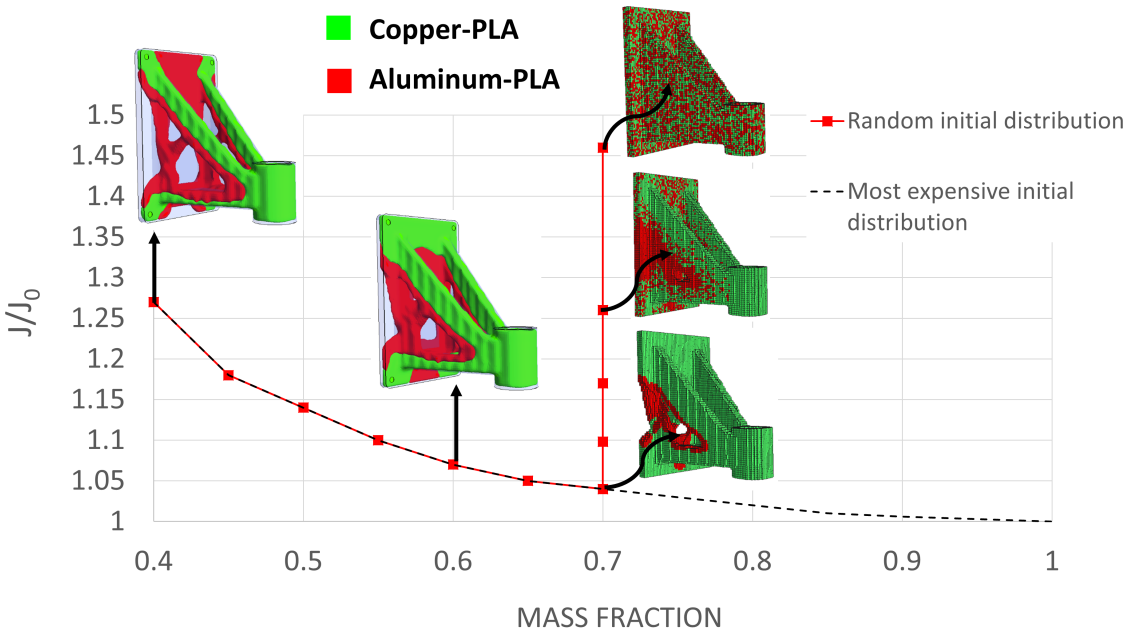

Figure 4.22: Mount bracket with random initial material distribution.

4.5.5 Run times and Memory Requirements

For all the experiments presented in this section, Table 4.4 summarizes the degrees of freedom, the target weight (or cost), total run-time, and required memory. All experiments were conducted on an Intel Core i7 CPU running at 3.4 GHz with 8GB of memory. Observe that all of the optimizations are completed in about a minute, and use the limited memory (in the order of a tens of Mega-Bytes).

Table 4.4: Summary of computational costs.

Example	#DOF	Target weight	Time	Memory (MB)
L-bracket	41,700	30%	2 min.	40
MBB	36,300	20%	2 min	30
Beam	34,000	20%	2 min	30
Mount Bracket	163,929	40%	3 min	60

CHAPTER V

Summary and Future Work

In this thesis, topology optimization based on Pareto-optimality is extended to consider support structure and material anisotropy in design for additive manufacturing. Furthermore, to take advantage of capabilities of AM in free-form fabrication, a multi-material topology optimization methodology is proposed to generate more complex optimal designs with improved performance.

In chapter 2, a topology optimization framework is proposed that leads to designs with reduced support structures. Specifically, we introduced a novel topological sensitivity approach for constraining support structure volume during design optimization. The effectiveness of the proposed scheme was illustrated through several numerical examples, and demonstrated using FDM technology. Support structures were assumed to be vertical for simplicity, but we believe that the methodology can be extended to handle non-vertical support structures. Additionally, the weighting proposed in this paper is simple and effective, but, in the future, we expect to adopt the method of Lagrange Multipliers. Finally, the proposed method must be coupled with methods for finding the optimum build direction to further reduce support volume.

In chapter 3, we have proposed a method to compute strength sensitivity based on generalized failure criteria such as Tsai-Wu for anisotropic parts. For numerical experiments, we have focused on anisotropic strengths of additively manufactured parts

where tensile strength along build direction is lower than other directions. The proposed framework can be extended to also include constitutive anisotropy, which requires accurate tensile and shear measurements. Also, the fact that the materials is brittle must be taken into consideration through a more comprehensive fracture model and sensitivity analysis. Moreover, the current printing processes introduce uncertainty in the material behavior, considering robustness can also be beneficial. Furthermore, the sensitivity can be extended to strength-based multi-material topology optimization. For multiple materials, since each material has its own strength, vonMises criterion is inadequate and more generalized failure indices are suitable. However, local de-bonding effects must also be considered. In chapter 4, a multi-material topology optimization scheme is presented. The method traces Pareto curve involving two conflicting objectives such as stiffness and weight (or stiffness and price). The element sensitivity is used to drive the optimization process. While the element sensitivity field can be treated as a multi-colored level set, for computational efficiency, we propose and justify a simple heuristic for discrete element-swapping. The effectiveness and robustness of this method is demonstrated via a number of 3D examples.

Future work can focus on other performance metrics, considering multiple load cases and multiple constraints. Further, before this method can be deployed in AM, potential de-bonding, stress residuals, feature size, and other AM-related issues must be accounted for.

Finally, the work presented in this thesis have mainly focused on elasticity effects, while there are many issues due to thermal effects that also need to be considered. Future research is required to integrate AM and TO through thermo-elastic formulations.

BIBLIOGRAPHY

BIBLIOGRAPHY

[1] Case Studies,Voxel8,http://www.voxel8.com/case-studies.

[2] Overview over 3d printing technologies, Additively, https://www.additively.com/en/learn-about/3d-printing-technologies.

[3] Tips for Designing a 3d Printed Part | Innovation Station, https://innovationstation.utexas.edu/tip-design.

[4] Cooper, K., Steele, P., Cheng, B., and Chou, K. "Contact Free Support Structures for Part Overhangs in Powder-Bed Metal Additive Manufacturing".

[5] Rankouhi, B., Javadpour, S., Delfanian, F., and Letcher, T., 2016. "Failure Analysis and Mechanical Characterization of 3d Printed ABS With Respect to Layer Thickness and Orientation". *J Fail. Anal. and Preven.,* **16**(3), June, pp. 467–481.

[6] Gao, T., and Zhang, W., 2011. "A mass constraint formulation for structural topology optimization with multiphase materials". *International Journal for Numerical Methods in Engineering,* **88**(8), Nov., pp. 774–796.

[7] Eschenauer, H. A., and Olhoff, N., 2001. "Topology optimization of continuum structures: A review". *Applied Mechanics Reviews,* **54**(4), p. 331.

[8] Bendsoe, M. P., and Sigmund, O., 2004. *Topology Optimization.* Springer Berlin Heidelberg, Berlin, Heidelberg.

[9] Rozvany, G. I. N., 2009. "A critical review of established methods of structural topology optimization". *Struct Multidisc Optim,* **37**(3), Jan., pp. 217–237.

[10] Kesseler, E., and Vankan, W. J., 2006. "Multidisciplinary design analysis and multiobjective optimisation applied to aircraft wing".

[11] Alonso, J. J., LeGresley, P., and Pereyra, V., 2009. "Aircraft design optimization". *Mathematics and Computers in Simulation,* **79**(6), Feb., pp. 1948–1958.

[12] Coverstone-Carroll, V., Hartmann, J. W., and Mason, W. J., 2000. "Optimal multiobjective low-thrust spacecraft trajectories". *Computer Methods in Applied Mechanics and Engineering,* **186**(2-4), June, pp. 387–402.

[13] Wang, L., Basu, P. K., and Leiva, J. P., 2004. "Automobile body reinforcement by finite element optimization". *Finite Elements in Analysis and Design,* **40**(8), May, pp. 879–893.

[14] Harzheim, L., and Graf, G., 2005. "A review of optimization of cast parts using topology optimization". *Struct Multidisc Optim,* **31**(5), Dec., pp. 388–399.

[15] Krishnakumar, A., and Suresh, K., 2015. "Hinge-Free Compliant Mechanism Design Via the Topological Level-Set". *J. Mech. Des,* **137**(3), Mar., p. 10.

[16] Gibson, I., Rosen, D., and Stucker, B., 2015. *Additive Manufacturing Technologies*. Springer New York, New York, NY.

[17] Brackett, D., Ashcroft, I., and Hague, R., 2011. "Topology optimization for additive manufacturing". In 22nd Annual international solid freeform fabrication symposium, pp. 348–362.

[18] Bendsoe, M. P., and Sigmund, O., 1999. "Material interpolation schemes in topology optimization". *Archive of applied mechanics,* **69**(9-10), pp. 635–654.

[19] Sigmund, O., 1997. "On the Design of Compliant Mechanisms Using Topology Optimization". *Mechanics of Structures and Machines,* **25**(4), Jan., pp. 493–524.

[20] Sigmund, O., 2001. "Design of multiphysics actuators using topology optimization-Part II: Two-material structures". *Computer Methods in Applied Mechanics and Engineering,* **190**(49-50), Oct., pp. 6605–6627.

[21] Allaire, G., Jouve, F., and Toader, A.-M., 2002. "A level-set method for shape optimization". *Comptes Rendus Mathematique,* **334**(12), pp. 1125–1130.

[22] Allaire, G., De Gournay, F., Jouve, F., and Toader, A., 2005. "Structural optimization using topological and shape sensitivity via a level set method". *Control and cybernetics,* **34**(1), p. 59.

[23] Chu, D. N., Xie, Y. M., Hira, A., and Steven, G. P., 1996. "Evolutionary structural optimization for problems with stiffness constraints". *Finite Elements in Analysis and Design,* **21**(4), Apr., pp. 239–251.

[24] Huang, X., and Xie, Y. M., 2008. "Bi-directional evolutionary topology optimization of continuum structures with one or multiple materials". *Comput Mech,* **43**(3), July, pp. 393–401.

[25] Liu, X., Yi, W.-J., Li, Q. S., and Shen, P.-S., 2008. "Genetic evolutionary structural optimization". *Journal of Constructional Steel Research,* **64**(3), Mar., pp. 305–311.

[26] Deaton, J. D., and Grandhi, R. V., 2013. "A survey of structural and multidisciplinary continuum topology optimization: post 2000". *Struct Multidisc Optim,* **49**(1), July, pp. 1–38.

[27] Xie, Y. M., and Steven, G. P., 1993. "A simple evolutionary procedure for structural optimization". *Computers & Structures,* **49**(5), Dec., pp. 885–896.

[28] Xie, Y. M., and Steven, G. P., 1996. "Evolutionary structural optimization for dynamic problems". *Computers & Structures,* **58**(6), Mar., pp. 1067–1073.

[29] Querin, O. M., Steven, G. P., and Xie, Y. M., 2000. "Evolutionary structural optimisation using an additive algorithm". *Finite Elements in Analysis and Design,* **34**(3-4), Feb., pp. 291–308.

[30] Feijoo, R. A., Novotny, A. A., Taroco, E., and Padra, C., 2005. "The topological-shape sensitivity method in two-dimensional linear elasticity topology design". *Applications of Computational Mechanics in Structures and Fluids*.

[31] Novotny, A. A., Feijoo, R. A., Taroco, E., and Padra, C., 2007. "Topological sensitivity analysis for three-dimensional linear elasticity problem". *Computer Methods in Applied Mechanics and Engineering,* **196**(41), pp. 4354–4364.

[32] Suresh, K., and Takalloozadeh, M., 2013. "Stress-constrained topology optimization: a topological level-set approach". *Struct Multidisc Optim,* **48**(2), Mar., pp. 295–309.

[33] Suresh, K., 2012. "Efficient generation of large-scale pareto-optimal topologies". *Struct Multidisc Optim,* **47**(1), May, pp. 49–61.

[34] Babu, S. S., Love, L., Dehoff, R., Peter, W., Watkins, T. R., and Pannala, S., 2015. "Additive manufacturing of materials: Opportunities and challenges". *MRS Bulletin,* **40**(12), Dec., pp. 1154–1161.

[35] Khoshnevis, B., Hwang, D., Yao, K.-T., and Yeh, Z., 2006. "Mega-scale fabrication by Contour Crafting". *International Journal of Industrial and Systems Engineering,* **1**(3), Jan., pp. 301–320.

[36] Bandyopadhyay, A., Bose, S., and Das, S., 2015. "3d printing of biomaterials". *MRS Bulletin,* **40**(2), Feb., pp. 108–115.

[37] Hoyt, R. P. "SpiderFab: An Architecture for Self-Fabricating Space Systems". In *AIAA SPACE 2013 Conference and Exposition*. American Institute of Aeronautics and Astronautics.

[38] Jibin, Z., 2005. "Determination of optimal build orientation based on satisfactory degree theory for RPT". In Ninth International Conference on Computer Aided Design and Computer Graphics, 2005, p. 6.

[39] Pandey, P. M., Thrimurthulu, K., and *, N. V. R., 2004. "Optimal part deposition orientation in FDM by using a multicriteria genetic algorithm". *International Journal of Production Research,* **42**(19), Oct., pp. 4069–4089.

[40] Nezhad, A. S., Barazandeh, F., Rahimi, A. R., and Vatani, M., 2010. "Pareto-Based Optimization of Part Orientation in Stereolithography". *Proceedings of the Institution of Mechanical Engineers, Part B: Journal of Engineering Manufacture,* **224**(10), Oct., pp. 1591–1598.

[41] Paul, R., and Anand, S., 2014. "Optimization of layered manufacturing process for reducing form errors with minimal support structures". *Journal of Manufacturing Systems*.

[42] Das, P., Chandran, R., Samant, R., and Anand, S., 2015. "Optimum Part Build Orientation in Additive Manufacturing for Minimizing Part Errors and Support Structures".

[43] Zhang, X., Le, X., Panotopoulou, A., Whiting, E., and Wang, C. C. L., 2015. "Perceptual Models of Preference in 3d Printing Direction". *ACM Trans. Graph.,* **34**(6), Oct., pp. 215:1–215:12.

[44] Umetani, N., and Schmidt, R., 2013. "Cross-sectional structural analysis for 3d printing optimization". *SIGGRAPH Asia,* **5**, pp. 1–4.

[45] Vanek, J., Galicia, J. A. G., and Benes, B., 2014. "Clever Support: Efficient Support Structure Generation for Digital Fabrication". *Computer Graphics Forum,* **33**(5), Aug., pp. 117–125.

[46] Barnett, E., and Gosselin, C., 2015. "Weak Support Material Techniques For Alternative Additive Manufacturing Materials". *Additive Manufacturing*.

[47] Dumas, J., Hergel, J., and Lefebvre, S., 2014. "Bridging the Gap: Automated Steady Scaffoldings for 3d Printing". *ACM Trans. Graph.,* **33**(4), July, pp. 98:1–98:10.

[48] Chen, Y., Li, K., and Qian, X., 2013. "Direct geometry processing for telefabrication". *Journal of Computing and Information Science in Engineering,* **13**(4), p. 041002.

[49] Gebhardt, A., 2011. "Additive Manufacturing Design and Strategies". In *Understanding Additive Manufacturing*, A. Gebhardt, ed. Hanser, pp. 103–128.

[50] Gibson, I., Goenka, G., Narasimhan, R., and Bhat, N., 2010. "Design rules for additive manufacture". In International Solid Free Form Fabrication Symposium.

[51] Liu, L., Wang, C., Shamir, A., and Whiting, E., 2014. "3d printing oriented design: geometry and optimization". In SIGGRAPH Asia 2014 Courses, ACM, p. 1.

[52] Seepersad, C. C., Govett, T., Kim, K., Lundin, M., and Pinero, D., 2012. "A designer's guide for dimensioning and tolerancing SLS parts". In Solid Freeform Fabrication Symposium, Austin, TX, pp. 921–931.

[53] Williams, C. B., and Seepersad, C. C., 2012. "Design for additive manufacturing curriculum: A problem-and project-based approach". In International solid freeform fabrication symposium, pp. 81–92.

[54] Zhou, M., Fleury, R., Shyy, Y.-K., Thomas, H., and Brennan, J. "Progress in Topology Optimization with Manufacturing Constraints". In *9th AIAA/ISSMO Symposium on Multidisciplinary Analysis and Optimization*. American Institute of Aeronautics and Astronautics.

[55] Xia, Q., Shi, T., Wang, M. Y., and Liu, S., 2011. "Simultaneous optimization of cast part and parting direction using level set method". *Struct Multidisc Optim,* **44**(6), Aug., pp. 751–759.

[56] Wang, W., Wang, T. Y., Yang, Z., Liu, L., Tong, X., Tong, W., Deng, J., Chen, F., and Liu, X., 2013. "Cost-effective printing of 3d objects with skin-frame structures". *ACM Transactions on Graphics,* **32**(6), Nov., pp. 1–10.

[57] Leary, M., Merli, L., Torti, F., Mazur, M., and Brandt, M., 2014. "Optimal topology for additive manufacture: A method for enabling additive manufacture of support-free optimal structures". *Materials & Design,* **63**, Nov., pp. 678–690.

[58] Gaynor, A. T., Meisel, N. A., Williams, C. B., and Guest, J. K. "Topology Optimization for Additive Manufacturing: Considering Maximum Overhang Constraint". In *15th AIAA/ISSMO Multidisciplinary Analysis and Optimization Conference*. American Institute of Aeronautics and Astronautics.

[59] Hu, K., Jin, S., and Wang, C. C. L., 2015. "Support slimming for single material based additive manufacturing". *Computer-Aided Design,* **65**, Aug., pp. 1–10.

[60] Ce'a, J., Garreau, S., Guillaume, P., and Masmoudi, M., 2000. "The shape and topological optimizations connection". *Computer Methods in Applied Mechanics and Engineering,* **188**(4), Aug., pp. 713–726.

[61] Suresh, K., 2010. "A 199-line Matlab code for Pareto-optimal tracing in topology optimization". *Struct Multidisc Optim,* **42**(5), Nov., pp. 665–679.

[62] Suresh, K., 2015. "Topology Optimization on the Cloud: A Confluence of Technologies". In ASME 2015 International Design Engineering Technical Conferences and Computers and Information in Engineering Conference, American Society of Mechanical Engineers, pp. V01AT02A041–V01AT02A041.

[63] Jiang, Y., Kautz, H., and Selman, B., 1995. *Solving Problems with Hard and Soft Constraints Using a Stochastic Algorithm for MAX-SAT*.

[64] Nocedal, J., and Wright, S., 2006. *Numerical Optimization*. Springer Science & Business Media, Dec.

[65] Deng, S., and Suresh, K., 2014. "Multi-constrained topology optimization via the topological sensitivity". *Struct Multidisc Optim,* **51**(5), Nov., pp. 987–1001.

[66] Lorensen, W. E., and Cline, H. E., 1987. "Marching Cubes: A High Resolution 3d Surface Construction Algorithm". In Proceedings of the 14th Annual Conference on Computer Graphics and Interactive Techniques, SIGGRAPH '87, ACM, pp. 163–169.

[67] Riddick, J. C., Haile, M. A., Wahlde, R. V., Cole, D. P., Bamiduro, O., and Johnson, T. E., 2016. "Fractographic analysis of tensile failure of acrylonitrile-butadiene-styrene fabricated by fused deposition modeling". *Additive Manufacturing,* **11**, July, pp. 49–59.

[68] Dowling, N. E., 1993. *Mechanical behavior of materials : engineering methods for deformation, fracture, and fatigue*. Prentice Hall.

[69] Sokolowski, J., and Zolesio, J.-P., 1992. "Introduction to shape optimization". In *Introduction to Shape Optimization*, no. 16 in Springer Series in Computational Mathematics. Springer Berlin Heidelberg, pp. 5–12.

[70] Changwen, X., and Minghua, Y., 1990. "Shape optimization of structures to minimize stress concentration". *Computers & Structures,* **36**(3), pp. 491–497.

[71] Sved, G., and Ginos, Z., 1968. "Structural optimization under multiple loading". *International Journal of Mechanical Sciences,* **10**(10), Oct., pp. 803–805.

[72] Kirsch, U., 1987. "Optimal Topologies of Flexural Systems". *Engineering Optimization,* **11**(1-2), Apr., pp. 141–149.

[73] Kirsch, U., 1990. "On singular topologies in optimum structural design". *Structural Optimization,* **2**(3), Sept., pp. 133–142.

[74] Cheng, G., and Jiang, Z., 1992. "Study on Topology Optimization with Stress Constraints". *Engineering Optimization,* **20**(2), Nov., pp. 129–148.

[75] Cheng, G. D., and Guo, X., 1997. "ε relaxed approach in structural topology optimization". *Structural Optimization,* **13**(4), June, pp. 258–266.

[76] Duysinx, P., and M. P. Bendsoe, 1998. "Topology optimization of continuum structures with local stress constraints". *Int. J. Numer. Meth. Engng.,* **43**(8), Dec., pp. 1453–1478.

[77] Rozvany, G. I. N., 2014. "On design-dependent constraints and singular topologies". *Struct Multidisc Optim,* **21**(2), Feb., pp. 164–172.

[78] Bendsoe, M. P., and Kikuchi, N., 1988. "Generating Optimal Topologies In Syuctural Design using A Homogenization Method". *Computer Methods in Applied Mechanics and Engineering,* **71**, Mar., pp. 197–224.

[79] Bendsoe, M. P., 1989. "Optimal shape design as a material distribution problem". *Structural Optimization,* **1**(4), Dec., pp. 193–202.

[80] Zhou, M., and Rozvany, G. I. N., 2001. "On the validity of ESO type methods in topology optimization". *Struct Multidisc Optim,* **21**(1), Mar., pp. 80–83.

[81] Yang, R. J., and Chen, C. J., 1996. "Stress-based topology optimization". *Structural Optimization,* **12**(2-3), Oct., pp. 98–105.

[82] Bruggi, M., and Venini, P., 2008. "A mixed FEM approach to stress-constrained topology optimization". *Int. J. Numer. Meth. Engng.,* **73**(12), Mar., pp. 1693–1714.

[83] Bruggi, M., 2008. "On an alternative approach to stress constraints relaxation in topology optimization". *Struct Multidisc Optim,* **36**(2), Jan., pp. 125–141.

[84] Le, C., Norato, J., Bruns, T., Ha, C., and Tortorelli, D., 2009. "Stress-based topology optimization for continua". *Struct Multidisc Optim,* **41**(4), Oct., pp. 605–620.

[85] Paris, J., Navarrina, F., Colominas, I., and Casteleiro, M., 2010. "Stress constraints sensitivity analysis in structural topology optimization". *Computer Methods in Applied Mechanics and Engineering,* **199**(33-36), July, pp. 2110–2122.

[86] Paris, J., Navarrina, F., Colominas, I., and Casteleiro, M., 2008. "Topology optimization of continuum structures with local and global stress constraints". *Struct Multidisc Optim,* **39**(4), Nov., pp. 419–437.

[87] Holmberg, E., Torstenfelt, B., and Klarbring, A., 2013. "Stress constrained topology optimization". *Struct Multidisc Optim,* **48**(1), Feb., pp. 33–47.

[88] Miegroet, L. V., and Duysinx, P., 2007. "Stress concentration minimization of 2d filets using X-FEM and level set description". *Struct Multidisc Optim,* **33**(4-5), Jan., pp. 425–438.

[89] Svanberg, K., and Werme, M., 2007. "Sequential integer programming methods for stress constrained topology optimization". *Struct Multidisc Optim,* **34**(4), May, pp. 277–299.

[90] Allaire, G., and Jouve, F., 2008. "Minimum stress optimal design with the level set method". *Engineering Analysis with Boundary Elements,* **32**(11), Nov., pp. 909–918.

[91] Amstutz, S., and Novotny, A. A., 2009. "Topological optimization of structures subject to Von Mises stress constraints". *Struct Multidisc Optim,* **41**(3), Aug., pp. 407–420.

[92] Xia, Q., Shi, T., Liu, S., and Wang, M. Y., 2012. "A level set solution to the stress-based structural shape and topology optimization". *Computers & Structures,* **90-91**, Jan., pp. 55–64.

[93] Poon, N. M. K., and Martins, J. R. R. A., 2006. "An adaptive approach to constraint aggregation using adjoint sensitivity analysis". *Struct Multidisc Optim,* **34**(1), Dec., pp. 61–73.

[94] Cai, S., Zhang, W., Zhu, J., and Gao, T., 2014. "Stress constrained shape and topology optimization with fixed mesh: A B-spline finite cell method combined with level set function". *Computer Methods in Applied Mechanics and Engineering,* **278**, Aug., pp. 361–387.

[95] Emmendoerfer, H., and Fancello, E. A., 2014. "A level set approach for topology optimization with local stress constraints". *Int. J. Numer. Meth. Engng,* **99**(2), July, pp. 129–156.

[96] Cai, S., and Zhang, W., 2015. "Stress constrained topology optimization with free-form design domains". *Computer Methods in Applied Mechanics and Engineering,* **289**, June, pp. 267–290.

[97] Schneider, M., and Andrä, H., 2014. "The topological gradient in anisotropic elasticity with an eye towards lightweight design". *Mathematical Methods in the Applied Sciences,* **37**(11), July, pp. 1624–1641.

[98] Delgado, G., and Bonnet, M., 2015. "The topological derivative of stress-based cost functionals in anisotropic elasticity". *Computers & Mathematics with Applications,* **69**(10), May, pp. 1144–1166.

[99] Hill, R., 1998. *The Mathematical Theory of Plasticity*. Clarendon Press.

[100] Azzi, V. D., and Tsai, S. W., 1965. "Anisotropic strength of composites". *Experimental Mechanics,* **5**(9), Sept., pp. 283–288.

[101] Hoffman, O., 1967. "The Brittle Strength of Orthotropic Materials". *Journal of Composite Materials,* **1**(2), Apr., pp. 200–206.

[102] Tsai, S. W., and Wu, E. M., 1971. "A General Theory of Strength for Anisotropic Materials". *Journal of Composite Materials,* **5**(1), Jan., pp. 58–80.

[103] Berthelot, J.-M., 1999. *Composite Materials: Mechanical Behavior and Structural Analysis*. Springer Science & Business Media.

[104] Groenwold, A. A., and Haftka, R. T., 2006. "Optimization with non-homogeneous failure criteria like Tsai-Wu for composite laminates". *Struct Multidisc Optim,* **32**(3), July, pp. 183–190.

[105] Qiu, G. Y., and Li, X. S., 2009. "A note on the derivation of global stress constraints". *Struct Multidisc Optim,* **40**(1-6), May, p. 625.

[106] Guo, X., Zhang, W. S., Wang, M. Y., and Wei, P., 2011. "Stress-related topology optimization via level set approach". *Computer Methods in Applied Mechanics and Engineering,* **200**(47-48), Nov., pp. 3439–3452.

[107] Sung Hoon Ahn, Michael Montero, Dan Odell, Shad Roundy, and Paul K. Wright, 2002. "Anisotropic material properties of fused deposition modeling ABS". *Rapid Prototyping Journal,* **8**(4), Oct., pp. 248–257.

[108] Sung Hoon Ahn, Changil Baek, Sunyoung Lee, and In Shup Ahn, 2003. "Anisotropic Tensile Failure Model of Rapid Prototyping Parts - Fused Deposition Modeling (FDM)". *Int. J. Mod. Phys. B,* **17**(08n09), Apr., pp. 1510–1516.

[109] Thomsen, J., 1992. "Topology optimization of structures composed of one or two materials". *Structural Optimization,* **5**(1-2), Mar., pp. 108–115.

[110] Yin, L., and Ananthasuresh, G. K., 2001. "Topology optimization of compliant mechanisms with multiple materials using a peak function material interpolation scheme". *Struct Multidisc Optim,* **23**(1), Dec., pp. 49–62.

[111] Jeong, S. H., Choi, D.-H., and Yoon, G. H., 2014. "Separable stress interpolation scheme for stress-based topology optimization with multiple homogenous materials". *Finite Elements in Analysis and Design,* **82**, May, pp. 16–31.

[112] Chaves, L. P., and Cunha, J., 2014. "Design of carbon fiber reinforcement of concrete slabs using topology optimization". *Construction and Building Materials,* **73**, Dec., pp. 688–698.

[113] de Kruijf, N., Zhou, S., Li, Q., and Mai, Y.-W., 2007. "Topological design of structures and composite materials with multiobjectives". *International Journal of Solids and Structures,* **44**(22-23), Nov., pp. 7092–7109.

[114] Sigmund, O., and Maute, K., 2013. "Topology optimization approaches". *Struct Multidisc Optim,* **48**(6), Dec., pp. 1031–1055.

[115] Blasques, J. P., and Stolpe, M., 2012. "Multi-material topology optimization of laminated composite beam cross sections". *Composite Structures,* **94**(11), Nov., pp. 3278–3289.

[116] Park, J., and Sutradhar, A., 2014. "A multi-resolution method for 3d multi-material topology optimization". *Computer Methods in Applied Mechanics and Engineering*, Nov.

[117] Wang, M. Y., and Wang, X., 2004. "âĂIJColorâĂİ level sets: a multi-phase method for structural topology optimization with multiple materials". *Computer Methods in Applied Mechanics and Engineering,* **193**(6-8), Feb., pp. 469–496.

[118] Wang, M. Y., Chen, S., Wang, X., and Mei, Y., 2005. "Design of Multimaterial Compliant Mechanisms Using Level-Set Methods". *J. Mech. Des.,* **127**(5), Jan., pp. 941–956.

[119] Wang, X., Mei, Y., and Wang, M. Y., 2004. "Level-set method for design of multiphase elastic and thermoelastic materials". *Int J Mech Mater Des,* **1**(3), Sept., pp. 213–239.

[120] Allaire, G., Dapogny, C., Delgado, G., and Michailidis, G., 2014. "Multi-Phase Structural optimization Via A Level-set Method". *Control Optimisation and Calculus of Variations*, pp. 576–611.

[121] Vermaak, N., Michailidis, G., Parry, G., Estevez, R., Allaire, G., and BrÃľchet, Y., 2014. "Material interface effects on the topology optimizationof multi-phase structures using a level set method". *Struct Multidisc Optim*, June, pp. 1–22.

[122] Wang, Y., Luo, Z., Kang, Z., and Zhang, N., 2015. "A multi-material level set-based topology and shape optimization method". *Computer Methods in Applied Mechanics and Engineering,* **283**, Jan., pp. 1570–1586.

[123] Sigmund, O., 2011. "On the usefulness of non-gradient approaches in topology optimization". *Struct Multidisc Optim,* **43**(5), Mar., pp. 589–596.

[124] Ramani, A., 2010. "A pseudo-sensitivity based discrete-variable approach to structural topology optimization with multiple materials". *Structural and Multidisciplinary Optimization,* **41**(6), June, pp. 913–934.

[125] Ramani, A., 2011. "Multi-material Topology Optimization with Strength Constraints". *Struct. Multidiscip. Optim.,* **43**(5), May, pp. 597–615.

[126] Yadav, P., and Suresh, K., 2014. "Large Scale Finite Element Analysis via Assembly-Free Deflated Conjugate Gradient". *Journal of Computing and Information Science in Engineering,* **14**(4), p. 041008.

APPENDICES

APPENDIX A

Element Sensitivity

The derivation of Equation 1.15 is included here for completeness. Consider the problem:

$$\mathbf{K}\mathbf{u}_0 = \mathbf{f} \tag{A.1}$$

Suppose an element is deleted from the mesh, this will lead to a change in $\mathbf{K}$, resulting in:

$$(\mathbf{K} - \Delta\mathbf{K}_e)(\mathbf{u}_0 + \Delta\mathbf{u}) = \mathbf{f} \tag{A.2}$$

Formally:

$$(\mathbf{u}_0 + \Delta\mathbf{u}) = (\mathbf{K} - \Delta\mathbf{K}_e)^{-1}\mathbf{f} \tag{A.3}$$

As a formal Neumann series:

$$(\mathbf{u}_0 + \Delta\mathbf{u}) = \left[\mathbf{u}_0 + \left(\mathbf{K}^{-1}\Delta\mathbf{K}_e\right)\mathbf{u}_0 + \left(\mathbf{K}^{-1}\Delta\mathbf{K}_e\right)^2\mathbf{u}_0 + \ldots\right] \tag{A.4}$$

Neglecting higher order terms

$$\Delta\mathbf{u} = \left(\mathbf{K}^{-1}\Delta\mathbf{K}_e\right)\mathbf{u}_0 \tag{A.5}$$

Now consider a quantity of interest:

$$\mathbf{Q}(\mathbf{u}) \tag{A.6}$$

The first order change in the quantity of interest is defined via its gradient with respect to the displacement:

$$\Delta Q \approx (\nabla_{\mathbf{u}} \mathbf{Q})^T \Delta \mathbf{u} \tag{A.7}$$

Substituting Equation A.5 into above, and taking the transpose:

$$\Delta Q \approx \left(\mathbf{K}^{-1} \nabla_{\mathbf{u}} \mathbf{Q}\right)^T (\Delta \mathbf{K}_e) \Delta \mathbf{u}_0 \tag{A.8}$$

Defining the adjoint as:

$$\boldsymbol{\lambda}_0 = -\mathbf{K}^{-1} \nabla_{\mathbf{u}} \mathbf{Q} \tag{A.9}$$

We have:

$$\Delta \mathbf{Q} \approx -\boldsymbol{\lambda}_0^T \Delta \mathbf{K}_e \mathbf{u}_0 \tag{A.10}$$

The above equation captures the first order change in any quantity of interest when an element is deleted. When an element is inserted, the sign changes:

$$\Delta \mathbf{Q} \approx \boldsymbol{\lambda}_0^T \Delta \mathbf{K}_e \mathbf{u}_0 \tag{A.11}$$

As a special case when the quantity of interest is the compliance, we have:

$$\mathbf{Q}(\mathbf{u}) = \mathbf{f}^T \mathbf{u} \tag{A.12}$$

Therefore:

$$\nabla_{\mathbf{u}} \mathbf{Q} = \mathbf{f} \tag{A.13}$$

And the adjoint is given by:

$$\boldsymbol{\lambda}_0 = -\mathbf{K}^{-1} \mathbf{f} = -\mathbf{u} \tag{A.14}$$

By substituting Equation A.14 in Equation A.10, we obtain Equation 1.15.

APPENDIX B

Support Structure Sensitivity

In this Appendix, we elaborate on the derivation of Equation 2.11. Consider the hole inserted in the interior of the design, we need to find support volume $A = a(A_1 + A_2)$ as illustrated in Figure B.1.

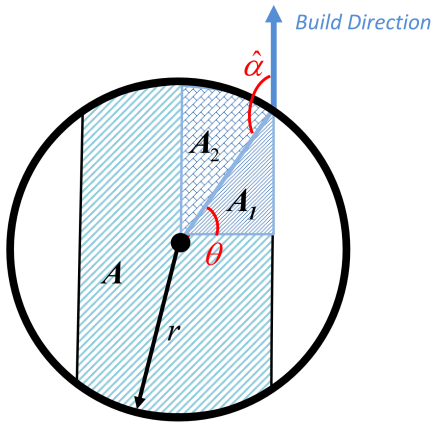

Figure B.1: Support area in a 2D interior hole.

Since $\theta = \hat{\alpha} - \frac{\pi}{2}$ we have:

$$A_1 = \frac{1}{2}(r\cos(\theta))(r\sin(\theta)) = \frac{1}{2}r^2\sin(\theta)\cos(\theta) = \frac{-1}{2}r^2\sin(\hat{\alpha})\cos(\hat{\alpha}) \tag{B.1}$$

$$A_2 = \left(\frac{\frac{\pi}{2}-\theta}{2\pi}\right)\pi r^2 = \frac{(\pi-\hat{\alpha})r^2}{2} \tag{B.2}$$

$$A = 2r^2(\pi - \hat{\alpha} - \sin(\hat{\alpha}\cos(\hat{\alpha}) \tag{B.3}$$

Next to find the support volume in a spherical ball with radius r we extend Equation B.3 as follows:

$$\begin{aligned} S &= \int_{-r\cos(\theta)}^{r\cos(\theta)} 2(r^2 - x^2)(\pi - \hat{\alpha} - \sin(\hat{\alpha})\cos(\hat{\alpha}))\,dx \\ &= 4r^3(\pi - \hat{\alpha} - \sin(\hat{\alpha})\cos(\hat{\alpha})\left(\sin(\hat{\alpha}) - \frac{\sin^3(\hat{\alpha})}{3}\right) \end{aligned} \tag{B.4}$$

Finally based on Equation 2.10 the topological sensitivity is computed via Equation B.5:

$$\mathscr{T}_S(p \in \Omega) = \lim_{\substack{\epsilon\to 0 \\ \delta\to 0}} \frac{4r^3(\pi - \hat{\alpha} - \sin(\hat{\alpha})\cos(\hat{\alpha}))(\sin(\hat{\alpha}) - \frac{\sin^3(\hat{\alpha})}{3})\left((\epsilon+\delta)^3 - \epsilon^3\right)}{\frac{4}{3}\pi\left((\epsilon+\delta)^3 - \epsilon^3\right)} \tag{B.5}$$

i.e.

$$\mathscr{T}_S(p \in \Omega) = \frac{3(\pi - \hat{\alpha} - \sin(\hat{\alpha})\cos(\hat{\alpha}))(\sin(\hat{\alpha}) - \frac{\sin^3(\hat{\alpha})}{3})}{\pi} \tag{B.6}$$

APPENDIX C

Anisotropic Strength Sensitivity

Consider the definition in Equation 3.19. Exploiting the p-norm definition in Equation 3.10, we have:

$$\mathbf{g} = \frac{1}{p}\left[\sum_e \gamma_e^{p-1}\frac{\partial \gamma_e}{\partial \mathbf{u}}\right] \tag{C.1}$$

must solve the following adjoint problem [31],

$$\mathbf{K}\boldsymbol{\mu} = \mathbf{g}^T \tag{C.2}$$

where $\boldsymbol{\mu}$ is the adjoint solution and $\mathbf{g}^T$ is the adjoint force. We are assuming hexahedral elements (with 8 nodes). Recalling Equations 3.3 and 3.8, the inverse of the strength ratio at each element $\gamma_e$depends on individual stress components at that element, which are evaluated as follows:

$$\{\sigma\}_{(6,1)} = [D]_{(6,6)}\,[B]_{(6,24)}\,\{u\}_{(24,1)} \tag{C.3}$$

Where $[D]$ is material tensor, $[B]$ is the gradient matrix, and

$$\begin{aligned} \{\sigma\}_{(6,1)} &= \{\sigma_{11} \quad \sigma_{22} \quad \sigma_{33} \quad \sigma_{23} \quad \sigma_{31} \quad \sigma_{12}\}^T \\ \{u\}_{(24,1)} &= \{u_1 \quad v_1 \quad w_1 \quad \ldots \quad u_8 \quad v_8 \quad w_8\}^T \end{aligned} \tag{C.4}$$

Hence, in order to evaluate Equation 3.19 we must evaluate Equation C.5:

$$\frac{\partial \gamma_e}{\partial \mathbf{u}} = \frac{2\dfrac{d\mathscr{A}}{d\mathbf{u}}}{-\mathscr{B}+\sqrt{\mathscr{B}^2+4\mathscr{A}}} - \frac{2\mathscr{A}\left[-\dfrac{d\mathscr{B}}{d\mathbf{u}}+\dfrac{2\mathscr{B}\dfrac{d\mathscr{B}}{d\mathbf{u}}+4\dfrac{d\mathscr{A}}{d\mathbf{u}}}{\sqrt{\mathscr{B}^2+4\mathscr{A}}}\right]}{(-\mathscr{B}+\sqrt{\mathscr{B}^2+4\mathscr{A}})^2} \tag{C.5}$$

where $\mathscr{A}$ and $\mathscr{B}$ are defined in Equation 3.3 and their derivatives are the generalization of the equations in [29],

$$\frac{d\mathscr{A}}{d\mathbf{u}} = 2\begin{bmatrix} C_{12}\left(F_{1,:}\sigma_{22}+F_{2,:}\sigma_{11}\right)+C_{13}\left(F_{1,:}\sigma_{33}+F_{3,:}\sigma_{11}\right)+C_{23}\left(F_{2,:}\sigma_{33}+F_{3,:}\sigma_{22}\right)+ \\ C_{11}\left(F_{1,:}\sigma_{11}\right)+C_{22}\left(F_{2,:}\sigma_{22}\right)+C_{33}\left(F_{3,:}\sigma_{33}\right)+ \\ C_{44}\left(F_{4,:}\sigma_{23}\right)+C_{55}\left(F_{5,:}\sigma_{31}\right)+C_{66}\left(F_{6,:}\sigma_{12}\right) \end{bmatrix} \tag{C.6}$$

$$\frac{d\mathscr{B}}{d\mathbf{u}} = C_1F_{1,:}+C_2F_{2,:}+C_3F_{3,:} \tag{C.7}$$

and

$$[F]_{6,24} = [D]_{(6,6)}[B]_{(6,24)} \tag{C.8}$$

It is worth noting that in Equation C.2, material anisotropy affects both stiffness matrix $\mathbf{K}$ through material tensor $\mathbf{D}$ and adjoint force $\mathbf{g}^T$ (through Tsai-Wu coefficients C_{ij} $i,j = 1,...,6$).